**ISTANBUL TECHNICAL UNIVERSITY ★ GRADUATE SCHOOL OF SCIENCE ENGINEERING AND TECHNOLOGY**

# ENGINEERING M-Si (M: Ag, Cu) THIN FILMS AS NEGATIVE ELECTRODES FOR LITHIUM ION BATTERIES

**Ph.D. THESIS**

**Billur Deniz KARAHAN**

**Department of Material Science and Engineering**

**Material Science and Engineering Programme**

**DECEMBER 2016**

**ISTANBUL TECHNICAL UNIVERSITY ★ GRADUATE SCHOOL OF SCIENCE ENGINEERING AND TECHNOLOGY**

# ENGINEERING M-Si (M: Ag, Cu) THIN FILMS AS NEGATIVE ELECTRODES FOR LITHIUM ION BATTERIES

**Ph.D. THESIS**

**Billur Deniz KARAHAN**
**(521102002)**

**Department of Material Science and Engineering**

**Material Science and Engineering Programme**

**Thesis Advisor: Assoc. Prof. Dr. Özgül KELEŞ**

**DECEMBER 2016**

**İSTANBUL TEKNİK ÜNİVERSİTESİ ★ FEN BİLİMLERİ ENSTİTÜSÜ**

# LITYUM IYON BATARYALARDA NEGATİF ELEKTROT OLARAK KULLANIMLARI İÇİN M-Si (M: Ag, Cu) İNCE FİLMLERİN TASARLANMASI

**DOKTORA TEZİ**

**Billur Deniz KARAHAN**
**(521102002)**

**Malzeme Bilimi ve Mühendisliği Anabilim Dalı**

**Malzeme Bilimi ve Mühendisliği Programı**

**Tez Danışmanı: Doç. Dr. Özgül KELEŞ**

**ARALIK 2016**

Billur Deniz Karahan, a Ph.D. student of İTU Graduate School of Science Engineering and Technology, student ID 521102002, successfully defended the dissertation entitled "ENGINEERING M-Si (M: Ag, Cu) THIN FILMS AS NEGATIVE ELECTRODES FOR LITHIUM ION BATTERIES", which she prepared after fulfilling the requirements specified in the associated legislations, before the jury whose signatures are below.

| | | |
|---|---|---|
| **Thesis Advisor :** | **Assoc. Prof. Dr. Özgül KELES**<br>Istanbul Technical University | **…………..…** |
| **Jury Members :** | **Prof. Dr. Gültekin GÖLLER**<br>Istanbul Technical University | **……………...** |
| | **Dr. Khalil AMINE**<br>Argonne National Lab. | **……………...** |
| | **Assoc. Prof. Dr. Özgül KELEŞ**<br>Istanbul Technical University | **………………** |
| | **Prof. Dr. Kürşat KAZMANLI**<br>Istanbul Technical University | **…….….…..** |
| | **Dr. Ali ABOUIMRANE**<br>Hamad Bin Khalifa University | **…....….……** |

**Date of Submission : 1 December 2016**
**Date of Defense : 21 December 2016**

***Canım oğlum Ali Faruk'a, beni her zaman destekleyen sevgili eşim Ömer'e ve yetiştirip bugünlere getiren değerli aileme,***

**FOREWORD**

I have a wealth of gratitude for my adviser Assoc. Prof. Dr. Özgül Keleş who has counseled me for eight years in the ways of my pursuit of research. Her decisive character, high motivation and human-based perspective have been an unique example to me. She means more than a supervisor to me. I am always thankful for her diligent mentoring of a person, not just a graduate student.

I am also grateful to Dr. Khalil Amine, Argonne National Laboratory for accepting me to work in his laboratories as a visitor scientist. His guidance and big support encourage me to accomplish this thesis. I also would like to thank Dr. O. Levent Eryilmaz for his great help to perform my experiments, Dr. Robert Erck for sharing his knowledge and experiences with me, and finally Dr. Ali Erdemir for his advice. Without them, this dissertation would be impossible to finish.

I would also like to thank my lab mates, especially Burçin Bilici, Ceren Yağsi, Emre Çetintaşoğlu, Kübra Yumakgil and Beril Akinci for their supports. We have made researching fun and productive.

I would also like to thank my professors who give me the opportunity to realize characterizations of my experiments: Prof. Dr. Gültekin Göller, Prof. Dr. Mustafa Urgen and Prof. Dr. Servet Timur.

Thanks to the funding agencies which supported this dissertation: The Scientific and Technological Reasearch Council of Turkey (TUBITAK) and ITU Scientific Research Project Coordination Office.

Lastly, I want to thank my husband and my family for the essential role they have played in accomplishing this work. To my parents who instill a strong work-ethic, outright person in me. I am beyond grateful for all their great support. To my Karahan family, I am indebted to each of you for encouraging and spurring on me.

A special thank to my husband, Omer, who was there whenever i felt good or bad with his special love and benignity.

December 2016 Billur Deniz KARAHAN
(MSc. Metallurgical and Material Science Engineer)

**TABLE OF CONTENTS**

**Page**

## ABBREVIATIONS

| | |
|---|---|
| **LIB** | : Lithium Ion Battery |
| **CD** | : Compact Disc |
| **DVD** | : Digital Versatile Disc |
| **NiMH** | : Nickel Metal hydride batteries |
| **NiCd** | : Nickel Cadmium batteries |
| **SEI** | : Solid Electrolyte Interphase |
| **GHG** | : Green-house gas |
| **EV** | : Electrical Vehicles |
| **BEV** | : Battery Electrical Vehicles |
| **PEV** | : Plug-in Electrical Vehicles |
| **$CO_2$** | : Carbon dioxide |
| **Li** | : Lithium |
| **NiMH** | : Nickel Metal hydride batteries |
| **NiCd** | : Nickel Cadmium batteries |
| **EC** | : Ethylene carbonate |
| **DMC** | : Dimethyl carbonate |
| **$LiPF_6$** | : Lithium hexafluorophosphate |
| **$Li_2CO_3$** | : Lithium carbonate |
| **C** | : Carbon |
| **Al** | : Aluminum |
| **Bi** | : Bismuth |
| **Hg** | : Mercury |
| **Pb** | : Lead |
| **Si** | : Silicon |
| **Fe** | : Iron |
| **Ni** | : Nickel |
| **Co** | : Cobalt |
| **Sn** | : Tin |
| **Cu** | : Copper |
| **SS** | : Stainless steel |
| **ppm** | : parts per million |
| **UV** | : Ultra violet |
| **DC** | : Direct current |
| **AC** | : Alternative Current |
| **V** | : Voltage |
| **XRD** | : X-ray diffraction |
| **FEG-SEM** | **:** Field Emission Gun-Scanning Electron Microscope |
| **W** | **:** Watt |
| **GDOES** | **:** Glow Discharge Optical Emission Spectroscopy |
| **DMC** | **:** Dimethyl Carbonate |
| **CV** | **:** Cyclic Voltammetry |
| **EIS** | **:** Electrochemical Impedance Spectroscopy |

| | |
|---|---|
| **CVD** | **:** Chemical Vapor Deposition |
| **PVD** | **:** Physical Vapor Deposition |
| **TPS** | **:**Thermal Plasma Spraying |
| **HPPM** | **:** High Power Pulse Sputtering |
| **HIPIMS** | **:** High Power Impulse Magnetron Sputtering |
| **XAS** | **:** X-ray Absorption Spectroscopy |
| **TEM** | **:** Transmission Electron Microscopy |
| **HR-TEM** | **:** High Resolution Tranmission Electron Microscopy |
| **STF** | **:** Sculptured Thin Films |
| **PE** | : Polyethyelene |
| **PP** | : Poly propylene |
| **VC** | : Vinylene Carbonate |
| **FEC** | : Fluoro Ethylene Carbonate |
| **a-Si** | : Amorphous Si |
| **α-Si** | : Crystalline Si |
| **MFP** | : Mean Free Path |
| **IR** | : Impinging Rate |
| **OAD** | : Oblique Angle Deposition |
| **GLAD** | : Glancing Angle Deposition |
| **QCM** | : Quartz Crystal Microbalance |
| **IAD** | : Ion Assisted Deposition |
| **SS** | : Stainless Steel |
| **GDOES** | : Glow Discharge Optic Emission Spectroscopy |
| **Ar** | : Argone |
| **O** | : Oxygene |
| **SOC** | : State of Charges |
| **OCV** | : Open Circuit Voltage |

## LIST OF TABLES

**Page**

**LIST OF FIGURES**

**Page**

**ENGINEERING M-Si (M:Ag, Cu) THIN FILMS AS NEGATIVE ELECTRODES FOR LITHIUM ION BATTERIES**

**SUMMARY**

It is essential to use low-cost and environmentally friendly energy storage systems. In this concept, all inovations done in energy storage devices are issued from accurate material selection and process design.

In todays world, among alternative energy storage devices, lithium ion battery (LIB) becomes more important. They provide electrical power for a wide variety of applications such as power tools, aerospace and small portable electronic devices. However, current LIB technology can not satisfy the energy and power requirements of long life cell phones, electrical/hybrid vehicles and smart grids.

We consider the example of smartphones, when graphitic based LIB are used, its charge can only endure for one day. When the use of LIB in Tesla Roadster (EV) is considered, EV carries 6831 lithium ion cells which together weight half a ton in the car. However, so many cells can only cover a distance of about 450-500 km, which is around half the driving distance of a fully loaded gasoline vehicle. Taking into consideration these facts, Department of Energy (DoE, USA) and the New Energy and Industrial Technology Development Organization (NEDO, Japon) indicate that improving the battery performance with higher energy density, longer battery life and lower cost should be the priority in energy researches. Therefore, making successful development in LIB will be the strategic target to work on for nations around the world.

So far, one of the challenge substituting graphite with high capacity alternative materials has been highlighted as a crucial challenge. In this sense, the use of various materials (C, Sn, Al, Sb, Bi) has been evaluated as anodes in LIB. Among them, silicon (Si) becomes prominent due to its high theoretical storage capacity (3579 mAh $g^{-1}$ at room temperature), low operation potential (-370 mV vs $Li/Li^+$), eco friendliness, high abundance on Earth's crust and low cost comparable to those of graphite. Despite these merits of Si, it has not yet replaced graphite in commercial applications, because when lithium ions ($Li^+$) reacts with Si, more than 300% volume expansion occurs generating an immense amount of stress in the anode. This stress causes a severe material collapse and electrical isolation, resulting in low coulombic efficiency (CE) and rapidly declining capacity. Moreover, as the electrochemical alloying potential of Si is above the solvent reduction level, a passive film (solid electrolyte interphase (SEI)) forms at the electrode/electrolyte interface. Herein, it is worth to note that volume expansion in cycling yields unstable SEI between the Si surface and electrolyte, which leads to an increase in impedance. Finally, the low electrical conductivity ($10^{-3}$ S $cm^{-1}$) and low Li diffusion coefficient ($10^{-14}$-$10^{-13}$ $cm^2s^{-1}$) in Si hinder fast electron transfers resulting high resistance in the electrode, hence failure in the early stages of cycling.

To be able to use Si electrodes in electrical vehicles or other advanced technological devices, highly stress-tolerant Si anodes that would withstand massive current demands while providing high energy density should be designed.

It is known that, all potential commercial anode architectures have not been able to deliver a combination of high power and high energy density over a long range of cycles. Thus, there is a need to design LIB electrodes that can be discharged/charged at high rates to meet the high current demands of advanced technologies. At the same time, the mechanical integrity should be maintained and the production cost should be feasible. Herein, fabricating nano-structructured Si thin film by physical vapor deposition techniques becomes prominent because it is believed that delamination and quick faillure of the thin film electrodes might be prevented by using nano-engineering strategies, including nano-structuring and composition grading.

In this dissertation, taking the above-mentioned claims as motivations an original idea of engineering Si based films to be used as negative electrodes in lithium ion batteries has been proposed. Magnetron sputtering and (glancing angle) electron beam evaporation processes have been chosen as the production techniques. Magnetron sputtering is used since highly energetic sputtered particles are believed to promote the intermetalic formation along the film as well as the adhesion of the coating to the substrate, and glancing angle electron beam evaporation method has been utilized since the process enables one to design nanoarchitectured thin film with a well aligned morphology.

To overcome the above mentioned restrictions of Si based anodes some researchers are working to design new functional electrodes and others optimize the testing conditions and/or innovate cell designs. The objective of this study is to gain insights in how to design new negative electrodes for next generation LIB. The results show that both process and material science engineerings should be used to produce next generation Si based electrodes. Following this idea, in this dissertation a material selection is purposed: use of electrochemically active (Ag) or inactive elements (Cu) with Si has been evaluated. Moreover, we have also modified production processes and characterization methods: cut-off voltages of the galvanostatic tests are optimized in the first chapter, high power pulsed magnetron sputtering (HPPMS) is used to deposit Si film in the second chapter, then ion assistance is adopted to the glancing angle electron beam deposition process in the third chapter.

In this dissertation, a compositional improvement has been done by cosputtering Ag atoms with Si, in the first chapter. Ag atoms having the highest electrical conductivity among all materials are believed to create electron conductive pathways in the Si anode so that a Si based film with 3.2 microns thickness could be able to cycle with high performance. As Ag atoms are also electrochemically active versus Li, the lithiation reactions of SiAg film has been optimized by using different lower cutoff voltages in galvanostatic test. The SiAg composite electrode fails in 20 cycles when cycled between 0.005-1.2 V, whilst delivers around 1700 mAh $g^{-1}$ after 60th cycled when cycled between 0.2-1.2 V. The approach proposed in this study is believed to offer a new gateway for material science to handle both the material properties as well as the testing conditions, to increase the electrochemical performance of the new electrodes.

The fact that Ag is a heavy and expensive metal, an alternative electrochemically inactive element Cu is used in the second chapter where we fabricate functionally graded SiCu film with 2.4 micron thickness. By tuning Cu content of the film along the thickness and improving the interaction between highly energetic Si and Cu atoms, a Si based electrode with high rate capability and cycle performance has been achieved by magnetron sputtering process. Herein Cu has been particularly chosen since it is the second most conductive metal after Ag. Plus being inactive versus Li, ductile behavior of Cu is expected to improve both physical and mechanical properties of the Si based electrodes. In the experiments, HPPMS process has been used to deposit Si film without arcing. The functionally-graded Si-Cu film performs 1500 mAh $g^{-1}$ after $100^{th}$ cycle when cycled at 100 mA $g^{-1}$, and deliver roughly 700 mAh $g^{-1}$ when cycled at 500 mA $g^{-1}$. This high capacity value has been first found in the literature for such a thick film electrode. This outstanding performance of the electrode is believed to be a result of synergy gathered from its compositional, structural and morphological particularities: The highly adherent compositionally graded film has high electronic conductivity as well as mechanical tolerance against volumetric changes due to Cu atoms existence. Cu atoms provide minimum electrochemical sintering or Si particle agglomeration during cycling. Plus, as a result of the varying Cu atoms presence along the film thickness (pure Cu at the bottom and 10%at. Cu at the top) the stress propagation in the electrode during cycling is highly improved. Moreover, interspaces among the domains help to handle strain changes in cycling. Besides, amorphous and nano-sized crystalline morphology promotes the reversibility of the reactions.

And finally, in the third chapter, first in literature compositionally graded helices containing SiCu film has been produced by glancing angle electron beam evaporation method. Herein, as an innovative approach, an ion assisted deposition technique was adopted to glancing angle deposition method to increase the adhesion of the helices to the substrate. The micro-spring behavior of the helices as well as the porosity (interspaces among the helices) in the well aligned film improve the mechanical resistance of the film, while the stress propagation is improved thanks to the compositionally graded structure. This electrode delivers approximately 1200 mAh $g^{-1}$ after $100^{th}$ cycles when cycled with 100 mA $g^{-1}$ rate.

In terms of technology and development of our country, impact of researches on LIB is increasing day by day. Taking into consideration this fact, this thesis represents a supportive step for the states-of-art of anode materials used in LIB

**LİTYUM İYON BATARYALARDA NEGATİF ELEKTROT OLARAK KULLANIMLARI İÇİN M-Si (M:Ag, Cu) İNCE FİLMLERİN TASARLANMASI**

## ÖZET

Günümüzde her kesimden insanın hızlı, verimli ve kolay iletişim için taşınabilir elektronik aletlerden (bilgisayarlar, cep telefonları, kameralar, fotoğraf makinaları, MP3 çalarlar, CD çalarlar, DVD oynatıcılar, radyolar, televizyonlar) yararlandığı bilinmektedir. Taşınabilir tüm bu elektronik ürünlerin görevlerini uzun süreli ve etkin olarak sürdürebilmeleri için temel şart yüksek enerji yoğunluğuna sahip, güvenli, uzun ömürlü, bakımı kolay yapılabilen, kısa sürede şarj edilebilen ve çevreye zarar vermeyen bir enerji kaynağına sahip olmalarıdır.

Günlük kullanım ihtiyaçlarının yanı sıra özellikle taşıma sektöründe de yüksek miktarda enerjiye ihtiyaç duyulmaktadır. Tekrar şarj edilebilen/ ikincil lityum-iyon bataryalar (LİB) sahip olduğu üstün özellikler sayesinde gerek ev aletlerinde gerekse de taşıma sektöründe yaygın olarak kullanılan enerji kaynaklarından biridir.

Tekrar şarj edilebilir pil olan lityum iyon piller, ikincil piller olarak da bilinirler; deşarj olduktan sonra tekrar şarj edilerek kullanılabilen elektrokimyasal hücrelerdir. Diğer ikincil pillerle (gümüş-çinko, nikel-çinko, nikel-hidrojen) karşılaştırıldıklarında bakım gerektirmemeleri ve uzun ömürlü olmalarının yanı sıra geniş çalışma sıcaklık aralığına, uzun raf ömrüne, çabuk şarj olabilme kabiliyetine, yüksek güçlü deşarj kapasitesine, yüksek enerji verimliliğine ve yüksek spesifik enerji yoğunluğuna sahip olmaları sebebiyle de sıkça tercih edilmektedirler. Pahalı olmaları ve yüksek sıcaklıklarda hızlı bozunmaları ise sahip oldukları en büyük dezavantajlardır.

İlk olarak 1970 yılında lityum metalinin enerji uygulamalarında kullanımına ait avantajlar fark edildikten sonra 1972'de Exxon $TiS_2$ yapısında katot üreterek Li'a karşı gerçekleştirdiği ilk lityum pilini üretmiştir. Katmanlı yapıdaki sülfür içeren katot malzemelerinin uzun çevrimler boyunca kararlı kalmadığı 1980'de kanıtlandıktan sonra Goodenough ve arkadaşları metal oksitleri alternatif katot malzemesi olarak önermişlerdir. Bu öneriyi takiben 1991 yılında ilk defa Sony $LiCoO_2$'in katot, karbonun anot olarak kullanıldığı ticari LİB'ları üretmiştir. Bu hücrelerde 3,6 V üstünde potansiyel elde edilmiş, uzun çevrimler boyunca kararlılık gösteren lityum iyon pillerin üretilmesi başarılmıştır. Enerji sektöründeki artan ihtiyaçlara uygun şekilde cevap verebilmek ve çevreye en az zarar veren teknolojinin kullanımını yaygınlaştırmak için tekrar şarj edilebilen LİB'larla ilgili yapılan çalışmalar son yıllarda oldukça hız kazanmıştır. 2008 yılında dünyadaki satış miktarı 36 milyar dolar, 2013 yılında ise değeri 51 milyar dolara ulaşan LİB pazarının 2020 yılına kadar 100 milyar doları geçmesi beklenmektedir. Elektrikli araçlar bu teknolojinin gelişmesinde ayrı bir öneme sahiptir.

Tekrar şarj edilebilen LIB temel olarak anot/katot, separatör ve eletrolitten oluşmaktadır. Anot malzeme negatif elektrot, katot ise pozitif elektrot olarak görev

alır. Pilin şarj reaksiyonu sırasında dışarıdan uygulanan fazla voltajı takiben pozitif elektrottan Li iyonları ayrılır, elektrolit boyunca difüz ederek negatif elektrotun yapısına yerleşirler (interkele ederler). Bu sırada pozitif elektrottan ayrılan elektronlar akım iletici kablo vasıtasıyla anoda elektron iletirler. Deşarj reaksiyonu sırasında ise anoda geçen (interkeleeden) lityum iyonları katottaki ilk yerlerini almak üzere hareket (deinterkele) ederken, elektronlar da depolanan enerjiyi istenilen uygulama için transfer ederler. Bu reaksiyonların yüksek verimle gerçekleşebilmesi için elektrot malzemeleri yüksek elektrik iletkenliğinde, hafif ve elektrolitle uyumlu olmalıdır. Elektrot üretiminde malzemeler yüksek iletken metal folyolara lamine edilir veya folyo üzerine biriktirilir. Pil elemanlarının biraraya getirilmesi sırasında folyoların üzerindeki elektrot malzemeleri arasında gerçekleşmesi muhtemel kısa devreyi önlemek için mikro gözenekli seperatörler veya jel/katı elektrolitler kullanılarak hücre içerisinde lityum iyonlarının yer değiştirmesi sağlanmalıdır.

Dünya'da LİB performansını geliştirmek için yapılan çalışmalar hücre elemanları ve elektrot dizaynı olarak temel şekilde sınıflandırılabilir. Bu çalışmalar sonucu sadece US patent ofisinde kayıtlı 10.000'e yakın lityum iyon teknolojisi üzerine patent olduğu görülmüştür. Elektrot malzemelerinin bileşimleri (kompozit üretimi dahil olmak üzere) ve yapısal (gözenekli) özelliklerini geliştirmek üzerine çalışanların yanı sıra, elektrolit ve membran özelliklerini geliştirmek için de çalışan araştırma grupları bulunmaktadır.

Günümüzde LİB'da pozitif elektrot olarak öncelikli olarak katmanlı ($LiCoO_2$), spinel ($LiMn_2O_4$) ya da olivin ($LiFePO_4$) yapıda malzemelerin kullanımı araştırılırken, negatif elektrot (anot) malzemesi olarak öncelikle karbon (C) daha sonra kalay (Sn), alüminyum (Al), antimon (Sb), bizmut (Bi) ve silisyum (Si) esaslı malzemelerin kullanımları değerlendirilmekteditr.

Son yıllarda alternatifleri arasından Si yüksek kapasiteye sahip olması (3579 $mAsg^{-1}$ oda sıcaklığında) ve hammaddesinin dünyada bol ve ucuz bulunmasından dolayı, araştırmalarda sıkça tercih edilmektedir. Si anotunun uygulanmasında karşılaşılan en büyük sorun ise malzemenin düşük elektrik iletkenliği ($10^{-3}$ S $cm^{-1}$), düşük lityum difüzyon katsayısı ($10^{-14}$-$10^{-13}$ $cm^2s^{-1}$), lityumla reaksiyon sırasında birim hücrede gerçekleşen yüksek hacimsel (%300) değişim ve lityumla reaksiyon potansiyelinin elektrolit parçalanma potansiyel değerinin altında olması sebebiyle yüzeyinde kararlı olmayan katı elektrolit ara yüzeyi (SEI: solid electrolyte interphase) oluşturmasıdır. Bu sorunun üstesinden gelebilmek için nanokompozit elektrotların kullanımı önerilmiştir. Bu bağlamda, gümüş (Ag) ve bakır (Cu) sahip oldukları yüksek elektrik iletkenliğikleri sayesinde geçmiş çalışmalarda tercih edilmişlerdir. Böylece, Si filmin içinde bulunan bu metal atomları, lityumla reaksiyona girmedikleri şartlar altında, hem elektrotun içinde yeni elektron yolları açmasına, hem çevrim testi boyunca Si'un elektrotta oluşabilecek elektrokimyasal aglomerasyonunun engellenmesine hem de Si-Li arasında gerçekleşen reaksiyon sonucunda oluşan yüksek hacimsel değişimi mekanik tampon olarak sindirerek, hacimsel değişimin yıkıcı etkisinin azalmasına sebep olmuşlardır. Si bazlı nanokompozit malzemeler literatürde sıkça kullanılmıştır.

Lityumla reaksiyona girmeyen Cu atomları, Ag atomlarına nazaran sahip oldukları daha düşük atomik kütlelerinin yanı sıra, sergiledikleri sünek davranışları ve Si'la farklı fazlar (ör:$Cu_3Si$) meydana getirmeleri sebebiyle galvonastatik test boyunca lityumla reaksiyonlarının tersinir olmasını sağlayabileceğini de kanıtlamıştır. Dahası

Cu, negatif elektrotun akım toplayıcı Cu folyo ile arasındaki adezyonunu artırarak, yüksek çevrim ömrü ve iyi kapasite saklama özelliği kazandırdığı da kanıtlanmıştır.

Şimdiye kadar, sol-jel, elektron demeti ile buharlaştırma, iyon katkılama, kimyasal buhar çökeltme, ultrasonik radyasyon, melez büyütme teknikleri ile SiCu kompozit filmleri üretilmiştir. Bu çalışmalar sonucunda üretim yönteminin özelliklerine bağlı olarak elektrotun tane özelliklerinin ve bu yüzden de elektrokimyasal performansının değiştiği gözlemlenmiştir. Bu sebeple araştırmacılar sıfır (0D), tek (1D), iki (2D) ve üç (3D) boyutta elektrot malzemeleri üreterek, LIB'da anot malzemesi olarak kullanımları durumunda özelliklerini incelemiştir. Sonuçlar temel olarak nano boyutta üretilen elektrot malzemelerin ilk kapasitelerinin daha yüksek olduğunu ve çevrim ömürlerinin daha uzun olduğunu kanıtlamıştır. Fakat elektrotun içerisinde aktif malzemenin tane boyutunun azalması aynı zamanda ikincil reaksiyon olarak tanımlanan oksitlenme ve katı elektrolit ara yüzey filminin yüksek miktarda oluşmasına neden olmaktadır. Bu oluşum sebebiyle ilk deşarj reaksiyonu (lityumun interkele ettiği) yüksek olsa da reaksiyonun geri dönüş veriminin oldukça düşük olduğu gözlenmiştir.

Günümüzde LİB'ları elektrikli araç gibi ileri teknoloji aletlerinde kullanmak için yüksek akım yoğunluklarında verimli performans sergilemeleri en önemli gereksinimleridir. Bu noktada yüksek miktarda gerilimi tolere edebilecek yapıda Si anot üretimi oldukça önem kazanmaktadır. Bu şekilde ekonomik olarak uygun şartlarla elde edilen elektrotun çevrim testi boyunca hem mekanik olarak bütünlüğünü koruması hem de yüksek kapasite sergilemesi hedeflenmektedir.

Bu kapsamda yapılan çalışmalarda malzeme seçimi ve proses dizaynının önem kazandığı görülmektedir. Bu tezde, yukarıdaki bilgiler göz önüne alınarak yüksek kapasite-çevrim performansı sergileyen anot eldesinin hem malzeme seçimi hem de üretim proseslerinde yapılan iyileştirmeler ile eldesi hedeflenmiştir. Malzeme seçimi kapsamında Si anotların performanslarını geliştirmek için birinci başlıkta lityuma karşı aktif özellik sergileyen yüksek elektrik iletkenliğine sahip Ag, ikinci ve üçüncü başlıkta ise lityuma karşı inaktif davranış sergileyen Cu atomu ilavesiyle kompozit filmler üretilmiştir. Proses gelişimi için ise ilk başlıkta Ag atomlarının çevrim testine etkisini inceleyebilmek ve SiAg filminin en verimli çalışacağı test aralığını bulmak için farklı galvanostatik test koşullarında test uygulanmıştır. İkinci başlıkta ise geleneksel manyetik sıçratma prosesi yerine 'sürekli olmayan, şiddetli akımla manyetik sıçratma' (High power pulsed magnetron sputtering: HPPMS) yöntemi kullanılarak homojen özellikte Si film sağlanmıştır. Üçüncü başlıkta ise iyon desteğinin elektron demeti buharlaştırma prosesine adapte edilmesi sayesinde yüksek yapışma özelliğine sahip şekilli ince filmler başarıyla elde edilmiştir.

İncelenen tezin birinci bölümünde kullanılan Ag elementinin anot malzemesi olarak kullanımı üzerine yapılmış çalışmalar, Ag elementinin 0,2 V altındaki potansiyellerde lityumla reaksiyona girdiğini ortaya koymuştur. 0,005-1,2 ve 0,2-1,2 V aralığında test edilen, manyetik sıçratma yöntemiyle elde edilmiş bu kompozit film, 0,005-1,2 V aralığında 20 çevrim sonunda çok düşük kapasite değerleri sergilerken, 0,2-1,2 V aralığında test edildiğinde 60 çevrim sonunda 1700 mAsa $g^{-1}$ deşarj kapasitesi ortaya koymuştur. Bu durum 0,2-1,2 V aralığında lityumla reaksiyona girmeyen nanoboyutta dağılmış Ag atomlarının Si filmi içerisinde elektron iletimlerini sağlayacak yollar oluşturmaları ile açıklanmıştır. Ag malzemesinin pahalı ve ağır olması, Li'la reaksiyon vermeyen ve yüksek elektrik iletkenliğine sahip, daha düşük atomik kütle ağırlığındaki Cu atomlarının alternatif olarak kullanılabileceğini göstermiştir. Bu sebeple, ikinci bölümde Si elektrodun özelliklerini geliştirmek için Cu atomları film kalınlığı boyunca miktarsal dağılımları değişecek şekilde manyetik sıçratma yöntemiyle biriktirilmişlerdir. Bu başlıkta Si film üretimi sırasında ark oluşumunu engellemek ve homojen özellikte film elde etmek için HPPMS yöntemi kullanılmıştır. Üretilen film kaplama/altlık ara yüzeyinde %100 at. Cu atomları içerirken kaplama/elektrolit arayüzeyinde %10 at. Cu içerecek şekilde tasarlanmıştır. Cu atomlarının sahip oldukları yüksek elektrik iletkenliği ve süneklik çevrim testi boyunca kaplamada oluşan gerilimin dağılmasına yardımcı olmuş, yüksek performans elde edilmesi başarılmıştır. Bu sayede 100 çevrim sonunda 1500 mAsa $g^{-1}$ deşarj kapasite sergileyen anot malzemesi elde edilmiştir. Son bölüm de ise kalınlık boyunca bileşimi değiştirme yaklaşımı eğik açılı elektron demeti buharlaştırma yöntemi kullanılarak denenmiştir. Kaplamanın ilk 5 dakikasında uygulanan iyon desteği sayesinde kaplamanın altlığa yapışmasının artması beklenmiştir. Bu deneylerde eğik açılı elektron demeti buharlaştırma yönteminin seçilmesinin temel sebebi prosesin farklı nanoşekilli yapıları düzenli dizilimli olarak elde edilmesine olanak sağlıyor olmasıdır. Bu yöntem sayesinde son başlıkta bileşimi kalınlık boyunca değişen helis şekilli SiCu ince filmleirn üretimi gerçekleştirilmiş, anot malzemesi olarak kullanımları değerlendirilmiştir. Bu tasarımla helis şekli sayesinde hem mekanik mukavemetin gelişmesi, hem de Cu atomlarının kalınlık boyunca oranlarının değişmesi sonucu oluşan hacimsel değişimin neden olduğu gerilimin dağılması amaçlanmıştır. Galvanostatik test sonuçları kalınlık boyunca değişen Cu miktarı sayesinde (elektrot/akım toplayıcı ara yüzeyinde %30 at. Cu bulunurken, elektrot/elektrolit ara yüzeyinde %10 at. Cu bulunmaktadır) elektrot üzerinde oluşan stres yayılımının değiştiğini ve bu sayede 100 çevrim testi sonunda 1200 mAsa $g^{-1}$ deşarj kapasitesi sergileyebildiğini göstermiştir.

Bu tezde uygun malzeme seçimi ve proses dizaynı ile fiziksel buharlaştırma yöntemleri kullanılarak (manyetik sıçratma ve iyon destekli eğik açılı elektron demeti buharlaştırma) Si bazlı filmlerin lityum iyon bataryalarda anot malzemesi olarak kullanımları için üretilebileceği gösterilmiştir. Yapılan deneysel çalışmalara ait sonuçlar elektrot malzemesinin bileşiminin ve elektrottaki boşluk miktarının/dağılımının yüksek elektrokimyasal performans sergileyen anot malzemesi eldesinde oldukça önemli olduğunu göstermiştir. Elektrottan elde edilen yüksek performans yüksek adezyon kuvvetiyle altlığa bağlı olan ince filmin yapısal, bileşimsel ve morfolojik özellikleriyle, elektrot yüzeyinde oluşan SEI filminin kararlılığıyla ve uygulanan galvanostatik test koşullarıyla ilişkilendirilmektedir.

İçinde bulunduğumuz hızla değişen düzende ilerleyen teknolojiyi yakalamak açısından LİB teknolojisini geliştirmek için yapılacak araştırma-geliştirme faliyeteleri oldukça önemlidir. Bu amaç dikkate alındığında yapılan bu tezin LİB teknolojileri için anot geliştirilmesi yönünde araştırma-geliştirme faaliyetlerini destekleyici nitelikte sonuçlar içerdiği düşünülmektedir.

# 1. INTRODUCTION TO LITHIUM ION BATTERIES

One of the biggest challenges of the modern society is to have enough energy to meet the growing energy demand and to have a clean environment to live for.

Fossil based sources play a critical role in providing energy that runs the engine of industrialization, the evolution of Western Society during the past century. However, currently, living dependency on fossil sources is underdiscussion because if the existent pace in energy consumption continues, the world will be short of the sources before 23$^{rd}$ century [1]. Added to this, the world could become unlivable due to pollution, which will disquiet the welfare of the world in future.

During last decades, concerns about global warming due to excessive $CO_2$ emissions put polticians, researchers under a tremendous pressure on reducing air pollution. Studies have shown that stabilizing the atmospheric concentration of $CO_2$ at approximately 450 parts per million (ppm) may help to delay the most serious consequences of climate change (Fig. 1.1). For this reason the use of renewable energies such as solar and wind energies, which require efficient energy storage systems are highly recommended.

Another approach to get "clean environment to live in" is to use zero emission vehicles instead of the ones having internal combustion engines (Fig.1.1.) [2].

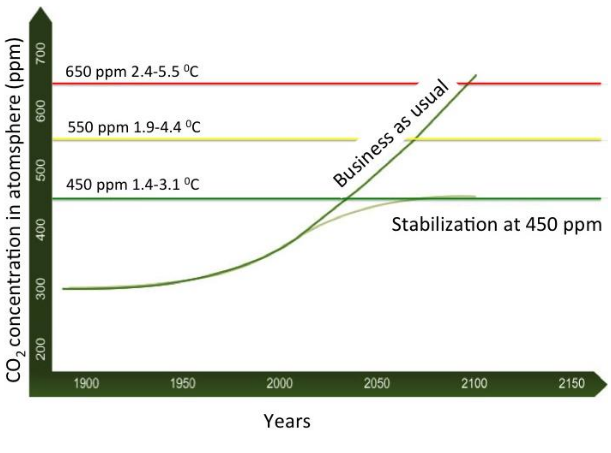


**Figure 1. 1 :** Environmental detriments caused by the use of fossil fuels [2].

Japanese was one of the early nations to commit to carbon reductions for climate policy. The foundation of the Japan government on research and development to improve EVs technology began in 1971. The Japanese government has been phasing PEV incentives since 1978. These incentives included subsidies, sales tax waivers, and leasing. Then, in 1973, Japan introduced the exigent ambient air quality standard for $NO_x$, as compared to the rest of the world. Under the Kyoto Protocol (1997), Japan committed to reduce its annual GHG emissions to 6% below 1990 levels upto 25 years (between 2008 and 2012) [3].

Japan is the home of Nissan which is the world leader in BEV development and the earliest car company to experiment with LIBs. Historically, Nissan was the leader in LIB manufacturing for consumer electronics. Statistics show that in 2009, Japan represented 57% of the global lithium-ion manufacture market share, with South Korea at 17% and China at 13%. In 2010, a government policy so named "The Next Generation Automobile Strategy 2010," was proposed including a target of installing 2,000,000 chargers and 5 000 quick chargers in the country by year 2020. As part of this policy, 356,000,000 USD were funded in 2011-12 to support this charging infrastructure goal and to provide purchase incentives to PEV consumers. In 2012, the Japanese BEV market represented 20%, and the PHEV market represented about 12% of the global market.  In 2015, the market penetration rate of PEVs is expected to be higher than 0.94%, which is a remarkable high growth value compared to the rest of the World [3].

In order to mitigate climate changes and reduce emissions, in 2009, the Ministry of Finance and Ministry of Science and Technology of China jointly prepared the Notification of Energy-Saving and Electric Vehicles Promotion in Pilot Demonstration Areas as the first specific policy to propose EV promotion. From then on, Chinese government has committed to increase the proportion of EV in vehicle market. The target of government is to hold 500 000 BEVs and HEVs by 2015, and 5 million by 2020 [4].

In 2009, US Energy Information Administration (EIA) reported that over 98% of energy consumed by transportation is originated from fossil fuels; whereas the consumption of electricity for vehicles is negligible [5]. In the same year, President Obama announced that the government founded 2.4 billions USD to develop next generation batteries and EVs. They aimed to have 1,000,000 EVs on the road by the end of 2015 [5].

The global market research has shown that though in 2011 there were only two commercial EVs (Chevrolet VOLT and Nissan LEAF) available on the US market, recently different companies have produced various EVs with different performances Fig. 1.2. shows actual and expected electrical vehicle models based on the data presented in [5] and [6]. For instance, Nissan could only travel 100 miles at a speed of 96.56 km/h (60 mph) after one single charge of 8 hours. This energy density is too low compared to that of the gaseoline. Therefore, the challenge to have more EVs on the road is to increase the energy density, cycle life and price availability of enery storage device.

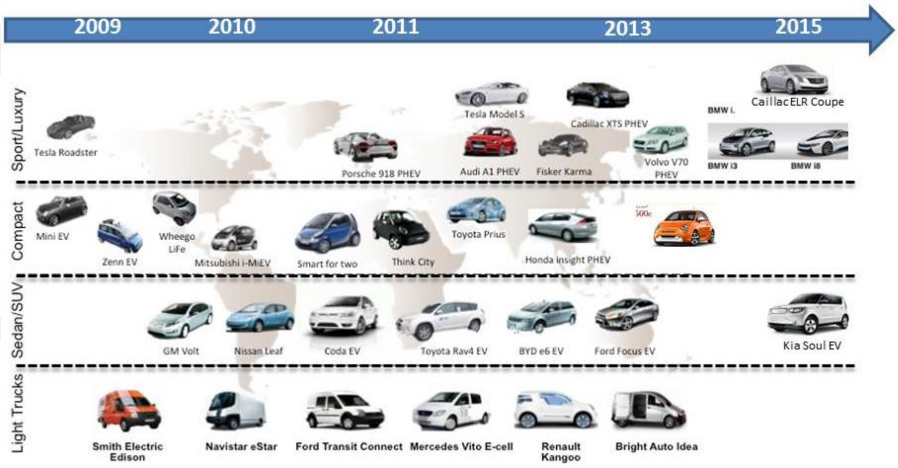


**Figure 1. 2 :** Various electrical vehicles [5,6].

Among various rechargeable batteries (Lead-acid, nickel-cadmium (NiCd), nickel metal hydride (NiMH)), LIBs that utilize the reversible lithiation/delithiation reactions to convert and store electrochemical energy have been widely used in portable electronics market (Fig. 1.3.) [7-9].

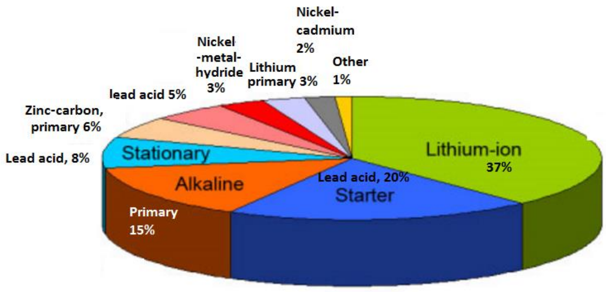


**Figure 1. 3 :** Usage level of batteries (grouped based on their chemistries) [9].

LIBs become very important among the other types of rechargeable batteries (Fig. 1.4.). Because [7-8];

- Li is one of the most electropositive elements (-3.04 V versus standard hydrogen electrode) as well as the lightest electrochemically active metal. Thus, Li based batteries can store more energy than other rechargeable batteries.

-LIBs operate at higher voltages in comparison to other batteries (e.g. 3.7 V for LIB and 1.2 V for NiMH or NiCd).

-LIBs have a lower self-discharge rate than the other types of rechargeable batteries

-LIBs have no memory effect.

-LIBs are also eco-friendly since they do not contain any toxic elements like mercury (Hg) or lead (Pb).

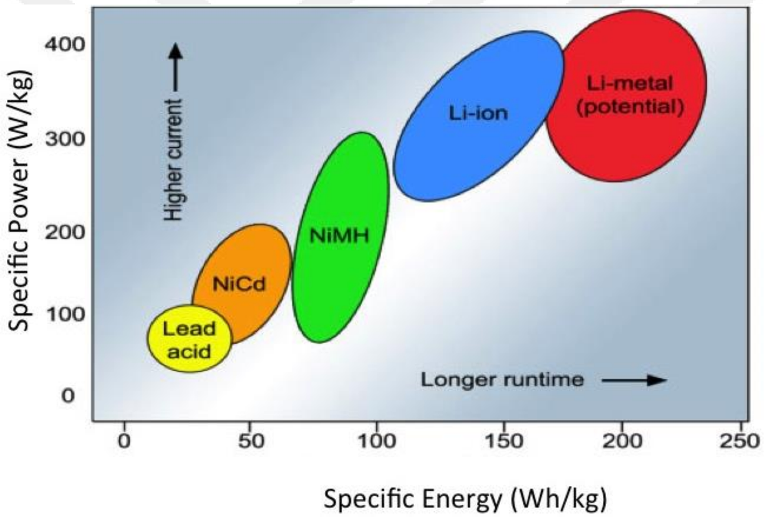


**Figure 1. 4 :** Advantages of LIB versus other rechargeable lithium batteries [9].

However, so far a LIB having outstandingly high capacity, high power and long cycle life have not been designed and produced commercially. Great efforts have been devoted for the replacement of the present commercialized cells by improving the designs, finding alternative production methods and electrode materials. Table 1.1. gives the requirements of electrodes, electrolyte and the separator to be used in next generation LIBs.

**Table 1. 1 :** Design requirements of cell components for next generation LIB.

| Anode | Cathode | Electrolyte | Seperator |
|---|---|---|---|
| High material strength | High material strength | High chemical stability | Low explosion risk |
| Structural stability | Structural stability | Cost effective | Chemical stability |
| Easy production | Easy production | Safe | Cost effective |
| High electron conductivity | High electron conductivity | High ionic conductivity | Small mesh size selective to Li |
| High Li diffusion rate | High Li diffusion rate | High Li conductivity | Environmental benign |
| Low lithiation potential | High working potential | Low flammability | |

## 1.1 Progress in Lithium Batteries Technology

Eventhough the basic principle of LIBs are dated to 1800, the explosion of the first energy crises promotes the big entrance of the technology in 1960s. At that time first Li based primary batteries were first proposed as alternative energy storage devices. In 1970, Panasonic and then Sanyo developed different primary lithium batteries for small sized devices. Since then, the battery has undergone several transformations to increase its stability and performance. In 1970s, M.S. Whittingham from Binghamton University produced lithium batteries as a result of his collaboration with Exxon. In this work, titanium sulfide (intercalation compounds) and metallic Li were used as cathode and anode materials, respectively [10]. However, because of dendritic Li growth during re-plating and subsequent explosion following oxidation prevented the widely use of this cell design. Then, in 1977, J.O Besenhard et al. [11] claimed that Li should be replaced by another compound, which ease Li insertion/de-insertion. Following this idea, in 1977 Samar Basu [12] proposed the use of graphite as a negative electrode. Then in 1980, Rachid Yazami justified the intercalation/deintercalation of Li in graphite electrode [13]. In the same year, John Goodenough from Oxford University and Kiochi Mizushime suggested to use $LiCoO_2$ as a positive electrode [14]. They believed that since the cathode material and electrolyte contain Li ions, there would be no need to use Li as electrodes.

In 1985, Akira Yoshino et al. accomplished to produce first lithium ion battery cell where $LiCoO_2$ was used as cathode and graphite as anode [15]. The commercialization of this first rechargeable LIB cell was achieved in 1991 following the cooperation between Yoshino and Sony. However, the fact that Co is hazardous for health Goodenough [16] and Thackarey [17] recommended replacing $LiCoO_2$ with $LiFePO_4$. Since then, different scientists put alternative electrode materials on the table to discuss their possible use in high-energy LIBs [18]. Among them, $LiNiO_2$ by Panasonic [19] and Si based electrode by Amprius Corp. [20] became remarkable. Nevertheless, the studies on LIBs have been exponentially increasing the best electrochemical performance has not yet been achieved.

### 1.2 Principles of Lithium Ion Battery

A battery storing chemical energy, converts it into electrical energy when it is connected to a circuit. In a battery cell, there are positive and negative electrodes: the negative electrode has a lower and the positive electrode has a higher voltage when there is no polarization. Those electrodes are named as anode and cathode. The reactions occurred in each electrode are called as half-cell reactions. An oxidation reaction (leading a loss of electrons) occurs in the anode whereas a reduction reaction (resulting a gain of electrons) happens in the cathode. For rechargeable batteries, the reactions occurring in the anode and the cathode are interchangeable, whether the battery is being charged or discharged.

As shown in Fig. 1.5, a LIB consists of an anode (negative electrode) and a cathode (positive electrode) separated by an electrolyte which only allows ions but not electrons to pass through. During charging, Li ions ($Li^+$) are released from the cathode into electrolyte (deintercalate) and are inserted into the anode. To remain charge neutrality in the electrode electrons flow from the cathode to the anode via an external circuit under an applied external electric bias. Then, in discharging $Li^+$ are extracted from the anode pass through the electrolyte, re-entering (intercalate) into the cathode providing an electric power. These reactions happen, when the material in the both electrodes are not in equilibrium. Therefore, the electrons flowing through the conductor wire can be used to power a device, as needed. When the discharge reaction is reversed the battery is charged via an external electric current. Therefore, a new reversible equilibrium conditions should be settled. In that case, electrons and positive ions will move to the negative electrode for getting the new equilibrium condition.

Therefore, during the discharging and charging processes $Li^+$ shuttles between the anode and the cathode realizing the reversible conversion and storage of electrochemical energy in the LIBs. Therefore, the working principle of the LIBs is also described as “rocking chair” [21].

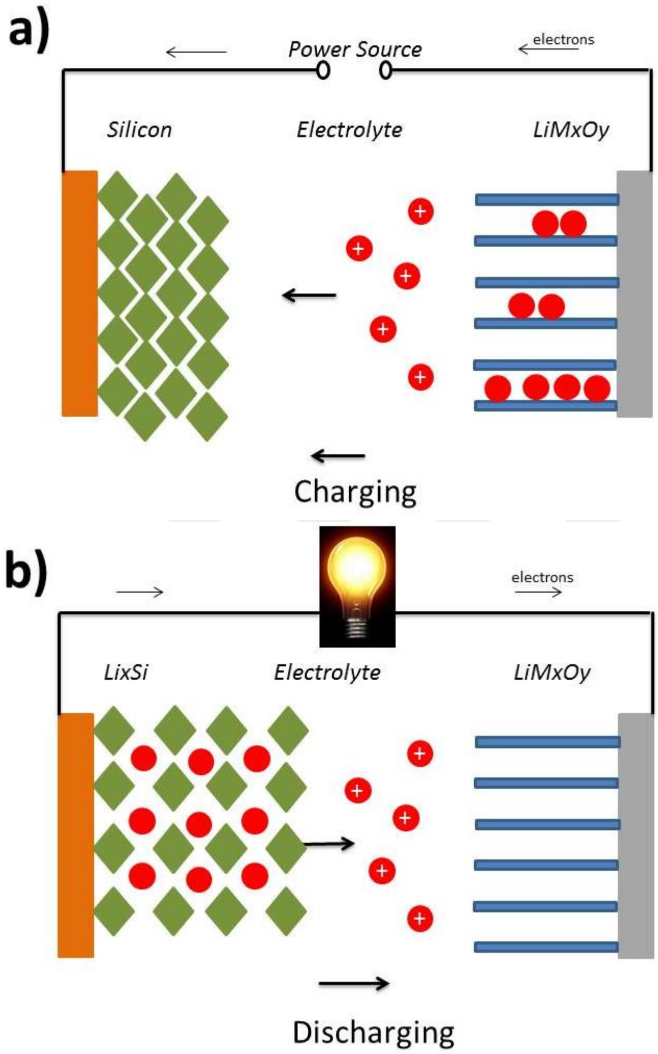


**Figure 1. 5 :** Schematic representation of lithium ion battery cell where Si is used as anode [21].

It is known that depending on the performance of a cell, the application area changes. Therefore, open circuit voltage, working potential, capacity, coulombic efficiency, and the energy density of the cell should be known. The open circuit voltage ($V_{oc}$) representing the voltage between the two terminals of the electrodes when a load is not connected, is proportional to the difference between the electrodes (cathode and the anode electrochemical potentials ($\mu_{cathode}$- $\mu_{anode}$)) (1.1). $V_{oc}$ decribes the driving forces for achieving equilibrium when the electrodes are in contact. $V_{oc}$ of LIB is typically between 3-4 V. Indeed, $V_{oc}$ is calculated by theoretical knowledge of the two electrode reactions, but these values could never be obtained in practice owing to the side reactions and other difficulties that the electrodes face in equilibrium (where F is the Faraday constant).

$$V_{oc} = \frac{(\mu_{cathode} - \mu_{anode})}{F} \quad (1.1)$$

The theoretical specific capacity of the cell is also important. It gives how much charge per gram of the material is in the cell. In more general, it represents the total quantity of electricity involved in the electrochemical reaction in term of the mass (specific capacity, mAh $g^{-1}$) or the volume (volumetric capacity, mAh $cm^{-3}$) of the active materials or the footprint area (area capacity, mA $cm^{-2}$) of the cell. The theoretical capacity of an electrode might be calculated following (1.2), where n is the mole fraction of Li in $Li_nM$ (the outer particle), 96500 is the Faraday Constant, $MM_m$ is the mass molarity of the active material (M), and y is the mass fraction of the active material in the electrode [21].

$$\text{Capacity of composite electrode} = \left(\frac{n \; x \; 96500 \; x \; 1000}{3600 \; x \; MM_M}\right) \text{ x y} \quad (1.2)$$

However, in real life only a fraction of the theoretical capacity of the tested cell is measured not only because the applied test current affects the lithiation kinetic but also other cell components increase the weight and the volume of the battery.
However, having a high capacity is not enough since the reversibility of the lithiation should be also considered to have long cycle life. Herein, the coulombic efficiency of the cell becomes important. Coulombic efficiency (1.3) is expressed as the percentage ratio between the discharge and the charge capacity of each cycle. In practice, the coulombic efficiency is always less than 100% due to irreversible loss of capacity caused by electrolyte-electrode chemical side reactions, and/or structure changes of electrode. Finally, the energy density (1.4) should also be known because it describes how much energy can be stored in terms of the mass (Wh $kg^{-1}$) or volume (Wh $l^{-1}$) of the electrode.

$$\text{Coulombic efficiency (\%)} = \frac{Capacity\ output}{Capacity\ input} \text{ x 100} \quad (1.3)$$

$$\text{Energy density} = Specific\ Capacity\ of\ the\ cell\ x\ OCV = \left(\frac{n \; x \; 96500 \; x \; 1000}{3600 \; x \; MM_M}\right) \text{xOCV} \quad (1.4)$$

## 1.3 Cell Components

### 1.3.1. Seperator

Seperator is an important component of the battery cell since it prevents the physical contact of the positive and the negative electrodes while permitting free ionic transport within the battery [22]. Thus, safety is closely related to the thermal stability of the separator. Different materials such as polyethylene (PE), polypropylene (PP), or various combinations [23] have been used to produce seperators. The fact that thermal stability of the polymer is weak at high temperatures, different materials have been evaluated to replace current polymers. It is also possible that some types of separators are not compatible with some electrolytes. For instance, polyolefins have high hydrophobicity and low surface energy resulting in low efficiency during cycling [24].

### 1.3.2. Electrolyte

In LIB the main charge/discharge voltage remains beyond 3 V, thus an aqueous electrolyte can not be used. Instead inorganic salts dissolved in organic liquids are considered as possible electrolytes. The solvent composition is chosen to achieve a satisfying viscosity, an ability to form a stable passivation layer on the electrode, and a sufficiently high dielectric constant to dissolve Li salts (such as lithium hexafluorophosphate ($LiPF_6$)). Moreover, as mentioned in Table 1.1. the electrolyte should have high ionic conductivity, high chemical stability, and be safe as well as cost-effective. Considering the working temperature of LIB (-20 to +60$^0$C) the solvent should have low melting point, high boiling point and low vapor pressure. In most common applications, a mixture of cyclic carbonic acid ester ethylene carbonate (EC, with high dielectric constant and viscosity) and chain-like ester dimethyl carbonate (DMC, with low dielectric constant and viscosity) is used [25]. Knowing that in the electrolyte lithium hexafluorophosphate ($LiPF_6$) is dissolved in solvent mixtures including ethylene carbonate (EC), dimethyl carbonate (DMC) and ethyl methyl carbonate (EMC) the working potential should be carefully chosen. It is essential for the electrolyte to have oxidation potential greater than cathode’s charge and discharge potential to prevent detrimental oxidation reaction in cycling. For a standard liquid electrolyte such as 1 M $LiPF_6$ in EC/EMC mixture, the lower limited potential to avoid electrolyte reduction is approximately 1.5 V vs. $Li/Li^+$, while the upper limit is usually between 4.2 and 5 V vs. $Li/Li^+$. The latter prevents the use of high voltage cathode materials (such as $LiNiPO_4$). However, the electrochemical potential of the most anode materials (such as C, Si etc.) is lower than the reduction potential of the standard liquid electrolyte. This causes a thermodynamically unstable interface formation between the electrode and the electrolyte as a result of the electrolyte decomposition. An insoluble Li-ion salts film will be formed on the surface of the electrodes, which is well known as solid electrolyte interphase (SEI) layer. The stability of this oxide layer is a key factor to obtain a high performance battery with long cycling life. In recent studies, some surface-active additives such as vinylene carbonate (VC) [26] or fluoroethylene carbonate (FEC) [27] have been used to enhance the formation of the highly stable passivating layer. The advantage of lithium carbonate ($Li_2CO_3$) additive to protect the surface of the electrode has been also shown [28]. It has been stated, the conventional liquid electrolytes have other drawbacks such as its high flammability, hazard to environment and human health [29]. Therefore, recently considerable effort is devoted to replace the unsafe liquid organic electrolyte with solvent-free solid electrolyte.

### 1.3.3. Cathode

Many different cathode materials have been used in literature: olivine type ($LiMPO_4$ (M=Fe, Ni, Co, Mn)), layered type ($LiCoO_2$) and spinel type ($LiNi_{0.5}Mn_{1.5}O_4$) electrodes (Fig. 1.6.). Spinel and olivine type electrodes are used for their high energy densities, layered type electrodes are used for its long cycle life [30]. Among various cathode materials, spinel $LiNi_{0.5}Mn_{1.5}O_4$ delivers a specific capacity of ~130 mA h $g^{-1}$ with high redox potential at 4.7-4.8 V vs. $Li/Li^+$. This makes it suitable for high-power applications such as electric vehicles [31]. Its three-dimensional (3D) network for Li-ion diffusion facilitates the fast Li insertion/extraction reactions. However, the formation of $Li_xNi_{1-x}O$ as a second phase, the dissolution of Mn ions from the electrode and the decomposition of the conversional liquid electrolyte on the electrode surface at high charge potential restrict its use [31-33] (Fig.1.6.).

The comparison of different cathode materials based on their crystal structure, specific capacity and their lithiation reactions are given in Table 1.2. [33,34]

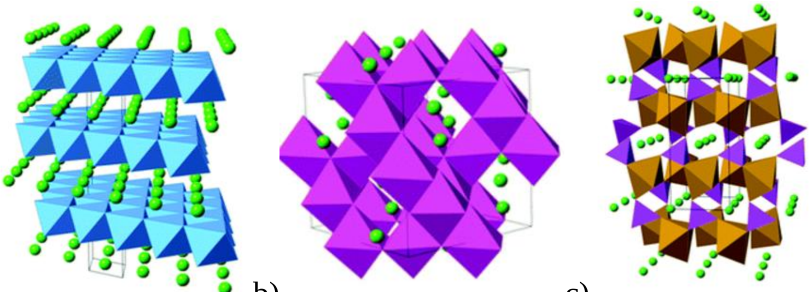

a) b) c)

**Figure 1. 6 :** Schematic representation of different structured cathode materials a) layered structured, b) spinel structured, c) olivine structured [34].

**Table 1. 2 :** Examples of cathode materials, their group and the approximate capacity range they have been reported to exhibit [33,34].

| Material | Group/structure | Specific Capacity ($mAhg^{-1}$) | Lithiation potential of the electrodes (vs Li/Li+) |
|---|---|---|---|
| $LiFePO_4$ | Olivine | 100-160 | 3.45 |
| $LiCoO_2$ | Layered | 70-140 | 3.9 |
| $LiMn_2O_4$ | Spinel | 80-155 | 4.1 |
| $Li(Ni_{0.33}Mn_{0.33}Co_{0.33}O_2)$ | Spinel | 80-160 | 3.8 |

### 1.3.4. Anode

Fig. 1.7. shows the evaluation of anode materials used in literature. First, Li metal was used as anode material due to its low electrode potential (-3.045 V vs standart hydrogen electrode (SHE)), low density (0.535 g $cm^{-3}$) and atomic weight (6.939 g $mol^{-1}$). However safety concerns (upon continuous charge and discharges dendrites form on Li surface causing short circuit, plus Li is too reactive for air) cause a replacement of Li by graphite. Eventhough graphite is stable and safe with a theoretical specific capacity of 372 mAh $g^{-1}$, it can not satisfy the high energy density requirement. Therefore, different materials have been proposed (Table 1.3) [35]. For most cases, the lithiation potentials of anode materials are lower than the reduction potential of the electrolyte. Thus, SEI layer forms on the anode surface, with a consumption of $Li^+$ leading to a lower coulombic efficiency in first cycles. To resolve this, lithium titanate ($Li_4Ti_5O_{12}$) of which lithiation potential is around ~1.55 V vs. $Li^+$/Li, is used. Therefore, there is no SEI layer formed on the $Li_4Ti_5O_{12}$ surface during the discharging/charging process. However, the specific capacity of this material is quite low (theoretical capacity of 175 mA h $g^{-1}$), hence impedes its practical uses in high energy density LIBs. Among other alternatives Sn or Si-based alloys or their composites become more promising as anodes because of their high

specific capacities which are expected to increase the cell energy density (Table 1.3) [35].

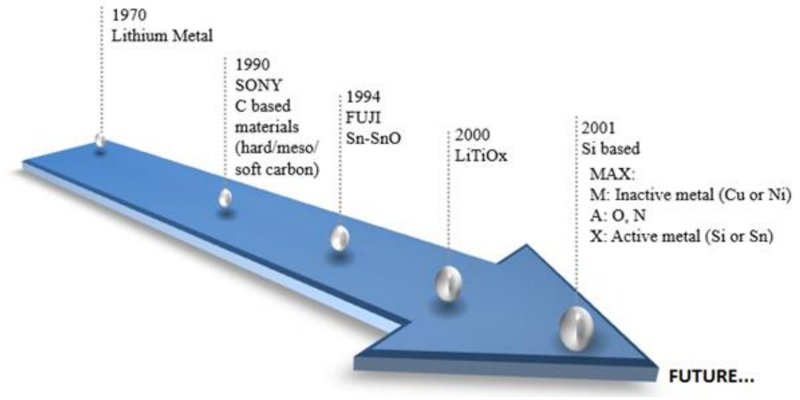


**Figure 1. 7 :** Evaluation of anode materials since 1970.

**Table 1. 3 :** Properties of alternative anode material used in literature [35].

| Material Properties | Li | C | $Li_4Ti_5O_{12}$ | Si | Sn | Sb | Al | Mg |
|---|---|---|---|---|---|---|---|---|
| Density (g cm$^{-3}$) | 0.53 | 2.25 | 3.5 | 2.33 | 7.29 | 6.7 | 2.7 | 1.3 |
| Lithiated phase | Li | $LiC_6$ | $Li_7Ti_5O_{12}$ | $Li_{4.4}Si$ | $Li_{4.4}Sn$ | $Li_3Sb$ | LiAl | $Li_3Mg$ |
| Theoretical capacity | 3862 | 372 | 175 | 4200 | 994 | 660 | 993 | 3350 |
| Volume change (%) | 100 | 12 | 1 | 400 | 260 | 200 | 96 | 100 |
| Potential vs Li/Li+ | 0.0 | 0.05 | 1.6 | 0.4 | 0.6 | 0.9 | 0.3 | 0.1 |

Attaining a very high energy from the negative electrode is not enough for commercialization of the cell, since the overall cell energy density depends on both the capacities of the anode and the cathode materials. Fig. 1.8. shows that current technology restricts the cell capacity mostly because of the low cathode material's capacity. Fig.1.8.a shows the change in the cell capacity vs anode capacity when the cathode capacity is 140 mAh $g^{-1}$ and Fig.8.b shows the changes in the cell capacity vs the anode, when the cathode has a capacity of 250 mAh $g^{-1}$. Both graphes reveal that in the present technology, producing an anode material with 1000 mAh $g^{-1}$ with a high coulombic efficiency and cycle stability is more useful and reasonable than producing an anode material with a very high capacity (i.e. 3579 mAh $g^{-1}$, theoretical capacity of Si), since the overall cell capacity does not increase remarkably afterwards.

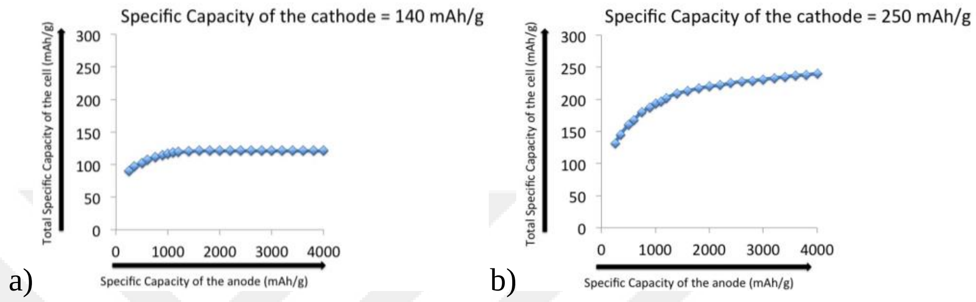


**Figure 1. 8 :** The relation between electrode's capacities and the cell capacity a) with a cathode having 140 $mAhg^{-1}$, b) with a cathode having 250 $mAhg^{-1}$ specific capacity.

Moreover, for commercial applications cell should also accomplish the cycle life test without failure (over 500 cycles for portable electronics and thousands cycles for electronic vehicles). However, a continuous decay in capacity during cycling is experienced. In recent decades, with the help of advanced characterization techniques, researchers try to understand the main reason behind this. Consequently, designing an alternative anode with high structural stability delivering capacity around 1000 mAh $g^{-1}$ becomes a noticeable topic to work on for both academic and industrial society [35].

While examining the electrochemical properties of an anode material, the importance of cost should not be underestimated. For the electrode materials, the cost is mainly dependent on its abundance, renewability, and its synthesis process. On the other hand, the hazards from electrode materials to environment and human health are another important consideration for researchers. Thus, low toxic and environment friendly materials are preferable as candidates.

As a summary, the design cirteria to fabricate the best anode for LIB could be divided in four subclasses: properties, structure, performance and process. Once the best anode material is chosen, its structure should be defined. The composite and/or nano-sized anodes could facilitate volumetric changes to perform better. To produce such structured electrode the production process should be carefully chosen to have mechanically stable, high energy density anode being able to be fabricated in mass production with a feasible cost (Fig.1.9).

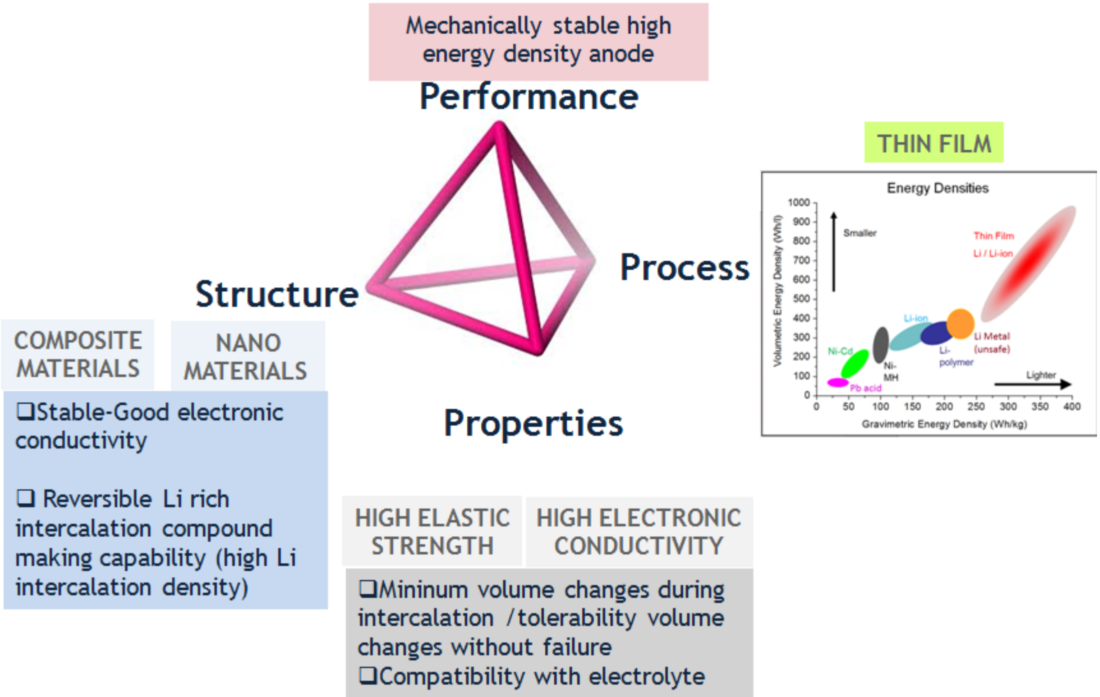


**Figure 1. 9 :** Design criteria for for anodes in LIB.

Considering all the above-mentioned properties of the ideal negative electrode, Si having high specific capacity is considered as a good candidate for next generation batteries. However, the high volume expansion and low electronic conductivity of Si prevent its wide use in commercial applications. The high volume changes in cycling introduce severe strain into the electrodes. Plus, the volume change could also damage the SEI layer leading to an unstable electrode/electrolyte interface in cycling. Moreover, lower electrical conductivity increases the resistance to transport resulting in a low rate performance. Therefore, to lower the destructive effect of high volume change and increase the electronic conductivity, the introduction of additives, doping with other elements, surface coating with electrical conductors or reducing the dimension or particle size of the electrode have been used [37-38].

In this disertation our motivation is to make accurate material selection and process desing to benefit the advantages of silicon without having quick failure problem. In the next chapter, more detailed explanation about Si anode material will be given.

## 2. SILICON BASED ANODE MATERIALS

Limited capacity of the graphite (372 mAh $g^{-1}$) can not meet the growing power requirements of consumers. Therefore, many researchers have been working to replace the graphite anode with new materials that form alloys with Li [39, 40]. As mentioned previously, among them, Si is especially attractive.

Fig. 2.1. shows the Li-Si phase diagram [41]. The stoichiometry of the four lithium rich intermetallic phases of the Li-Si system was first determined by Wen and Huggins [41]. An assessment of the Li rich part of the phase diagram from experimental and thermodynamical data was published by van der Marcel et al. [42].

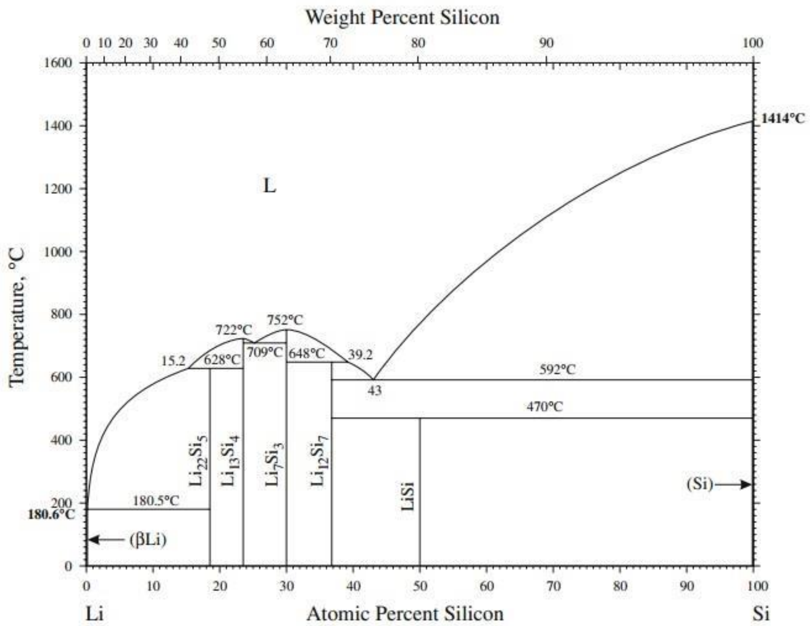


**Figure 2. 1 :** Si-Li phase diagram [41].

These preliminary studies have shown that Si is electrochemically active material versus Li. Further, galvanostatic tests show that Si can deliver a capacity upto 4200 mAh $g^{-1}$ (at high temperature) depending on the x amount in $Li_xSi$ particles. Beside this high theoretical capacity of Si, its low average discharge potential (~0.4 V) versus $Li/Li^+$ and its high abundance in the Earth's crust [41-43] make Si an attractive negative electrode material for LIB. Moreover, the fabrication technology of Si is mature. Thus, the cost of Si-based LIB is expected to be relatively low in future. Despite these attractive features, the commercialization of the Si anode has been impeded due to its poor cycle performance associated with intrinsic low conductivity ($10^{-3}$ S $cm^{-1}$), slow Li diffusion (the diffusion coefficient of Li in Si is about $10^{-13}$ $cm^2/s$), severe volume changes (as much as 400 % at high temperature) upon cycling, and unstable solid-electrolyte interphase (SEI) formation following electrolyte reduction on its surface [43, 44]. As a result, agglomeration (to form bulky structure), pulverization, cracking and/or delamination may occur in the electrode, resulting in lost of contact of the Si with other materials within the anode as well as contact loss between the anode and the current collector. Consequently, Si has irreversible capacity loss, unstable performance and quick failure. P. Hovington et al. [45] have analyzed the morphological changes of Si anodes upon cycling by in-situ and ex-situ scanning electron microscopy (SEM) and have justified that besides SEI formation, Li entrapment in the Si electrode represents another reason to explain the significant capacity loss of Si anode. Depending on the crystal structure of the Si, once an electrochemically driven amorphization occurs in the first cycle, it creates many defects (including dangling bonds) that have a strong affitinity to capture Li. The substituted Li in Si electrode can be stayed stable up to $670^0$C, which proves the difficulty to extract all Li from the Si particles in cycling.

Table 2.1 summarizes the disadvantages of Si anode, the reason of these disadvantages and their effects on the electrochemical performances, briefly.

**Table 2. 1 :** The disadvantages of Si anode and their effects on the electrochemical performance.

| Intrinsic Properties/ Causes | Results/ Problems | Consequences/ Performances |
|---|---|---|
| Surface oxidation | Lost of electronic contact | Low coulombic efficiency |
| Low electrical conductivity | Peel-off | Low capacity retention |
| Low Li diffusion coefficient | Li trapping | Low rate performance |
| SEI formation | Electrochemical agglomeration | Low volumetric energy density |
| Volume variations upon cycling | Pulverization | Quick faillure |
| | SEI decomposition<br>Cracking | |

### 2.1. Electrochemical Lithiation of Si Anodes

Electrochemical reaction between Li and Si at high temperature is given in Fig. 2.2. Lithium-silicon alloys with different stoichiometric ratios are reported during the electrochemical lithiation of Si at elevated temperatures (around 400-500$^0$C) (Fig. 2.1). In parallel with the Li-Si phase diagram 4 crystalline Li-Si phases exist: $Li_{12}Si_7$, $Li_{14}Si_6$, $Li_{13}Si_4$ and $Li_{22}Si_5$ (Fig. 2.1.). As Huggins has indicated their existences are also justified as distinct voltage plateaus in Fig. 2.2 [46]. However, the electrochemical lithiation reaction of Si at room temperature is still under discussion depending on the crystalline state of Si in the electrode.

Figs. 2.3. and 2.4. give the voltage-capacity and its differential capacity vs voltage curvatures for Si, respectively. It is denoted that amorphous (a) $Li_xSi$ forms once crystalline (α-Si) Si starts to react with Li (I). Then (II) shows that $Li_{15}Si_4$ forms when α-Si reacts with Li at the cell voltage below 50 mV. In delithiation, previously formed $Li_{15}Si_4$ transforms back into a-$Li_xSi$. Then once all Li is removed from the Si electrode, the remained-Si is found to be amorphous. Therefore, the delithiation reaction of $Li_{15}Si_4$ is found to be a two-phase reaction (III). On the other hand, when a-Si is lithiated the curve reveal two slopping plateaus marked as (IV) in Fig. 2.3. and (IVa) and (IVb) in Fig. 2.4. These plateaus point out that two phases are present during the lithiation of a-Si: first reveals the Li-Si interaction where all inserted $Li^+$ have Si as the nearest neighbor and the second shows the Li-Si interaction where the inserted $Li^+$ have $Li^+$ as the nearest neighbor atoms. During delithation reversible peaks ($V_a$) and ($V_b$) are found in Fig.2.4.

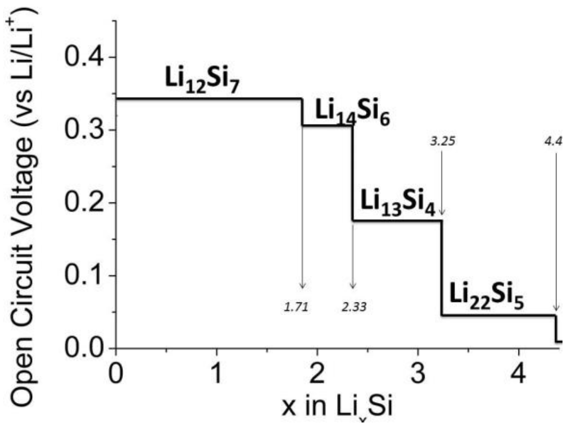


**Figure 2. 2 :** Silicon lithiation showing two phase plateaus at 415 $^0$C [46].

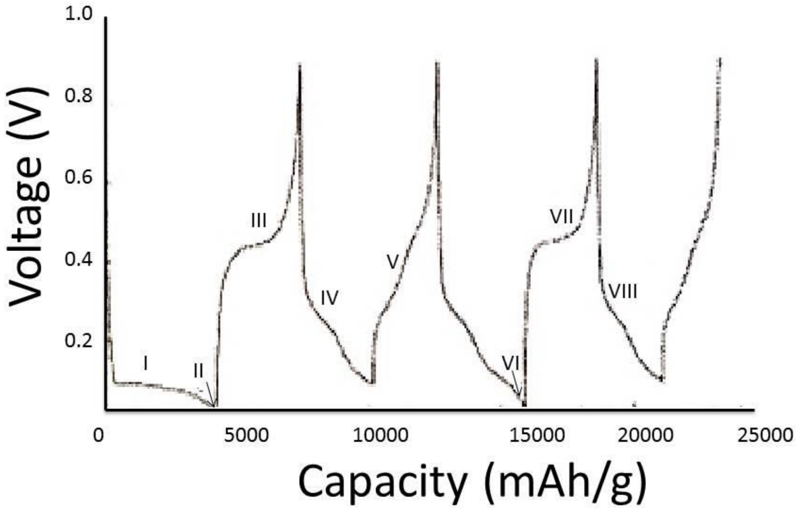


**Figure 2. 3 :** Voltage vs Capacity curve for Si. The curve indicates reactions occurring during cycling [47].

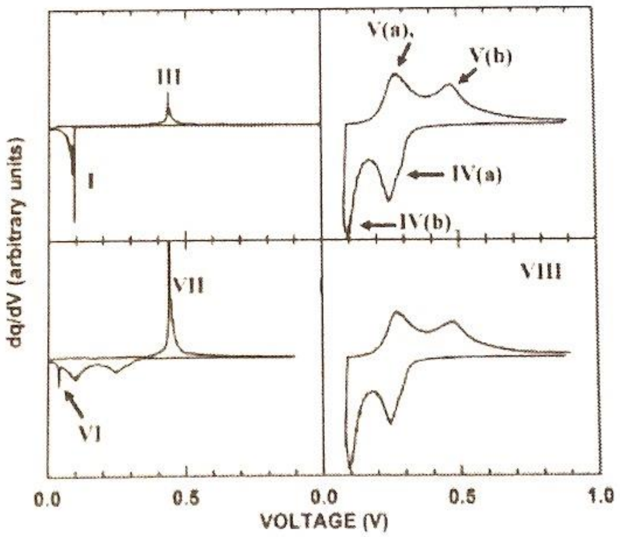


**Figure 2. 4 :** Differential capacity vs voltage for the curve presented in Fig. 2.3 [47].

These results show that electrochemical insertion of $Li^+$ into α-Si destroys its crystal structure which brings about the formation of an amorphous alloy [47]. As a consequence, a two phase compound is detected to be stable until all Si transforms into a-$Li_xSi$ form (when the cell voltage is higher than 60 mV). However, when the cell voltage is below 50 mV then all Si transforms into crystalline $Li_{15}Si_4$ [48-50]. It is worth to note that contrary to the Li-Si phase diagram that shows multiple Li-Si phase, both ex-situ and in-situ X-ray diffraction studies revealed a decrease and disappearance of α-Si peaks during the first Li insertion, while no peak was detected corresponding to the equilibrium Li-Si phases [47,51-54]. Previous in-situ XRD, SEM and high-resolution transmission electron microscopy (HR-TEM) have revealed that lithiated Si is formed primarily as amorphous phase [51]. A change in slope indicating a new Li-Si phase formation is only remarkable when the cell is discharged with a very low rate (C/100). In 2004 Obravac et al. [52] have reported the formation of a new crsytalline phase ($Li_{15}Si_4$) when the cell potential goes down to 50 mV vs $Li/Li^+$. Then in 2004, Hatchard et al. [54] have confirmed that α-Si as well as a-Si thin film anodes form $Li_{15}Si_4$ when the cell voltages goes below 50 mV. These researches have proved that rather than $Li_{22}Si_5$ phase, $Li_{15}Si_4$ is the terminal phase when Si is discharged near to zero potential at room temperature. Herein it is worth to note that in 2013 Abel et al. [55] have corrected this fact by indicating that this phenomenon is particle-size dependent and some morphologies do not crystallize even when held at 0 V for a long time. However, if the cell is not discharged lower than 50 mV, the formation of $Li_{15}Si_4$ will be bypassed no matter the particle sizes (Fig.2.3.).

Lithiation mechanism of a-Si demonstrates different features then that of α-Si at room temperature. When cycled at very low rate Maranchi et al [56] have shown that the a-Si has remarkable cathodic peaks around 0.25 and 0.1 V in addition to peak around 30 mV showing the formation of $Li_{15}Si_4$ (Fig. 2.4). Though for the α-Si the lithiation starts around 0.1 V and a peak around 50 mV becomes remarkable to demonstrate the formation of $Li_{15}Si_4$. In the charge reaction (delithiation) an anodic peak around 0.45 V is noted to show the conversion of $Li_{15}Si_4$ to amorphous $Li_xSi$. In comparison, when the a-Si thin film anode is cycled with a higher rate two broad bumps at 0.3 and 0.5V are noted, of which existences are related to the transition between different a-$Li_xSi$ phases (Fig.2.4.) [57].

Because amorphous materials experience isotropic material stress during volumetric changes, use of a-Si wihout crystal transformation is beneficial for reducing the risk of fracturing during cycling. Therefore, by limiting the upper and lower cut-off voltages, amorphous to cystalline transition can be avoided, increasing the reversibility and the coulombic efficiency of the electrode. By controlling the states of charges/discharges the degree of lithiation and volumetric growth can be also controlled, which restrict electrode pulverization in some degree.

Beside crystal structure, the SEI formation on the Si electrode is also very crucial for the electrochemical performance. It is formed following the decomposition of the electrolyte components at the interface between the electrode and the electrolyte. When $Li^+$ travel towards the anode through the electrolyte, they react with this degradation products and form solid parts on the anode surface. Indeed, the SEI layer is very thin (30-50 nm) and contains inorganic and organic products deposited on the anode surface during cycling. SEI layer being electrically insulator inhibits the electron transfer between the electrode and the electrolyte. A well-formed SEI is impermeable to solvent, but allows migration of $Li^+$ between the solvent and active species. Thus, SEI affects the kinetic of $Li^+$ transfer, hence achievable rate of charge and discharge reaction. Although SEI causes initial irreversible reaction, a stable SEI film existence on the top of the anode helps to retain the electrode integrity by providing stable electrode/electrolyte interface, hence avoiding further SEI thickening on the electrode.

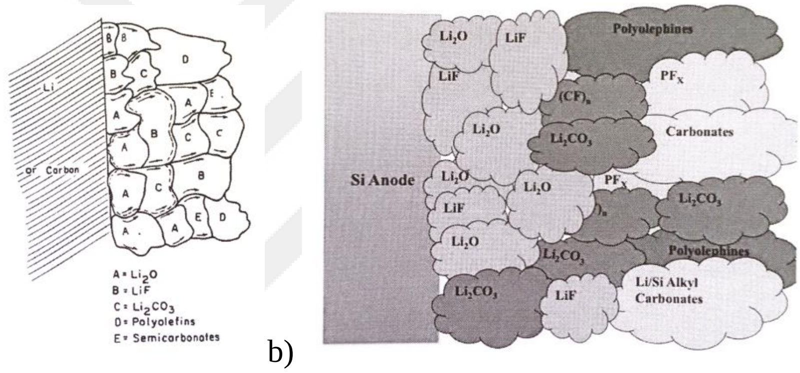


a) b)

**Figure 2. 5 :** Schematic of the solid electrolyte interphase formed on a) the graphite, b) the Si anode [58].

The SEI formation on the graphite has been widely studied in the past [57-58]. Based on these analyses, when a standard electrolyte of EC:DEC is used, the SEI is mainly composed of lithium oxides, lithium salts and other carbonates. A schematic representation of the SEI on a graphite or Li metal is shown in Fig. 2.5a as proposed by Peled et al. [58]. Lithium oxides, lithium fluoride and lithium carbonates are attached close to anode surface within the SEI layer, whilst other organic compounds such as polyolefins and semicarbonates are near the electrolyte phase. On the other hand, SEI formation on Si anodes is significantly different from the typically formed SEI of the graphite for two main reasons (Fig.2.5.b) :

- Si surface is more reactive than graphite. The SEI on Si electrode is more complex and includes hydrocarbons ($C_2H_5OCOOLi$, $LiCO_3$, $Li_2O$, LiF) and Si containing products ($SiF_6^{-2}$).

- As SEI layer does not undergo any expansion, high volume changes of Si in cycling causes break up of the SEI and exposes fresh reactive Si to the electrolyte.

## 2.2.Improving Electrochemical Performance of Si Anodes for LIB

Adjusting the cut off voltages, modifying the surface of the electrode, changing the electrolyte composition, increasing the contact area and addition of different elements in the Si electrode are possible solutions to improve the performance.

As the amorphous $Li_xSi$ formation from α-Si starts around 120 mV, by limiting the low cut off voltage to a value higher than 0.1 V both the structural and morphological stabilities of the electrode are expected to ameliorate because only the a-Si particles would be cycled. In addition, surface modifications, particularly surface coating of electrode by conductive polymer coating [59], Ag [60], Sn [61] and metaloxide [62] have been also shown to improve the performance of LIB electrodes. It is believed that surface modifications may suppress metal dissolution by reacting with residual trace-amounts of HF in the electrolyte, plus it may also change the interfacial kinetics, improve surface conductivity, and act as mechanical protecting layers. To improve the cycle performance of the Si electrode, some scientists have modified the electrolyte compositon as well. Knowing that ethylene carbonate (EC) is usually part of the solvent mixture due its high dielectric constant and the ability to form stable SEI on graphite, lithium bis (oxalato) (LIBOB) is added to improve the cycling stability by encouring non-porous SEI film formation. However, the fact that LIBOB has lower ionic conductivity, so internal resistance increases the polarization, which prevents its widely used in commercial applications [63]. Instead, vinylene carbonate (VC) or Fluoroethylene carbonate (FEC) is widely used to get stable performance. Because, VC is reduced at higher potentials than those of EC. This can greatly influence SEI composition directly [64]. Moreover, FEC is also used to increase the coulombic efficiency as it helps to have a stable electrode/electrolyte interface. It has been also suggested that the additive in the electrolyte may encourage the formation of a more stable SEI or enable faster selfhealing of this oxide layer. Recently, silane based additives such as monomethoxy trimethyl silane has been also recommended to be added into the electrolyte to decrease the extent of SEI formation [64-65].

Other than those mentioned above, researches on morphological and compositional improvements emphasize the importance of nanotechnology to increase the electrochemical performance of the electrodes (Table 2.2).

**Table 2. 2 :** Solutions proposed to overcome the disadvantages of Si anodes.

| Morphological | Compositional |
|---|---|
| Control the crystal morphology | Addition of inactive element |
| Induce porosities | Insertion of Si in a conductive matrix |
| Increase the surface area | Alloying Si with an active material |

### 2.2.1. Use of nanostructured electrodes for LIBs

In recent years, to reduce the intensive stresses induced by the volume expansion of Si anodes nano engineering approaches have been studied. The results have revealed that the mechanical performance of the nanostructured electrode would be higher than those macroscopic ones.

However, for the nanostructured electrodes in most cases, eventhough the initial capacity is very high, the first cycles coulombic efficiencies are found to be low. This prevents their widely uses in commercial applications.

The use of different nanostructured Si electrode in LIBs the structure depending on sizes has been clasified as zero, one-, two-, and three-dimension.

*Zero-Dimensional Silicon Nanoparticles:* The galvanostatic test results of micron sized Si powders have been shown to lose over 90% of their initial capacity within 5 cycles [66-67]. Main reasons of the failure are delamination, irreversible capacity loss and poor electrical conductivity because of a discontinuos current pathway. Previous works show that by generating nano-sized particles (1-100 nm diameters) the performance of the electrode has been improved. Because nano-sized particles result in a low number of atoms in a grain, less volume changes in cycling, and lower mechanical stress within the particles. Plus, the existence of large number of grain boundaries acts as active sites for Li insertion/deinsertion. Therefore, the nanosizing makes the material more reactive and reduces energy barriers for alloy formation [68-70]. Moreover, small particle size provides shorter diffusion path for the transport of Li and electrons leading to a good performance at higher discharge/charge rates. Finally, the superplastic deformation behavior has been found to be higher for small sized particles, which promotes a better accommodation of strain generated by large volume changes. The superior mechanical resistance of the small-sized particles to fracture can be also explained by the formation of small sized cracks of which magnitude do not reach the critical sizes for propagation, as they do in bulk materials [70]. In 2012, Yang et al. [71] have confirmed that the nanoscale fracture and deformation mechanisms could be different from those macroscopic ones. They have proved that many materials at nanoscale are more ductile than those of micron-sized [71]. For example, bulk Si is brittle and fracture easily, but the strength of Si reaches to the theoretical value when Si is in nanometer size.

In 2003, Graetz and coworkers compared cycling performance of Si nanocrystals (nanoparticles are around 5-20 nm), Si thin films (100 nm), bulk Si and graphite [72]. They have found that the morphologies of nanoscale Si is important since it can shorten the length of the diffusion pathway thus improve Li reaction rate eventually. Moreover, they have claimed that the nano-structured Si film having no inactive binders has higher specific capacity. The nanostructured films attached to the substrate surface can efficiently release the stress induced by the expansion of particles by moving vertical direction (up-down). Additionally, they have shown that the thin film deposition methods provided good uniformity, optimum adhesion between the films and the current collectors, which would be expected to maintain good electrical contact in cycling. Thus, providing improved cycling stability and cycle life.

Although there are many advantages of nanomaterials, generation of uncontrolled side reactions, difficulty in producing and controlling the size endanger the stability of electrodes in cycling. Plus, since the binding and conductive additives increase the electrode mass, the achievable capacity would be low. Therefore, decreasing the particle size is not enough to improve the electrode performance [72] alternative Si structures have to be examined as anode materials.

*One-Dimensional Silicon Nanowires (Si NWs):* Silicon nanowires can be produced by vapor-liquid-solid, solution-liquid-solid, physical thermal deposition, chemical vapor deposition, molecular beam epitaxy and laser ablation method. It is also possible to use patterns or nanolithography to get Si nanowires [43]. It is believed that the nanowire formation can effectively avoid the pulverization of Si by providing facile strain relaxation. In 2001, Yu et al. [73] have used solid-liquid-solid method; in 2004 Kolb et al. [74] have evaporated SiO in an inert gas atmosphere using gold coated Si wafer as substrate; in 2006 Chang et al. [75] have heat-treated iron-catalyst Si nanopowder at $980^0$C. However, no electrochemical performances of these coatings have been given. Then in 2008, Chan et al [69] prepared Si NWS (diameter < 100 nm) by CVD method on gold-coated stainless steel discs. The electrode delivered 75% coulombic efficiency in the $1^{st}$ cycle. The shortened Li transport distance in the Si nanostructure and the low ohmic resistance (to the current collector) are believed to be the main reasons for it.

Herein to minimize cracking and electrochemical sintering, the size of particles should be very small. The particle diameter needs to be lower than 150 nm for nanowires. The contact surface area between the anode and the electrolyte is much smaller than zero dimensional structures, resulting in lower energy density.

*Two-Dimensional Silicon Thin Films:* The improved electrochemical performance of the thin film anode was mostly linked to its good adhesion, thickness, electrical conductivity and crystal structure.

Film thickness is important for Si thin film electrode because an increase in film thickness induces stress during deposition. If the internal stress of the film is too high then the coating would be delaminated from the substrate before cycling test. Therefore, to improve the adhesion of the coating Yonezu et al [76] have tried to increase the roughnening of the substrate. The results have shown that a micro-columnar structured Si film (with 3.6 μm thickness) sputtered on roughened Cu foil surface has been achieved to cycle without failure eventhough the capacity value is very low. The importance of the film thickness has been also highlighted in literature. It has been claimed that it is difficult to improve the energy density of the electrode by increasing the film thickness, because by increasing the film thickness diffusion length of Li as well as the tensile stress in the Si film generated during Li insertion increase [77]. The volumetric expansion in Si film occurred in cycling has been analyzed by ex-situ SEM [51, 54]. The results have proved that as the film is attached to the substrate with high adhesion, the expansion has occured perpendicular to the film surface normal. On the other hand, in delithiation contraction takes place both perpendicular and in plane directions versus the substrate surface normal. The latter causes cracking of the film after the first cycle to form “islands” that still remain attached to the substrate after delithiation [77]. These islands formation helps the active material to be cycled without additional cracking which avoids the quick failure of the electrode after first cycles (Fig. 2.6.).

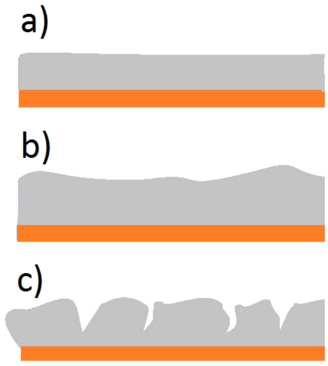


**Figure 2. 6 :** Schematic representation of the Si film a) as-deposited state, b) lithiated state, c) delithiated state.

It is important to prevent any possible disconnection of the film from the current collectors following the volumetric changes [69]. Because thin film structure can not decrease the stress induced by the size effect on the horizontal direction thus the material cracks/ pulverizes, hence might lose its contact with the current collector. Therefore, some additional element/compound can be used with Si to minimize the destructive effects of volume changes in cycling.

In 2013 Wen et al [78] have confirmed this fact and revealed another reason for the declining in the electrochemical performance of thick Si film : low electron conductivity of Si. Low electrical conductivity of Si increases the internal resistance of the battery. The time to measure the current would not be enough, resulting low capacity in cycling. Therefore, the use of additional element/compound in the Si film could be also beneficial to form new electron conductive pathways.

Other than those mentioned above, the crystalline structure of the Si (α-Si) is also important. To make more detailed analysis, Si thin films have been clasified depending on their crystal structure: amorphous and crystalline. In 2000, Li et al. have investigated [79] lithiation of α-Si film and they have found that a layer by layer destruction of the pristine Si film crystaline structure occurred since Li diffusion is very high in <110> direction. Thus, amorphous phase forms along the surface of <110> direction of the α-Si. On the other hand, for a-Si not only an isotropic expansion occurred but also the crystal transformation and thus the irreversible Li trapping are prevented, resulting in an increase of coulombic efficiency in cycling. In 2003, Maranchi et al [56] produced 250 nm thick a-Si film by magnetron sputtering on a Cu substrate. They have shown that at the Cu/Si interface, Li-Si-Cu intermetallics have been formed, plus plastic strain in Cu substrate has been increased in cycling leading a progressive decrease of capacity during the galvanostatic test. In the same year, Graetz et al. [72] have produced 100 nm thick a-Si thin film by physical vapor deposition (PVD) method. Then, in 2004 Ohara et al. have fabricated an a-Si thin film of 50 nm by PVD [80]. They have indicated that it would be better to have a mixture of amorphous and polycrystalline Si in the negative electrode since a-Si would act as a buffer in that case. In 2009, Cui and co-workers have fabricated crystalline-amorphous core-shell Si nanowires as anodes [81]. They have preferably chosen a-Si because Kumta and co-workers [57] have shown that a-Si is able to withstand better pulverization during cycling as compared to α-Si. Plus, Cui et al. [81] have also mentioned that α- and a-Si particles react with Li at different potentials: around 220 mV for α-Si and 120 mV for a-Si. Therefore, Cui et al. have used α-Si acting as a stable mechanical support for a-Si to provide an efficient electrical conducting pathway when the charging potential is limited to such a value (higher than 120 mV) that only a-Si would react with Li. These core-shell anodes have exhibited a high charge storage capacity (around 1000 mAh $g^{-1}$) with a 90% capacity retention over 100 cycles, but the rate capability of the electrode should be still improved due to the intrinsic low electrical conductivity of Si.

Indeed, different than powders, Si thin film has been shown different fracturing mechanism where cracking could be affected by both the bounding strength among the particles of the film and between the active material of the film with the substrate [82]. In this sense, in 2012, the fracture formation in a-Si film produced by magnetron sputtering method has been discussed [83]. In cycling, Si thin films have broken up into individual pieces (islands) that have been separated from each other as interconnected cracks. Then, for the thinner Si films, the size of the islands would be smaller. Microscobic analyses have proved that the islands are not connected with each other but most of them remain attached to the substrate in cycling since the substrate is thicker than the Si thin film. Plus, it has been also demonstrated that depending on the film thickness the shapes of cracks forming in the electrode have changed: cracks have been straight in thick films but wiggled in thin films. For the 1000 nm thick a-Si thin film “a growth of cracks” has been noted rather than crack nucleation. Because a branch of primary cracks (long and straight) propagated until reaching to another branch. Thus, there have been few sharp changes in direction. Other than that, all cracks have been long and straight in the thick film. This justifies that the number of crack initiation sites or the density of cracks (total length per unit area) in the final state is relatively small for the thick Si films. On the other hand, for thinner Si films, cracks showed more branches and wiggles. Although most cracks are interconnected with each other, there are many places where cracks are unable to propagate. Hence, there is more crack initiation sites and the density of cracks is higher in the thin Si films [77,83] (Fig. 2.7.).

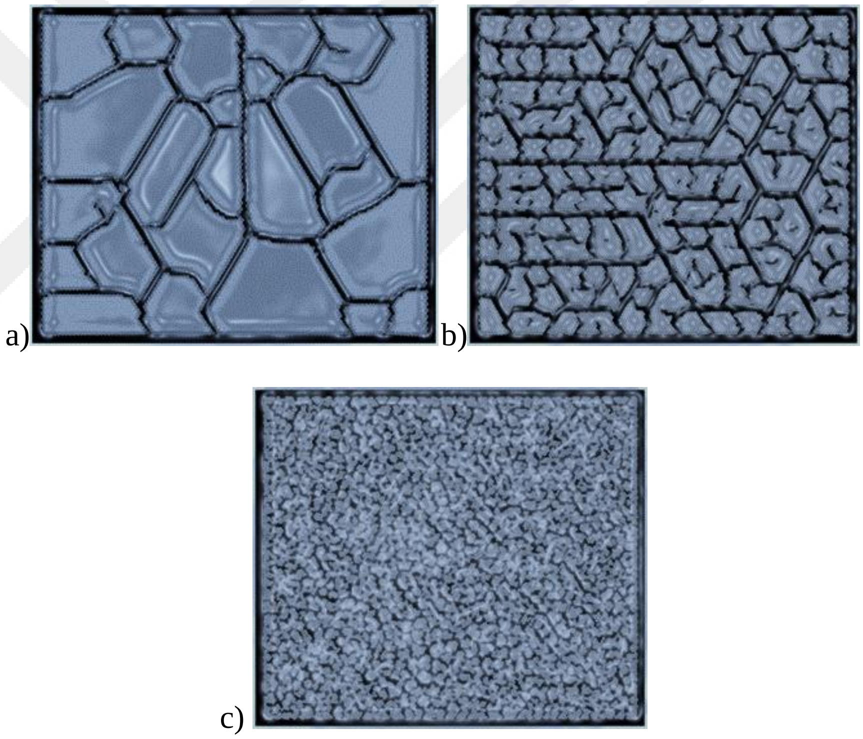

**Figure 2. 7 :** Schematic representation for crack formation in the Si films when a) thickess around 1000 nm, b) thickess around 500 nm, c) thickess around 200 nm [83].

Li have calculated the critical thickness of Si film for crack generation and estimated the order of magnitude of the critical thickness for cracking in a-Si film (non-porous) to be around 100-200 nm [83-84].

Considering these facts, to further improve both the rate capability and the energy density of the cell, nanostructured Si thin films should be used in next generation

LIBs, as reported by many bulk and micro-battery research groups [50, 85-87]. They have claimed that being able to accommodate high volume changes thanks to interspaces among the nanostructures, being directly connected to the metallic substrate leading a minimum capacity loss, having high surface area resulting higher reaction sites and having 1D structure to allow efficient electron charge transport and fast Li diffusion [81, 88] are the main advantages. As the nature of the stress experience by the active material is seen to be dependent on the morphology, the dimension and the structure of the electrode has a particular importance. Indeed, previously it has been showed that the stress level and maximum stress in the nano-structured materials is found to be lower than those of bulk materials because of their high surface/volume ratios. For instance, nanostructured Si films deposited on a substrate shows different volume changes since the stress dissipation in the electrode would be different depending on morphology, crystal structure and thicknes of the electrode. In this sense, the critical thickness for crack formation could be also higher than that of non-porous Si films. However, this idea is still underdiscussion.

*Three-Dimensional Structured Silicon Anodes:* Nanotubes having 3D have been used as anodes in LIB since both the interior and the exterior surfaces are accessible to Li. Therefore, nanotubes are expected to have enough free spaces to accommodate the large volume changes of Si, and to retain stable surface between the electrolyte/electrode for long cycles. In 2008, Kim et al. [89] and in 2010 Xiao et al. [90] have produced “octopus foot-like” and “nest-like” electrode, respectively. Eventhough these structures shorten Li diffusion path and increase the contact area of electrodes with electrolytes, they can only be produced by expensive and complicated methods. Plus, because of their low tap density, the volumetric energy density wouldnot satisfy next generation applications’ requirements [43].

### 2.2.2. The Effect of composition in Si anodes for LIBs

Using Si composite and/or alloy may be another solution to overcome the disadvantages of Si anode material.

In alloy design Obravac et. al [52] have mentioned that the specific energy (and the volumetric energy), the magnitude of the volume expansion and the ability of an electrode to withstand volume changes must be taken into account. Thus, it is important for anode materials to have additional space and/or some buffers along with active materials to accomodate volume expansion during lithiation. It has been experimented that beside co-deposition, the top coating of ductile metal particles like Fe, Co and Cu on Si can significantly improves the electrical contact and cyclability within charge and discharge.

Two types of lithiation reactions with alloys have been distinguished: Type I has the named as ‘addition type reaction’ [91] and Type II is the “displacement type reaction”.

In the Type I, nanocomposites of active (Si) and inactive (SiM) particles react with Li. Inactive (SiM) phase is merely a bystander during the lithiaton. Therefore, the voltage-capacity plateau of the Type I alloy is mostly unaffected by any inactive phases presence. However, this inactive phase may affect the kinetics of lithiation, because of different diffusion coefficients values of Li of active and inactive particles. In recent years, many scientists have produced composites where an active material is dispersed in an inactive matrix. The inactive component should be stable over the potential range that the active particles are operated. Besides, matrix materials are expected to be high electronic conductive and ductile to play a “buffer” role for alleviating the mechanical stress arising during lithiation reactions. Moreover, the inactive component is supposed to suppress the aggregation of the active element (Si) upon cycling. In this regards, the inactive matrix forms a skeleton (or a network) not only to accommodate the volume changes but also provide reaction sites for the active elements. On the other hand, for Type II, lithiation occurs for alloys in which active elements are weakly bounded to inactive phase [92]. Such displacement reaction can be written as decomposition and Type I lithiation reactions.

Herein, as the decomposition reaction needs a change in free energy (and in volume), for Type II it is important to have enough energy to realize the decomposition reaction. The amount of this free energy value can be obtained from tabulated values which are prepared by means of the macroscopic atom model [93]. As stated, the addition/dopping some conductive elements in Si is very advantageous because they could improve the conductivity of the film. Therefore, among all the alternative additives (such as Ag, Ni, Sn, Cu etc.) in this dissertation silver (Ag) and copper (Cu) have been chosen to be used with Si.

Ag having the highest electrical conductivity in all elements, reacts with Li under 0.2V (vs $Li^{+}$) (Fig. 2.8). Though Cu is an inactive element versus Li (Fig. 2.9), it is known to own the second highest electrical conductivity after Ag. But the cost is much cheaper than Ag. Moreover, the fact that the phase diagram of Ag-Si and Cu-Si elements demonstrates differenciations, the electrochemical performance of Si-M (M:Cu,Ag) electrodes are expected to be different from that of the pure Si anode (Fig. 2.10.a,b) [94].

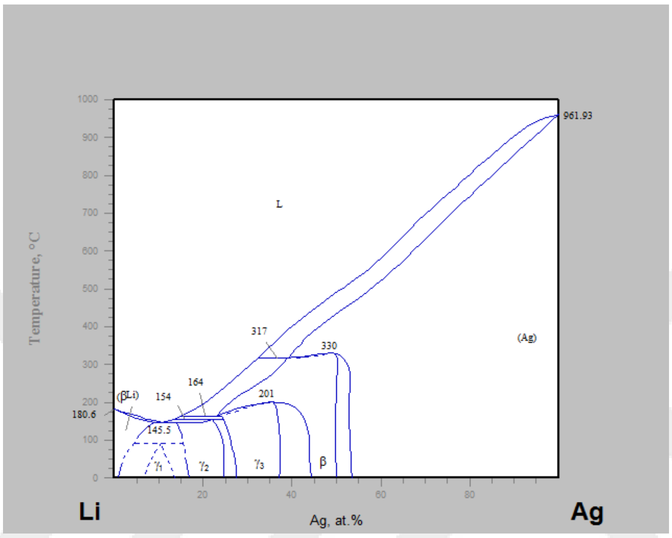


**Figure 2. 8 :** Phase diagram of Ag with Li [94].

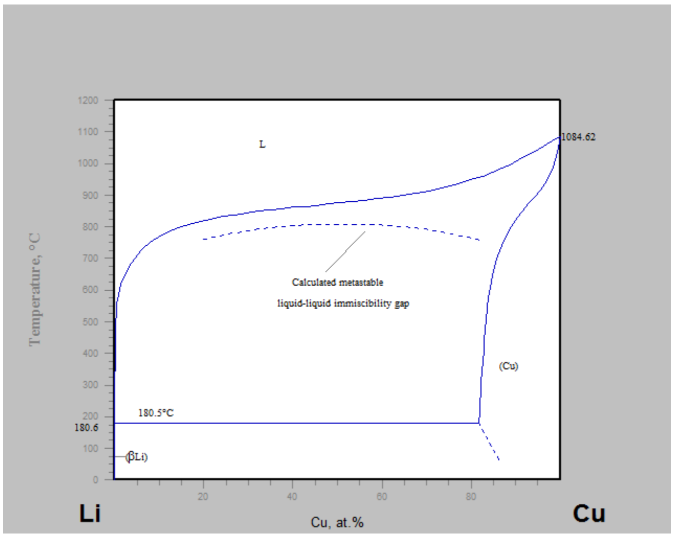


**Figure 2. 9 :** Phase diagram of Cu with Li [94].

a)

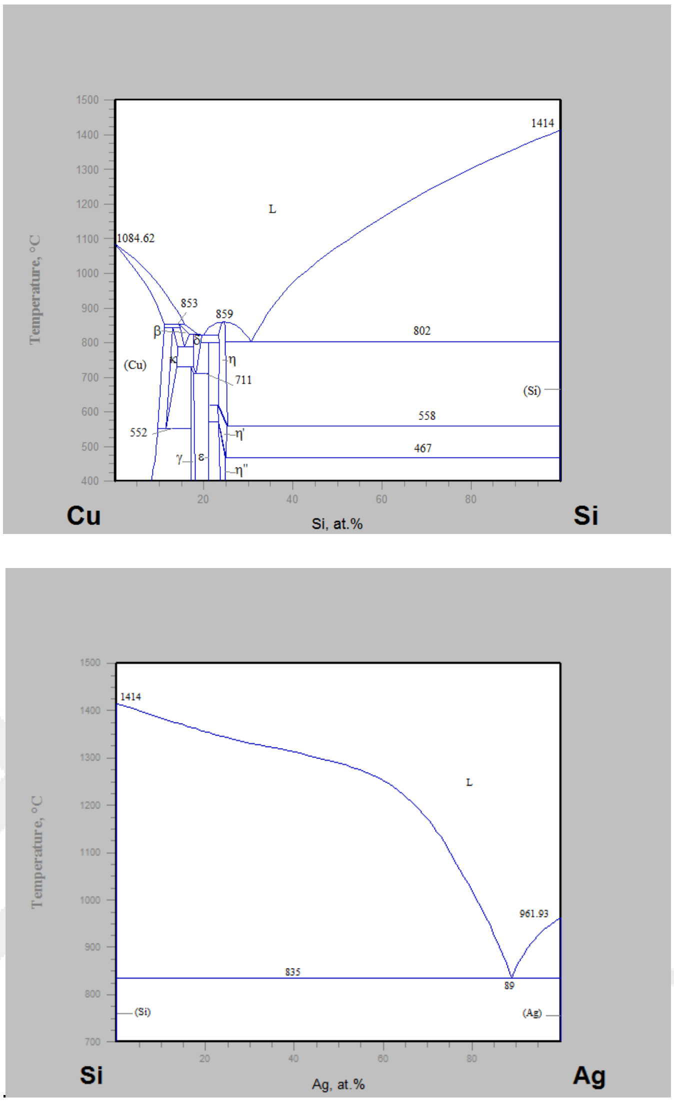


b)

**Figure 2. 10 :** a) Phase diagram of Cu with Si, b) Phase diagram of Ag with Si [94]. .

# 3. THIN FILM VACUUM DEPOSITION METHOD

Variety of vapor deposition techniques can be employed in order to produce thin films. Direct heating, evaporation via focused electron beam or laser or arc-induced, and sputtering (bombarding the material with energetic inert ions) are the basic principles of vapor deposition techniques [95]. Herein, it is important to note that all of these techniques are performed under vacuum and rely on the kinetic theory of gases (see Fig. 3.1.).

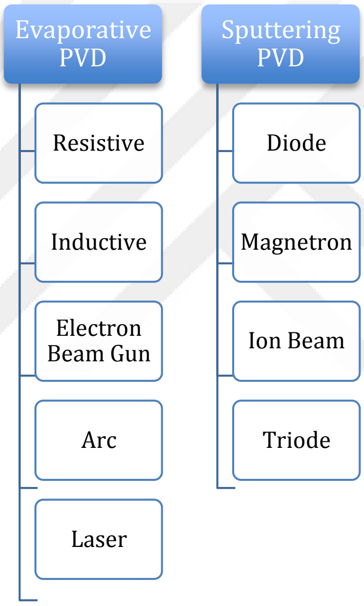


**Figure 3. 1 :** Vapor deposition methods [95].

## 3.1. Physical Vapor Deposition Method (PVD)

Physical vapor deposition process involves a physical method to remove individual atoms/molecules from a source (solid or liquuid), then transfer through a vacuumed chamber to deposit on a substrate surface to form a film [96]. PVD methods  enable one to fabricate thin films followed by the condensation of a vapor particles of the desired material onto substrate surfaces (Fig. 3.1.).

Unlike CVD process where chemical reactions trigger the deposition process, PVD is a purely physical process. This method dates back to 1838 and has been on progress since then. First application was done by Micheal Faraday who deposited films by evaporating material.

- PVD methods being environmentally benign process, enhances a product's durability (hardness, strength, abrasion resistance) and prolonges service lifetime of an unprotected product by improving the corrosion resistance. Plus, a wide range of diverse group of substrates (like any type of inorganic and/or some organic materials) might be used as substrates [96-98].
- In PVD methods it is possible to evaporate or sputter the target material to be deposited [96-98].

In this dissertation both electron beam evaporation and magnetron sputtering methods have been used to engineer Si based thin films to be used as anodes in rechargeable lithium ion batteries.

### 3.1.1. Electron beam evaporation method

The process uses a stream of high energy electrons 5-30 keV to evaporate the source materials. Mean free path (MFP:how far does an electron can go before striking to another) and impingement rate (IR:how many molecules strike the substrate surface in a given period of time) are two important concepts of the process. Indeed, it is known that contrary to the atmospheric conditions in vacuum environment MFP is very high and IR is very low.

The advantages and disadvantages of electron beam evaporation process are given in Table 3.1.

**Table 3. 1 :** Advantages and disadvantages of electron beam evaporation method [95,96,99,100].

| Advantages | Disadvantages |
|---|---|
| High deposition rates (1-10 nm $s^{-1}$) | Difficult to control the film composition |
| Less substrate surface damage from impinging atoms | Possible X-ray damage due to electron beam evaporation |
| Excellent purity of the film in very high vaccuum environment | Difficult step coverage (a line of sight process) |
| Minimum substrate heating due to cooling system | |

The equipment for electron beam deposition includes ultra high vacuum, vapor source, magnets to control the beam, cooling water system for crucible, quartz crystal microbalance to monitor the deposit thickness, bell jar (vacuum chamber), mechanical shutters to presicely control the evaporation rate and high electrical power (either high current or voltages, 1-10kW). Usually, the gun source is used in the system and the electrons are thermionically emitted from heated filaments. Electrons are directed to the crucible thank to the magnetic field created by the magnets. Contamination in the film is eliminated by the shields as the process is line of sight.

In evaporation, the filament cathode is polarized (biased negatively) with respect to a nearby grounded anode from 4 to 20 kV. This value is high enough to accelerate the emitted electrons. Then, a transverse magnetic field is applied to deflect the electron beam in a $270^0$ circular arc and focus it on the hearth of the crucible (Fig. 3.2.) [101, 102]. Prior to deposition, pre-cleaning of the substrate is necessary to form adherent coatings. Therefore, parts to be coated (substrate) are first cleaned by acetone before placing in the chamber. When the energy brought by the lectron beam increases the temperature of the source material to its evaporation temperature, atoms or molecules start to leave the surface of the source material in the crucible and travel following more or less straight pathways until they reach another surfaces (substrate, chamber wall, instrumentation). As the temperature of these surfaces are lower, these atoms or molecules will transfer their energies to the surface to be condensed. Herein the vapor pressure at the substrate surface is very high which restrict their re-evaporation.

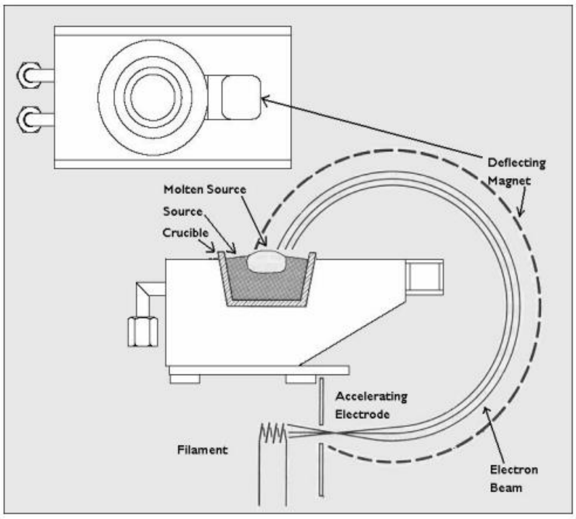


**Figure 3. 2 :** Schematic representation of electron beam evaporation method [101].

In electron beam evaporation process, multiple vapor sources could be used to get multilayered coatings or composite films made of  multiple components.

The physical principle of the evaporation process lies on the “vapor pressure” principle. “Vapor pressure” is the pressure at which the vapor phase is in equilibrium with its solid or liquid phase at a given temperature. Evaporation from the melted (liquid) phase or direct sublimation from the solid phase can be occrred depending on the vapor pressure of the evaporated material: if the element in question achieves a vapor pressure greater than $l0^{-3}$ torr (vapor pressure between $l0^{-2}$ and $l0^{-3}$ torr is required for high rate film growth) at its melting point, it sublimes.Therefore when a vapor pressure of a material is significantly higher than the pressure inside the vacuum chamber a flux of atoms is being emitted from the source material in all directions.  Elements such as Cr, Ti, Mo, Fe, and Si reach sufficiently high vapor pressures below their melting point [95]. However, in most cases materials in question do not have a vapor pressure higher than $10^{-3}$ torr at its melting point metals, thus a melt forms before it evaporates.

The vapor pressures of the pure element, compound and alloys are different: pure metals evaporate as atoms or clusters thus their evaporation rate depends on their vapor pressure. Alloys are made of two or more metals. The physical properties of an alloy is between the constituent alloying elements whereas the chemical properties of each element forming the alloy remain unaffected. Knowing that the constituents of an alloy can be separated by physical means (separated by melting), in evaporation the constituents of the alloys evaporate nearly independent from each other and enter the vapor phase as single atoms (in a manner parallel to the behavior of pure metals). However; the evaporation of compounds is found to be different than those of the pure elements or alloys. The difference is based on the principle differenciation in terms of “alloy” and “compound”. A compound is an association of several elements that are bound together through chemical reactions. Molecules (elements bound together by covalent bonds or ionic bonds) and complexes (elements bound together by coordination bonds) are some examples of different compounds. Therefore, individual elements of a compound can be obtained by breaking the compound via another chemical reaction(s). In real life, very few inorganic compounds evaporate without molecular change. Different vapor pressures of the elements forming the compound causes differentiation in the vapour composition (from that of the original solid or liquid source). As a consequence, the stoichiometry of the film to be deposited via electron beam deposition generally differs from that of the source.

Mass spectroscopic studies of the vapor have proved that both molecular association and dissociation mostly occur in the vacuum chamber. In Table 3.2 evaporation phenomena that occur in compounds are categorized briefly.

**Table 3. 2 :** Evaporation of Compounds (M: Metal, X: Non-metal).

| Reaction Type | Chemical Reaction | Examples | Comments |
|---|---|---|---|
| Evaporation without dissociation | $MX_{(s\ or\ l)} \rightarrow MX_{(g)}$ | $SiO$, $B_2O_3$, $GeO$, $SnO$, $AlN$, $CaF_2$, $MgF_2$ | Compound stoichiometry maintained in the film |
| Decomposition | $MX_{(s)} \rightarrow M_{(s)}+1/2\ X_{2(g)}$<br>$MX_{(s)} \rightarrow M_{(l)}+1/n\ X_{n(g)}$ | $Ag_2S$, $Ag_2Se$<br>III-V semiconductors | Separate sources are required |
| Evaporation with dissociation | Chalcogenides: (Po,S,Te,Se,O + electropositive element)<br>$MX_{(s)} \rightarrow M_{(g)}+1/2\ X_{2(g)}$ | CdS, CdSe, CdTe | Separate sources are required |
| Less tendency for unintential substrate heating since there is a cooling system | Oxides:<br>$MO_{2(s)} \rightarrow MO_{(g)}+1/2\ O_{2(g)}$ | $SiO_2$, $GeO_2$, $TiO_2$, $SnO_2$, $ZrO_2$, | Metal rich discolored deposits (reactive evaporation is preferred) |

Once the chamber contains evaporated molecules or atoms, they may be adsorbed and permenantly stuck where they land (very rare), adsorbed and permenantly stuck after diffusing on the surface until they find an appropriate high energy sites (by physisorption or chemisorption), adsorbed then desorbed after sometime, or immediately reflected off from the surface. Herein the substrate temperature is very important because at high substrate temperatures the impinging molecules would have a kinetic energy higher than that of the substrate surface, so the adsorption becomes easier.

Considering the basic pricinciples of electron beam evaporation methods, in the next chapters the oblique angle deposition and glancing angle deposition methods by electron beam evaporation will be explained in details.

Oblique Angle Deposition Method (OAD): Among many variables that influence the growth of the film (substrate temperature, substrate position, evaporation rate, etc.), the deposition angle (θ) between the direction of the incoming particle flux and the substrate normal plays a key role to define the film morphology. Figs. 3.3.a-c clearly shows that in contrast to the dense thin film deposition where the flux of particles that contributes to the growth of the film reaches the substrate normal, the concept of oblique angle deposition (OAD) is different.

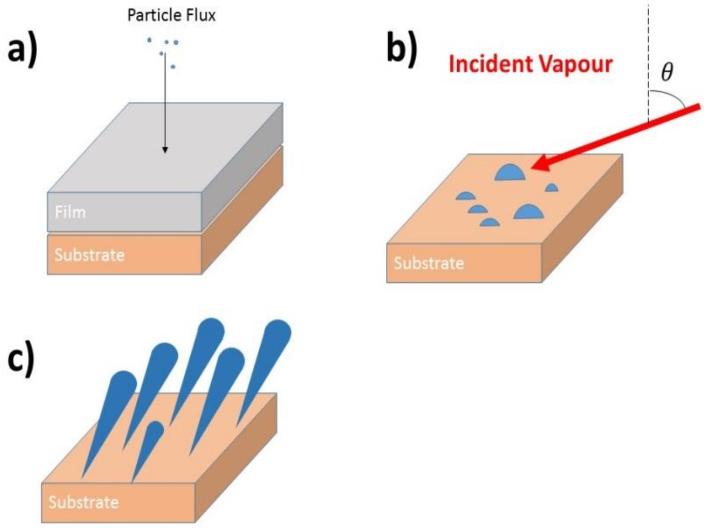


**Figure 3. 3 :** Comparison of thin film deposition resulting in a) dense layer (ϴ is zero), b) early growth of nanocolumns (ϴ>70$^0$), c) later stages of growth by OAD.

The mechanism of the nanorods formation during the OAD method has been studied previously. The results show that it is possible to control the orientation of the nanorods growth by changing the incident flux angle because the electron beam deposition is a line-of sight process. Therefore, to have nanorods in OAD method, the substrate position should be fixed to receive the evaporated particle flux under a highly oblique angle (ϴ) in reference to the substrate's surface normal (ϴ>70$^o$). The vapour flux ($\vec{F}$) hits the substrate from both vertical ($\vec{F_I}$=$\vec{F}$. cosϴ) and lateral ($\overrightarrow{F_{//}}$=$\vec{F}$. sinϴ) directions: the vertical component ($\vec{F_I}$) induces film growth and the lateral component ($\overrightarrow{F_{//}}$) contributes to the shadowing effect [101].

Karabacak et al. [102-103] highlight the importance of this "shadowing effect" and define it as one of the dominating mechanism that is competing with "surface diffusion process" to control the film morphology in OAD method. At room temperature deposition, since the surface diffusion rate is very slow, the impinging atoms randomly form islands on the substrate, when such growth is governed by Volmer-Weber or Stranski-Krastanov process (Figs. 3.4.a-b). As deposition proceeds, the initially nucleated islands act as shadowing centers and all large islands receive more impinging atoms as compared to small ones, leading to inclined nanocolumnar film growth, where homogeneously distributed porosities are formed among the inclined nanorods. Thereby, a decrease in the incident flux angle (ϴ) deteriorates the columnar growth, and generates a non-aligned (flat) film when the ϴ is $0^o$. Thus, to control the porosity or interspaces the incident flux angle (ϴ) should be close to $90^o$.

Besides the incident flux angle (ϴ), the substrate surface roughness and the evaporation source composition have significant impacts on the composition and the morphology of thin films, which in turn affect their electrochemical performances, when used as anodes in LIB [101-103].

For the OAD method since $\overrightarrow{F_{//}}$ remains constant during the deposition, columns with a tilt angle of β is formed. In most cases, β is less than the vapour incident angle ϴ and follows the empirical tangent rules ($\Theta < 60^0$) or cosine rule ($\Theta > 60^0$) (Fig. 3.6.) [104-106] (3.1, 3.2):

$$\tan \beta = \tfrac{1}{2} \tan \Theta \tag{3.1}$$

$$\beta = \Theta - \arcsin((1-\cos \Theta)/2) \tag{3.2}$$

a)

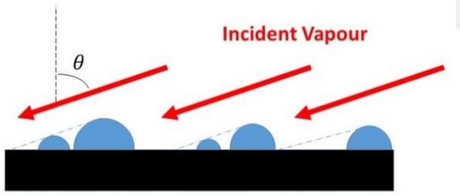


b)

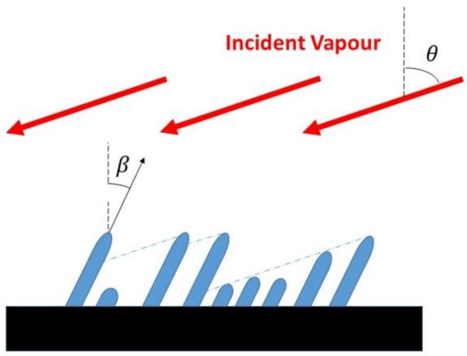


**Figure 3. 4 :** a) Nucleation, b) growth of inclined nanocolumnar structured thin film.

Both equations are not derived from basic physical principles, but rather found to be correlated well with experimental results [105,107-108].

The drawback of these models is purely geometrical since they neglect the surface mobility of the ad atoms, conservation of momentum of ad-atoms and residual gas pressure.

Therefore, Lichter and Chen incorporates the effects of surface diffusion and they derived the (3.3) where the Θ (Θ < $60^0$) is independent on the magnitude of the beam flux (J) and on the height of initial surface perturbation [109].

$$\tan \beta = 2/3\ [(\tan(\Theta)/ (1+\Theta\ \tan(\Theta).\ \mathrm{Sin}(\Theta)] \tag{3.3}$$

Briefly, as seen by the schematic representation (Fig. 3.5.) of the geometrical relations between incoming particle flux and islands formation on the substrate surface, the atomic-scale self-shadowing is very important for film formation process. The deposition of further particles is restricted to the tops of the nuclei that have formed primarily on the substrate. Therefore, rather than a compact thin film, sculptured thin films (STFs) comprising of columnar, needle-like structures, inclined in the direction of the incoming particle flux are evolved.

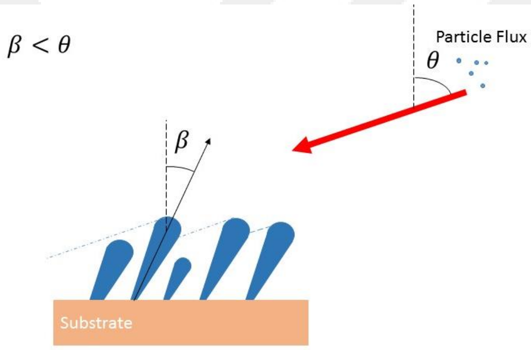


**Figure 3. 5 :** Schematic representation of the general rule $\beta$< Θ .

Glancing angle deposition (GLAD):

In 1959, Young and Kowal were the first to combine OAD with azimuthal substrate rotation under deposition angles $30^0$ < Θ < $60^0$ , to form a polarization filter for visible line on glass [110].

Although this particular experiment is very unique, the idea of altering the film morphology using both OAD and azimuthal rotation was not used again until the mid of 1990s. With the introduction of SEM analysis technique, Robbie et al started to work STFs [111-112]. They increased the Θ and rotated the substrate with stepwise rotation or continuous rotation (Fig. 3.6.) and they proved that increasing Θ> $80^0$ leads less dense film growth.

The basic deposition step is the same as that of OAD (Fig. 3.7a.). The deposition flux is incident onto a substrate at a large angle (Θ >$70^0$) with respect to the substrate normal. But in GLAD, the substrate is manipulated by two programmed stepper motors. One motor controls the incident angle and the other controls the azimuthal rotation of the substrate with respect to the surface normal. During the deposition the substrate can rotate azimuthally at a fixed incident angle, polarly changed incident angle or around both axes simultaneously [113-114].

Fig. 3.7. shows SEM views of the differently structured thin films fabricated by GLAD method, given in literature [115-124].

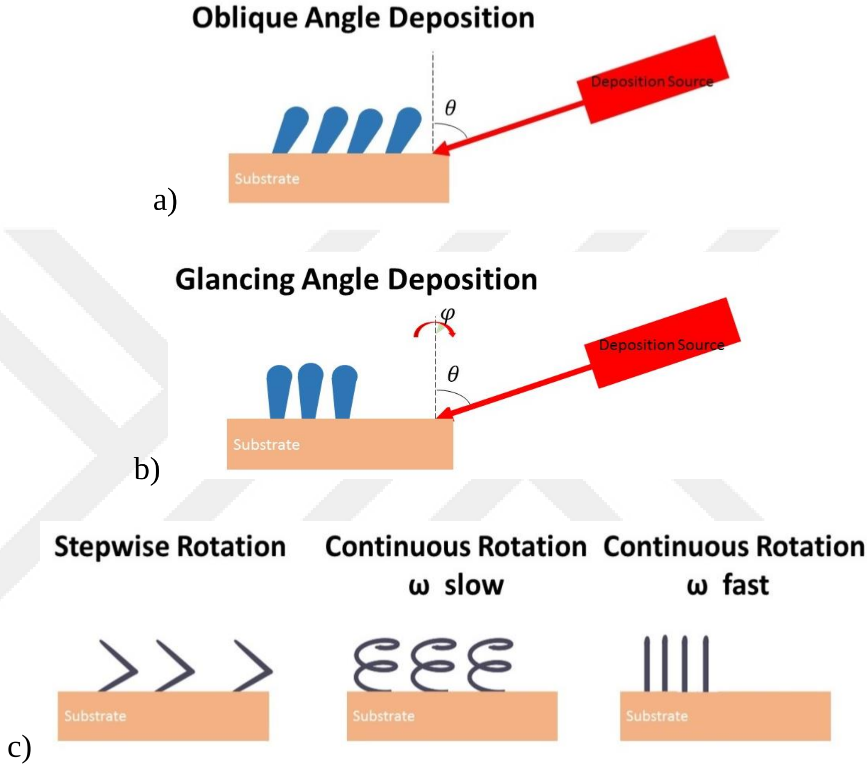


**Figure 3. 6 :** Comparison of a) OAD and b) GLAD method, c) n-fold structures with stepwise substrate rotation , helical (slow substrate rotation speed, w) or vertical columnar structure (fast substrate rotation,w) with continuous substrate rotation.

During the GLAD, the deposition rate not only has a vertical component (with respect to the substrate surface) but also has a lateral component. The lateral growth rate contributes to the shadowing effect, which brings about two facts: the self-alignment effect and lateral sculpturing effect. Thus, in GLAD the three parameters that determine the morphology of the columns are very crucial: the incident angle, the growth rate, the substrate rotation speed.

By changing the speed and the phase of the rotation and the evaporation deposition rates of sources the nanocolumns can be sculptured into a C shape, S shape, Zigzag shape or matchstick, helical and perpendicular columns (Fig. 3.8.) [125-126]. A stepwise rotation (with fast substrate rotation) for a predefined azimuthal angle, followed by a pausing cycle grows an 'arm' of the desired structure of the thin film (STF). In this period of pause, following the stepwise rotation, n-fold nanostructures (n being the number of pausing cycles in one full turn of the substrate), comprising of slanted column-like arms are grown. For example, two-fold chevron-like structures can be achieved by keeping the substrate motionless for a time $t_1$, then after rotation of the substrate it is kept motionless for another time $t_2$ where $\theta$ is stable around $70^0$ during all evaporation. On the other hand, when the substrate is continuously rotated with a fixed rotation speed (w) when $\Theta > 70^0$, depending on the pitch (p=r/w) value different morphologies from nanospirals (helical slow rotation, high p value), or crew like structures (intermediate p values) to non-slanted upright columnar 'matchsticks' structures (Low p value) could be achieved. A further degree of freedom can be introduced by changing the deposition angle in deposition to alter the density of STF along its thickness [126-127].

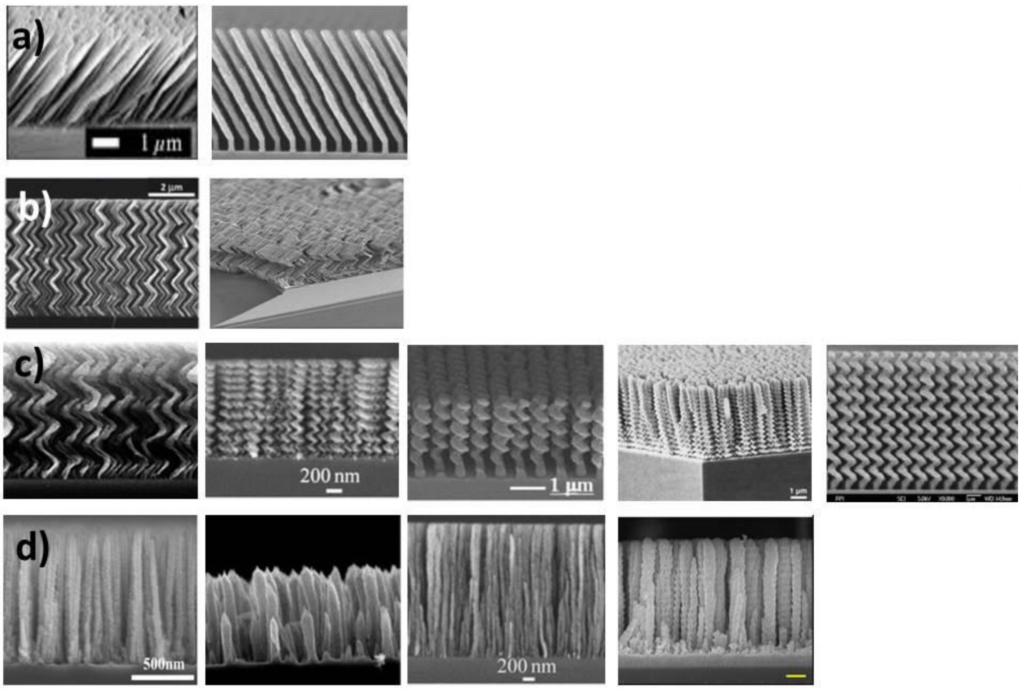


**Figure 3. 7 :** Different structures formed as a result of GLAD method. a) inclined nanocolumns, b) n-fold chevron like structure, c) helices, d) vertical nanocolumns.

### 3.1.2. Sputtering method

Among alternative PVD method, sputtering becomes remarkable since it is widely used in commercial applications due to some advantages [96,98]:

In sputtering, as there is no X-ray damage and the targets can be sputtered with DC or RF power a wide variety of metarials (metals, insulators, alloys and composites) can be sputtered. The target composition can be replicated during the film deposition. The substrate surface can be cleaned just prior to deposition to increase the adhesion of the coating. The step coverage and the film quality (adhesion, dense structure, etc) could be improved by adjusting the process parameters. Uniform thickness over large substrates can be achieved by using targets with high surface area.

However, during sputtering the substrate might be damaged due to ion bombardment. Possible contamination might be occurred unless using ultra clean gasses and ultra clean targets are used in the production. In some cases, a degradation occurs in some materials (e.g., organics) due to ionic bombardment. The process is considered to be energy ineffective.

In PVD, the existence of "plasma" is very crucial to produce well adherent coating on the substrate. Because plasma makes the gas conductive, thus the generated ions can be accelerated to strike the target. Therefore, before giving the principle of sputtering mechanism, the glow discharge and plasma concepts should be elaborated.

**Generation of Glow Discharge and Plasma:**

Plasma is the assembly of gas made of neutrals (atoms and molecules) and charged particles (ions and electrons). Plasma acting as electrical conductor, defined as "partially or fully ionized gas, which is on average electrically neutral and balanced". Because any change in the plasma would be balanced followed by the movement of the charged particles under the electric field effect. The concept of plasma is very important because it can be shaped in a chamber and moved by using electromagnetic forces [96].

Although for a physicist a glow discharge is not an ideal plasma, the term "plasma" was first used by Lewi Tonks and Irving Langmuir to describe the state of matter in the "glow discharge" (which is quite different than the ordinary gases) [128].

Sarkar explains that the plasma glows when the charged particles are deexcited by emitting photons. He states that to define "plasma" "degree of ionization" should be known: fraction of the neutral species (atoms and/or molecules) which would be ionized should be close to 1 to get "fully ionizde plasma". Knowing that electrons play a crucial role in plasma, electron density of the (cold) plasma in sputtering is between $10^{9}$-$10^{12}$ $cm^{-3}$ with 1-10 eV electron temperature.

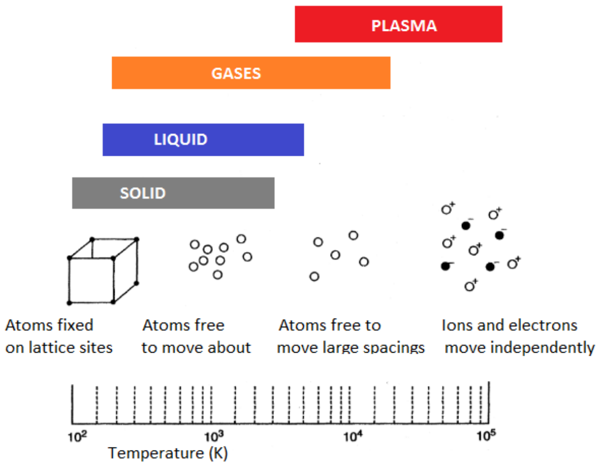


**Figure 3. 8 :** States of matter as a function of temperature [96].

In sputtering, the target, so called “cathode” is a plate of the materials to be deposited and it is connected to the negative terminal of a power supply. In the chamber, the substrate has three options: (1) it might not be connected to anywhere – floating. (2) it might be grounded, 3) it might have its own power supply so called BIAS where the negative pole goes to the substrate and the positive pole of this second power supply goes to chamber which is grounded [96].

In this low-pressure system, a DC glow discharge is created when a potential is applied between two electrodes. The formation of a glow discharge starts when a very small current flows initially as a result of small number of initial charge carriers (Fig. 3.2.). As the voltage increases, sufficient energy is imparted to the charged particles to create more carriers (like secondary electrons) as a result of their collisions with the cathode and neutral ions. When the positively charged ions collide with the cathode, their kinetic energy is partially transferred to the cathode. In addition, ions in the chamber also collide with neutral gas atoms (more often than the first case) transferring their energy partially to them. Whichever species strike the cathode redistribute the energy until a part of the cathode is ejected, typically in the form of free atoms (and electrons, X-ray (see Fig 3.3.)). This process is known as “sputtering” (Fig. 3.3). In a continuous system, as charge multiplication occurs, the current increases (Point A) rapidly but the voltage, which is limited by the output impedance of the power supply remains constant. This regime is known as the “Townsend avalanche” (Point B) where many electrons and ions are created through avalanches but the voltage is always constant. Eventually, when enough electrons are generated to produce sufficient ions, the discharge becomes self-sustaining (Point C).

Thus, the gas begins to glow now (Point D) and the voltage drops to few hundreds Volts accompanied by a sharp rise in current. At this state “normal glow” occurs (the region between Points C-E). Knowing that at early stages, the ion bombardment of the cathode is not uniform but is concentrated near on the defects (like the cathode edges or at other surface irregularities), at that period more power is supplied on the target, the bombardment increasingly spreads over the entire surface until a nearly uniform current density is achieved. A further increase in power results in higher voltage (and current density) levels. The “abnormal discharge” regime has now been formed and this is the operative domain for sputtering and other discharge processes (e.g., plasma etching of thin films) (the region between Points E-F). In Point G, an arc discharge is generated as a result of an electrical breakdown of a gas to form a current through a normally nonconductive media like “air”. The arc discharge that is formed as a result of the thermoionic emission of electrons from the electrodes has a lower voltage than a glow discharge [96]. Figure 3.3. defines the characteristic current-voltage curve during glow discharge sputtering process.

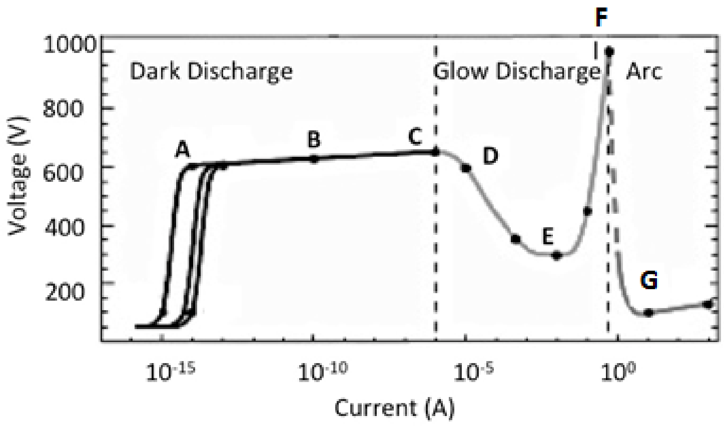


**Figure 3. 9 :** Glow Discharge formation in plasma A: Saturation current, B: Avalanche Townsend discharge, C: Self-sustained Townsend discharge, D: Corona discharge, E: Normal glow discharge, F: Unstable region, G: Electric arc discharge [96].

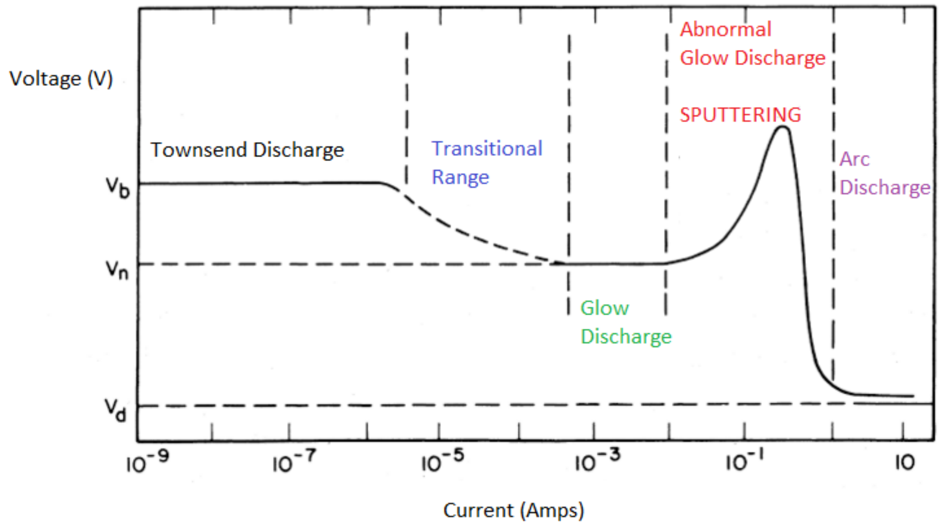


**Figure 3. 10 :** DC diode, current-voltage characteristic [96].

Therefore, within the plasma, collisions between electrons and other species (charged or neutral) dominate the properties of the glow discharge. Targets atoms are ejected following the collision of the working gas as a result of direct (of surface atoms) or cascade collisions (penetration into solid, which produces intermal collisions and recoils). These collisions might be elastic or inelastic depending on whether the internal energy of the colliding specie is preserved. Each collusion is different since it depends on the type of ion (mass, charge), the nature of surface atoms involved, and on the ion energy. Therefore, the type of the gas and the pressure level of the chamber are very important to form plasma prior to sputtering.

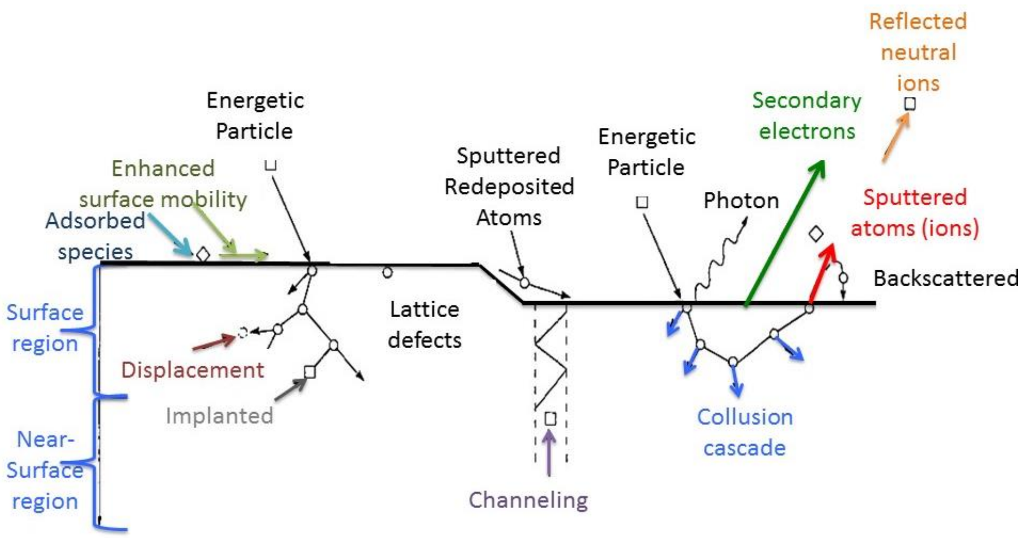


**Figure 3. 11 :** Depiction of energetic particle bombarded on surfaces and growing films [95].

In sputtering process, not only the target atoms, but also secondary electrons, X-rays and neutral atoms are also emitted from the target (Fig. 3.4.). The formation of these newly generated secondary electrons is very important for self-sustaining discharge reactions.] They are accelerated and ionize/excite an Ar atom and/or ionize an impurity atom like $O^-$ which goes to substrate and may go into the film. In deed sputter can be used for both etching and deposition. In this chapter main focus is on sputter deposition technique.

The sputtering process can be divided into four categories: (1) DC, (2) RF, (3) magnetron, (4) reactive. In all four processes the elemental and metal targets tend to have purities of 99.99% or higher, whereas those of the non-metals are generally less pure with a typical upper purity limit of 99.9%. These metallurgical realities rely on the drawbacks of the production methods (like powder metallurgy etc) used to produce electrodes. Targets are available in a variety of shapes (e.g., disks, toroids, plates, etc.) and sizes.

Followed by the definition of Sarkar, in DC sputtering, the glow discharge occurs because the electrons gain sufficient energy to generate visible light by collision, via photons. Fig. 3.4. gives shematic representation (with important regimes) of DC glow discharge process in a low pressure [96]: In its simplest form, the system consists of two electrodes in a chamber held at low pressure (1–10Torr). The chamber is typically filled with argon. A several hundreds volts is applied between the two electrodes. As explained previously a small population of atoms within the chamber is initially ionized through random collision processes, as a result the ions (which are positively charged) are driven towards the cathode and the electrons are driven towards the anode under the control of the electrical field present in the chamber. As long as the potential is maintained, a population of ions and electrons remains stable. During discharge process a layer of low luminosity appears on the cathode so named as “cathode dark space” or “Crookes fark space” or “space charge sheath”. Herein the voltage drops drastically, and the ions and the atoms are accelerated because very few collusions occurs in this region hence the absence of photons creates darkness. A bright region known as “negative glow” is noticed next to the dark region where the current increases but the voltage is limited by the power supply. Herein secondary electrons are created by Ar bombardment of the target material. This region is identified as “Townsend discharge” and it creates more electrons in the chamber. “Faraday dark space” and “positive column” follow the townsend discharge.

On the other hand, on the anode surface a very small glow region is present which is followed by an anode sheath (“positive column”) where electron is decelerated toward the anode due to its faster random movement. When electrode spacing is decreased postive column and Faraday dark space are consumed and glow discharge occurs with only cathode dark space and negative glow (“Argon plasma”) (see Fig. 3.4.). If the electrode spacing is reduced too much than the cathode dark space is distorted and discharge is extinguished. Therefore, to make effective sputtering the anode (substrate) should be placed well before the Faraday dark space (inside the negative glow) so that the positive column doesnot appear in sputtering.

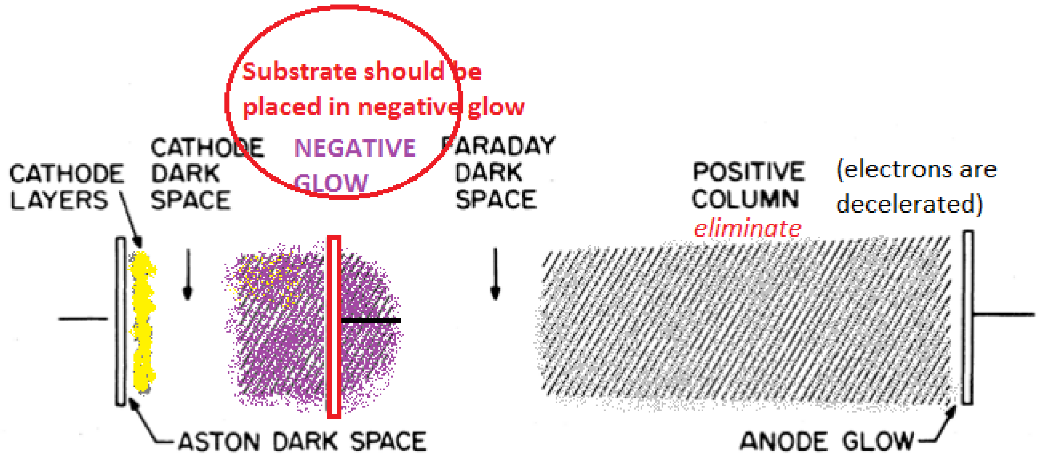


a)

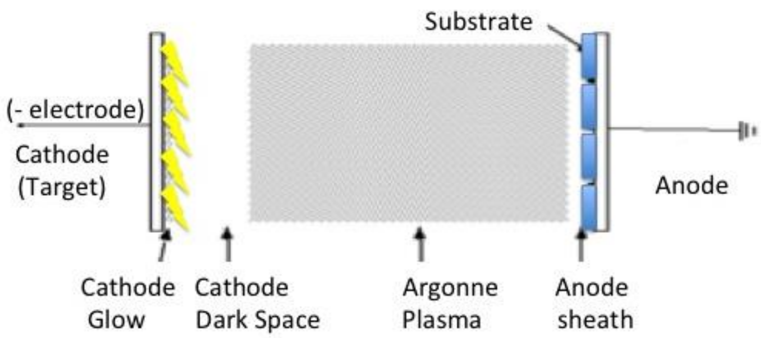


b)

**Figure 3. 12 :** a)Schematic representation of important regimes in a low pressure DC glow discharge b) Schematic representation of vacuum chamber for DC sputtering [95].

When the necessary calculations are done, the velocities of Ar and electron in a plasma are found to be (under 100 eV) 20000 m/sec and 6000000 m/sec, respectively. This shows that the plasma is highly conductive due to fast moving electrons.

As stated previously, presence of a continuos plasma is very important for coating. Experimental studies demonstrate that the multiplication of pressure with target-substrate distance should be larger than 0.5 (cm·Torr) to have a stable plasma (For instance, if target-substrate spacing is 10 cm, pressure should be higher than 50 mTorr). Because if the P×d value is too large, it causes too many collisions that prevent electron energy buildup. Otherwise if the P×d value is small, there will be very few collisions thus, very few secondary electrons are generated.

During sputtering, the energy of each incoming ion is measured to be 500-1000 eV, and the energy of sputtered particles (mostly neutral) of which energy distribution is given by Maxwellian distribution is 3-10 eV. Thus, the sputtering process is noted to be very inefficient from the energy point of view. Because 95% of incoming energy goes for heating the target and generating secondary electrons instead of sputtering new particles from target. Therefore, to realize high rate sputter deposition, an efficient cooling technique is highly required to avoid target damage from overheating.

It is important to note that, the sputtering efficiency is not always the same for every element present in the target. The "sputtering yield" (Y) should be well-known to describe the sputtering efficiencies of different elements present in the same target. Sputtering yield (Y) is the number of sputtered atoms per impinging ion. Between two different elements with different sputter yields, one with higher yield would have higher sputter deposition rate. The sputter yield depends on the energy of the incident ions, the masses of the ions and target atoms, the binding energy of atoms in the solid, and the incident angle of ions. On the other hand, the yield is rather insensitive to the target temperature except at very high temperatures where it shows an apparent rapid increase due to the accompanying thermal evaporation.

The maximum sputter yield is achieved when the incidence angle of impinging ions to substrate surface normal is about 60-70$^0$. At larger angles, surface electric field deflects the impinging ions and lowers the yield, and at lower angles the atoms are not sufficient (Fig. 3.6.).

The energy of incident ions is also crucial for sputter yield, as expected. A threshold energy exists for every material to release an atom from the target. Below the threshold energy value the atom is not “sputtered” (Fig. 3.7.). Therefore, once the ion energy is higher than the threshold, the yield increases with the energy. Once the incident ion energy is increased more and more, the yield approaches a saturation limit. Sometimes, at very high energies, the yield decreases because of the increasing penetration depth and hence increasing energy loss below the surface (Eq. 3.1, 3.2).

$$E_{Threshold} = \frac{Heat\ of\ Vaporization}{\gamma(1-\gamma)} \quad (3.1)$$

$$\text{where } \gamma = \frac{4\,M_1 M_2}{(M_1 + M_2)^2} \quad (3.2)$$

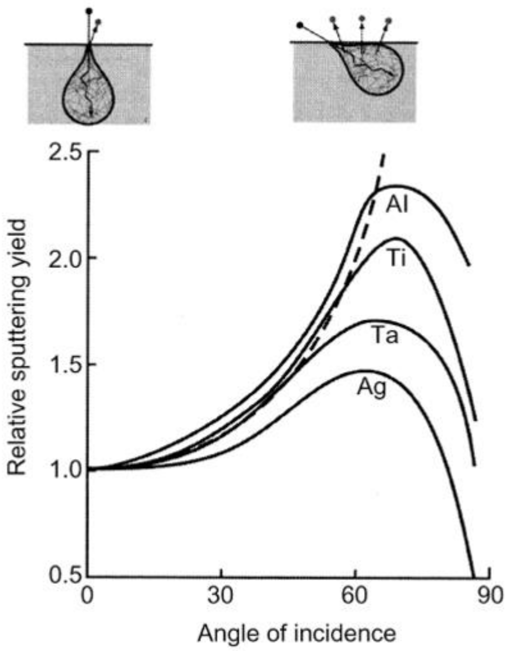


**Figure 3. 13 :** The incident angle effect on the sputtering yield of the element [96].

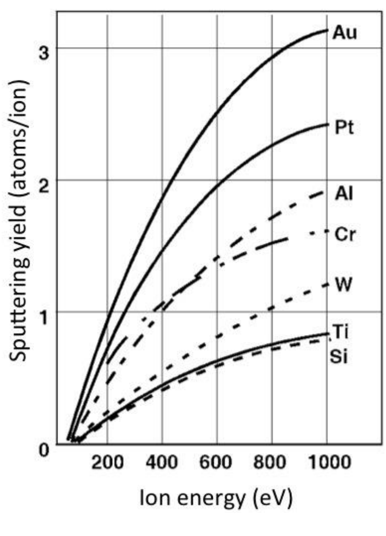


**Figure 3. 14 :** Sputtering yield dependence on the incoming ion energy [95].

Sputter yields of different atoms at different ion energy levels are given in Table 3.1.

**Table 3.1.** Sputter yields of different atoms at different ion energy levels [95].

| Target | 100 eV | 300 eV | 600 eV | 1000 eV | 2000 eV |
|---|---|---|---|---|---|
| Al | 0.11 | 0.65 | 1.2 | 1.9 | 2.0 |
| Au | 0.32 | 1.65 | 2.8 | 3.6 | 5.6 |
| Cu | 0.5 | 1.6 | 2.3 | 3.2 | 4.3 |
| Ni | 0.28 | 0.95 | 1.5 | 2.1 | |
| Pt | 0.2 | 0.75 | 1.6 | | |
| Si | 0.07 | 0.31 | 0.5 | 0.6 | 0.9 |
| Ta | 0.1 | 0.4 | 0.6 | 0.9 | |
| Ti | 0.08 | 0.33 | 0.41 | 0.7 | |
| W | 0.12 | 0.41 | 0.75 | | |

Moreover, ion incidence mass has to be high to increase the sputter yield. Fig. 3.8. shows that sputter yield is maximum for ions with full valence shells (such as Ar, Kr, Xe, etc ) [95,129]. Argon which is typically the choice of working gas rather than other heavy gases (radon, xenon, krypton) because it is easy to find argon and its price is affordable.

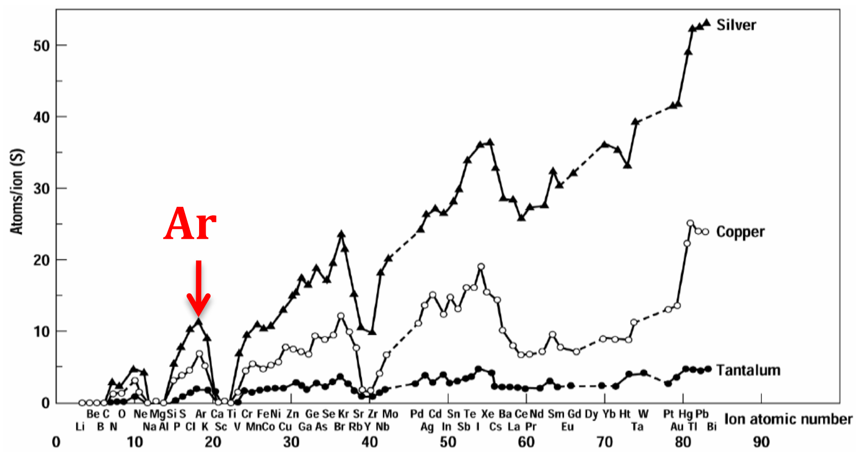


**Figure 3. 15 :** Incoming ion's mass dependence on the sputtering yield [95].

The deposition rate is also important for sputtering, hence pressure in the vacuum chamber should be optimized: at high pressure mean-free path of an atom is decreased, thus sputtered atoms have to go through tens of collisions before reaching the substrate and considerable amount of atoms would be deposited on the chamber wall. This reduces deposition rate. Whilst, at low pressure higher ion energy increases the sputter yield and deposition rate. But as there are very few Ar ions to bombard the target, the deposition rate is still considered as low. There exists an optimum pressure (provided that such a pressure can sustain the plasma) for maximum deposition rate. This optimum pressure depends on target-substrate configurations as stated previously (their separation, target/substrate size, etc.) (Fig. 3.9) [95,129].

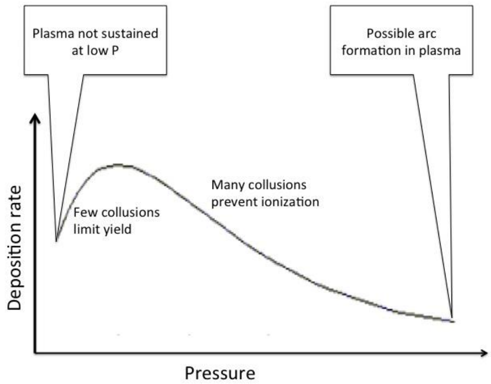


**Figure 3. 16 :** Deposition rate dependence on the pressure inside the chamber [95].

**Magnetron sputtering**

As in other PVD techniques, in magnetron sputtering, there is no chemical reaction that occurs behind the deposition process. Herein, it is essential to obtain a stable, bulk form of the material to be deposited ("the target") under vacuum atmosphere. During the deposition, once the substrate surface is cleaned then Ar plasma glow discharge is created in the vacuum chamber. This plasma forms the flux of source Ar ions to bombard the surface of the target.

It is possible to do both non-reactive and reactive sputtering depending on the conditions in the vacuum chamber. In the case of non-reactive sputtering, Ar is the gas chosen for the plasma, then for reactive sputtering, a reactive gas for the sputtered material such as $N_2$ and $O_2$ gases may be added/used in certain proportions to Ar sputtering gas to deposit nitride and oxide films, respectively [129,130].

The sputtering process consists of two electrodes: the positive anode (more commonly the grounded chamber) and the negative cathode (the target material) are positioned in a vacuum chamber. Once the ionization voltage for Ar is applied between the two electrodes, the electric field becomes strong enough to ionize the Ar gas in the chamber to form a stable plasma. The $Ar^+$ being positively charged accelerates towards the cathode (target) and bombards the surface to eject atoms from the target. In that case, the $Ar^+$ neutralizes itself with electrons from the target (“plasma current”). The voltage used in the sputtering determines the kinetic energy of the bombarding $Ar^+$ and thereby the energy of the ejected atoms. As stated previously, the ejection of atoms from the target also results in the emission of secondary electrons (from the target) to ionize more Ar atoms. As the latter promotes the plasma presence in the vacuum chamber, it is very essential to trap secondary electrons close to the target area as possible. The latter generation of more $Ar^+$ near the target where they are required. This is the main reason why a magnetic field is applied in the coating system.

This permanent magnet that is added to the sputtering target assembly enhances the deposition rate and traps the electrons near the target surface. This magnet creates lines of magnetic flux that are perpendicular to the electric field or parallel to the target surface. This static magnetic field retains secondary electrons in that region, which increase the number of collisions (Fig. 3.10.).

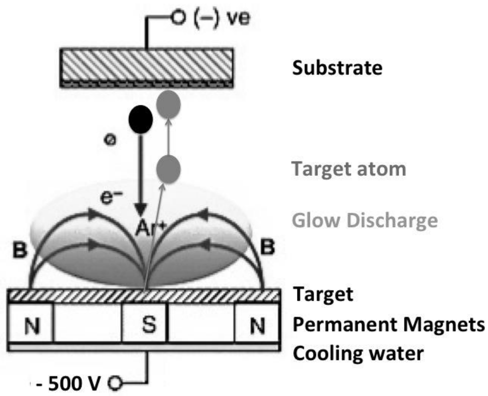


**Figure 3. 17 :** Schematic view of magnetron sputtering process [95].

Therefore, by means of magnetron sputtering the efficiency of ionization from energetic collisions between the electrons and gas atoms is improved compared to conventional DC sputtering. Thus, the current density and the deposition rates increase drastically (Fig. 3.11). In addition, unintentional target heating is reduced since the dense plasma is confined near the target and ion loss is less. Besides, discharge pressure decreases remarkably, a lower Ar pressure (to 0.5mTorr, can still sustain plasma) can be utilized since ionization efficiency is larger which can improve film quality as less Ar will be incorporated into the film.

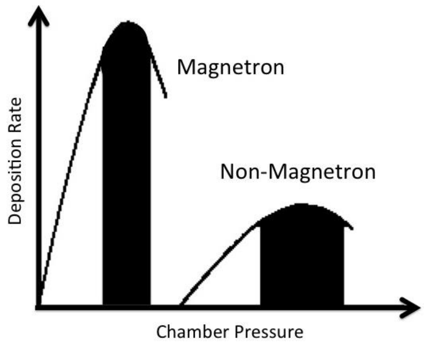


**Figure 3. 18 :** Comparison of deposition rate and chamber with and withour magnetron sputtering [95].

**High power pulsed magnetronsputtering (HPPMS)**

In a conventional magnetron sputtering process the plasma can be intensified by increasing the voltage, and eventually power. However, the operator is limited since overheating of target should be strictly prevented. Herein sputtering of insulating or low conductivity materials becomes very challenging because of the possible arc formation during the sputtering. The arcs could have detrimental effects to the structure as well as the properties of the film. To circomvent arcing, high power pulsed magnetron sputtering process is proposed in recent studies [131].

HPPMS was first developed by Kouznetsov et al [132] where they have applied high energy pulses in the megawatt range to the target to form a high density plasma in front of the target.

Indeed, pulsed magnetron sputtering is mainly designed to fabricate highly insulating films (particulary oxides and alumina) as the low deposition rate of RF sputtering and “target posining” causing arc formation of reactive sputtering process impede their practical fabrication. HPPMS process enables one to deposit defect-free films with a high rate (minimum arcing). Although AC power supplies are becoming available, in most cases pulsed DC power supply is used. Use of energy switching power supplies generates high frequency square wave signal. Therefore, during the deposition the target is being sputtered with the normal operating voltages for a fixed time (pulse-on). This duration is optimized to prevent charging on the poisoned region on the target surface. Then by changing the target voltage (pulse-off) the charge on the target is dissipated through the plasma. The voltage applied to the target during the pulse-off time could be more positive voltage or null. Kelly et al [131] claims as the electrons move faster than ions, preserving 10%-20% of the negtive operating voltage of the target is enough to dissipate the charged region and prevent arcing.

Besides, some power supplies equipped with advanced arc suppression electronic controls. In that case the total power applied to the target during pulse-on period would be restricted as well, resulting an arc suppression effect.

Pulsing frequency and reverse time are also important. Below 20 kHz HPPMS was not found to be effective to suppress arcing. And the reverse time should be optimized so as to get the duty cycle close to 50%:pulse-on time approaches or equals to pulse-off time. Studies show that reverse voltage hasnot found to minimze the arc formation, but affects the deposition rate [131].

HPPMS enhances the ionization of gas atom and increases the degree of ionization resulting well adherent, dense, defect-free, smooth film formation at high deposition rates [133].

Knowing that the microstructure of the film is determined as a result of the surface and bulk diffusion processes, the deposition temperature and the concentration of the impurities (inhibiting the crystal growth) become important to control the film morphology. In 1970, Thornton defined the relation of the thin film morphology with the deposition temperature where he claimed that low Ts/Tm ratio (Ts: substrate temperature, Tm: Melting temperature) gives columnar morphology and the high ratio predicts dense film formation. Nevertheless, Sarakinos et al [133] have declared that although the predictions of Thornton are valid for films deposited by magnetron sputtering, they are failed for films formed by HPPMS, because HPPMS results in film densification, surface smoothening and suppresion of columnar morphology or renuclation of columns during deposition. The latter promotes nanocrystaline or amorphous morphology of the film. Sarakinos et al [133-134] have also asserted that one would be able to better control the internal stress and their effect on phase formation by using HPPMS process

# 4. RESULTS AND DISCUSSIONS

## 4.1. SiAg Film by Magnetron Sputtering for High Reversible Lithium ion Storage Anodes [1]

### 4.1.1. Introduction

Lithium ion batteries (LIB) have been widely used in portable electronic devices (such as laptops, mobil[1]e phones, medical microelectronic devices etc.) due to their high energy density and long cycle life. However, further increase in energy and power densities with improved safety and low cost is highly required to get broad and practical applications in stationary energy storage devices and electrical vehicles.

So far, cathodes can deliver upto 300 mAh $g^{-1}$ capacity [135]. The overall cell capacity mostly depends on the anode material's capacity. Therefore, a need to replace the currently available commercially negative electrode, graphite, is on demand to get higher cell capacity.

Among alternatives (such as Sn, Sb, Al, Ge, Si etc. [136-139]) Si becomes remarkable. Because, it is environmentally friendly and abundant in the earth's crust. Moreover, it has a theoretical capacity of 3579 mAh $g^{-1}$ (at room temperature) which is more than 10 times higher compared to that of the commercial graphite [140]. The huge volume variation during lithiation and delithiation process (>300%) and unstable surface electrolyte interphase (SEI) film which causes low cycling efficiency and quick failure are the main challenges for the practical implementation of Si anodes in commercial lithium ion batteries [141]. In addition, its low electrical conductivity ($10^{-3}$ S $cm^{-1}$) and low Li diffusion coefficient (between $10^{-14}$ and $10^{-13}$

[1] This chapter is based on the paper : Polat, B.D., Eryilmaz, O.L., Keles, O. (2016). SiAg film by magnetron sputtering for high reversible lithium ion storage anodes. *Journal of Alloys and Compounds*, **654** 363-370.

$cm^2\ s^{-1}$) restrict the utilization of its full capacity and hinder its rate performance [142-144].

In the past decade, numerous scientific investigations have been directed to overcome the disadvantages. Using Si-M electrode is one of the solutions. Herein, M is not only used to prevent mechanical disintegration or the aggregation of Si in cycling but also works as conductive filler, which constructs conductive percolation network in the electrode. This is essential to compensate the low electronic conductivity of Si and achieve full electrode utilization. Besides, this conductive network can also increase battery power and enable faster charge/discharge reactions.

In this work, among various metals (M: Cr, Cu, Mo, Ti, V, Ni, etc.) Ag is particularly chosen [145-148]. In previous studies it has been shown that although both Si and Ag atoms are active toward Li. Knowing that Ag content affects the electrochemical reaction mechanism of the electrode, the optimization of Ag content in the film leads to benefit some advantages of Ag particles in the electrode such as buffering the large volume change of Si during cycling, creating new electron pathway in the electrode, increasing the overall cell potential related to its low lithiation potential (below 0.2 versus $Li/Li^+$) and minimizing the aggregation of Si particles in cycling [149-153].

Within the concept of this paper, we have decided to fabricate 3 micron thick SiAg (20% at. Ag) film by magnetron sputtering technique. The electrochemical performance of the SiAg film is examined when cycled in different potentials. The galvanostatic test results of the SiAg (20% at. Ag) samples cycled between 1.2–0.2 and 1.2–0.005 V are discussed based on the electrochemical reaction mechanism of the electrode with Li. The data provide a further understanding of the factors controlling the reversibility and the cycle life of the SiAg negative electrode. The outcomes show that deciding 0.2 V as the lower cut-off voltage is the best strategy. Because choosing 0.2 V as the lower cutoff voltage restricts the lithiation of Ag particles with Li. This prevents extreme volumetric change, the tendency of phase separation during Li removal and at the end the quick failure of the electrode.

### 4.1.2. Experiments

SiAg film is produced by using a Cemecon CC800/9 magnetron-sputter system. High purity (99.99%) Si and Ag targets ($500 \times 88$ mm$^2$) are used.

The substrates rotate on a planetary holder system to increase the interaction of the Ag and Si atoms along the SiAg composite film. Prior to deposition, the substrates are cleaned with acetone and isopropyl alcohol before being placed in the coating chamber. The chamber is pumped down to a pressure less than $10^{-5}$ Pa. To enhance the adhesion of the film, Ar etching is applied to the substrate at 550 V bipolar pulsed with 250 kHz frequency and 1600 ns reverse time. After cleaning, 150 W and 3000 W are applied to Ag and Si targets for 150 min at −100 V bias for the deposition.

The film is deposited on different substrates: Si wafers for cross sectional view, and mechanically polished (1200, 800, 600, 320, 3 μm, 1 μm, 0.5 μm) Cu discs (15.5-mm diameter and 1.5-mm thickness) for compositional, structural (XRD analysis) and electrochemical analyses.

The surface morphology of the film before and after the cycle tests as well as the film thicknesses are investigated by field-emission scanning electron microscopy (FEG-SEM, JEOL JSM 7000F). The distribution of Ag and Si atoms in the coating are displayed by means of backscattered imaging. The phases present in the coatings are determined using Philips PW3710 System with a 2θ range of 10–100° in steps of 0.05°(with CuKα at 40 kV and 30 mA).

Electrochemical performance of the SiAg electrode is measured using a 2032 button coin cells. The cells are prepared in an argon filled glove box (MBRAUN, Labmaster) based on the following sequence: i) a working electrode; ii) a 1M $LiPF_6$ in the ethylene carbonate-dimethyl carbonate, EC:DMC 1:1 (Merck Battery Grade) electrolyte solution iii) a separator (Celgrad 2400) and iv) a lithium metal foil as the counter electrode. The galvanostatic tests are made at room temperature in between 0.2–1.2 V (vs $Li/Li^+$) with C/12 rate. To understand the effect of cut-off voltage, another galvanostatic test is applied with the same rate (C/12) between 0.005–1.2 V (vs $Li/Li^{+)}$.

The changes in surface morphologies of the electrodes are examined to see the effect of potential range. The cycled samples are disassembled in the glove box and washed with DMC (dimethyl carbonate) and naturally dried in the glove box prior to the surface analyses.

HS-3E test cell (HohsenCorp., Japan) which enables to make measurement in three electrode configuration is used to accomplish cyclic voltammetry (CV) and electrochemical impedance spectroscopy (EIS). Herein, the SiAg films are used as working electrodes and Li as counter and reference electrodes. To justify the accuracy of the measurement in three electrodes cell, we measure the impedance of the working electrode (WE) and the counter electrode (CE) versus the reference electrode (RE) separately. Then, the sum of these impedances (WE/RE and CE/RE) is compared to the impedance results of WE versus CE (WE/CE). The results prove that using this geometry, the difference in the impedances of WE/RE and CE/RE is found to be less than 9% in the explored frequency range (not given here), which proves the EIS data used in this study are reliable and consistent.

Cyclic voltammetry (CV) is performed for the first 3 cycles in the potential range of 0.2 V–1.2 V (vs $Li/Li^+$) at a scan rate 0.03 mV $s^{-1}$ and electrochemical impedance spectroscopy (EIS) analyses are made on the 1$^{st}$, 2$^{nd}$ and 3$^{rd}$ discharged samples at 0.2 V, in the frequency range of 10 mHz-10 kHz with 10 mV rms (Gamry PCI4/750). To realize the EIS tests at 0.2 V, the cell is discharged to 0.2 V, then a certain amount of time is given for relaxation at the open circuit voltage (OCV) until the OCV potential drift is less than 0.5 mV $h^{-1}$, then the impedance of the sample is measured.

Finally, as the high-rate cycling behavior is one of the most important electrochemical characteristics of a lithium ion battery required for power storage application, the rate-capability of the SiAg film is evaluated by applying series of galvanostatic tests with different rates. The rate capability of the electrode is measured charging with C/12 rate and discharging at different rates (C/6, C/2, C and 2C). Both charging and discharging are conducted between 1.2 and 0.2 V vs $Li^+$. Since the discharge capacities at higher rates are lower than the charge capacity, 60 min open-circuit-potential relaxation is performed before the subsequent discharge reaction, as suggested by Sethuraman et al. [154]. This enables that the electrode retains its low state-of-charge before the beginning of each rate experiment.

### 4.1.3. Results and discussions

The backscatter view (Fig. 4.1.a–c) exhibits a uniform distribution of Ag particles that provides efficient electron percolation pathways from the current collector to the whole electrode. The surface view of the SiAg film displays a homogenous morphology (Fig. 4.1.d–f) where a grainy structure is remarkably detected. EDS analysis reveals the presence of 19.5% at. Ag in the electrode (along with less than 5%at. oxygen) The cross sectional image shows that the film has a thickness around 3.2 μm.

Comply with the outcomes of Lee [150] and Hatchard [149] et al.'s works the high amount of Ag (>15%at.) is thermodynamically immiscible with Si leading a phase-segregated morphology in the electrode (Fig. 4.1.a–f).

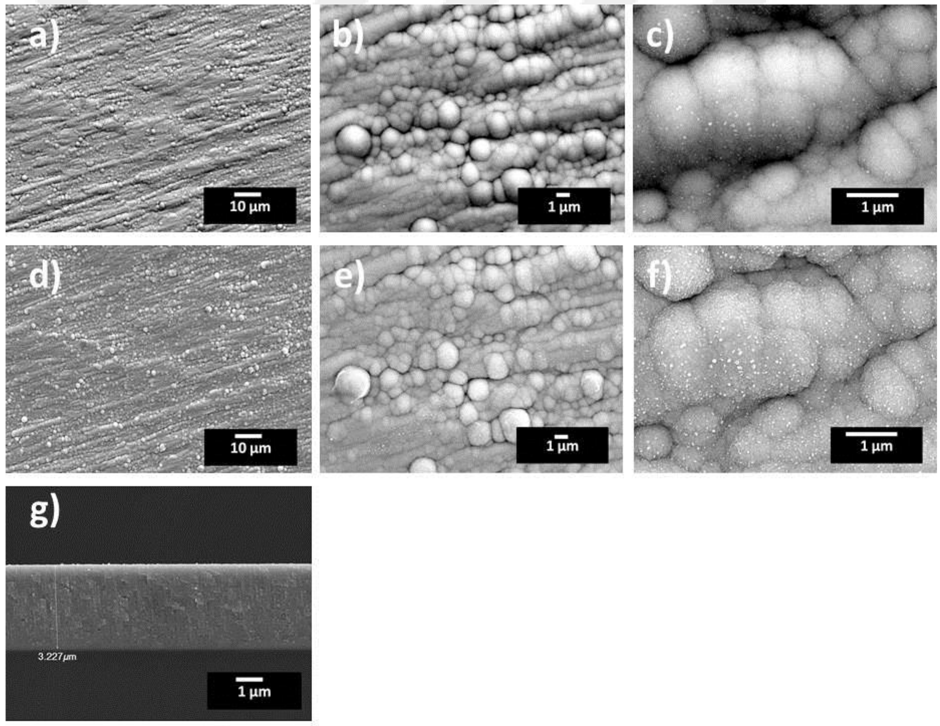


**Figure 4. 1 :** a), b), c) Backscattering images, d), e), f) SEM image and g) Cross section image of the SiAg film.

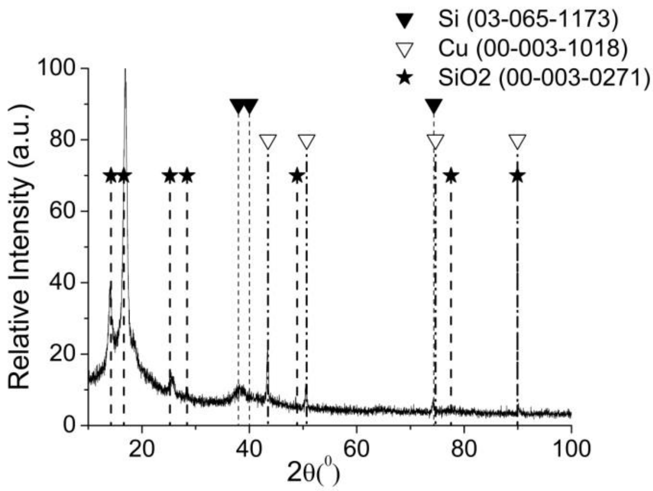


**Figure 4. 2 :** XRD analysis result of the SiAg film deposited on glass substrate.

The structural properties of the film are further investigated by means of XRD (Fig. 4.2), where the presences of Si (JCPDS:03-065-1173), Cu (JCPDS:00-003-1018) and $SiO_2$ (JCPDS:00-003-0271) crystals are clearly seen. $SiO_2$ crystals might be explained by the surface oxidation of the sample when it was taken out of the vacuum chamber to ambient atmosphere. And the peaks related of Cu are coming from the substrate material as the film contains only Si and Ag atoms. As no Ag peaks are seen in XRD spectra, Ag or Ag containing particles are believed to be present as in nano-sized crystals or amorphous structure.

The existence of the hump seen in low diffraction angles ($2\theta < 20^0$) gives the evidence of amorphous and/or nano-sized crystals in the film. It is believed that the electrode contains mostly amorphous Si beside some nano-sized Si crystals. When Si is sputtered onto Cu substrate, the atoms deposit with a random orientation and possess short-range order, as stated previously [149]. Herein, the presence of amorphous and nano-sized crystal Si particles is very important for the electrochemical performance. In previous studies, $Li^+$ insertion/extraction mechanisms in Si crystals are analyzed by using in-situ XRD, SEM and high resolution transmission electron microscopy methods (HR-TEM) [155-158]. In these researches, according to the "solid-state amorphization theory" during $Li^+$ insertion, the crystal structure of the nano-sized Si particle is destroyed and converted into an amorphous metastable structure (Li–Si) without the formation of intermediate phases [151-154]. This amorphous lithiated Si phase prevails up to 0.05 V, followed by the formation of a new crystalline ($Li_{15}Si_4$) compound when the cell potential goes down to lower values (V < 0.03 V) [54]. Furthermore, studies point out that during $Li^+$ extraction (on the anodic side), crystalline $Li_{15}Si_4$ is converted into two different phases (a-Si and α-Si), where $Li^+$ ions are trapped resulting a decrease in the specific capacity delivered by the thin film electrode. Therefore, to eliminate irreversible lithiation reactions of crystalline Si and to minimize the volume expansion in the electrode the lower cut off potential of the galvanostatic test is fixed to 0.2 V, which is higher than the recrystallization voltage of the lithiated product (0.03 V). In addition, knowing that the lithiation of Ag particles occurs below 0.2 V, choosing 0.2 V as a cut off voltage prevents the lithiation of Ag particles [54]. In this case, the Ag particles having no reaction with $Li^+$ are expected to be dispersed in the $Li_xSi$ matrix to promote the electrical conductivity, decrease polarization and minimize the aggregation of Si particles during cycling.

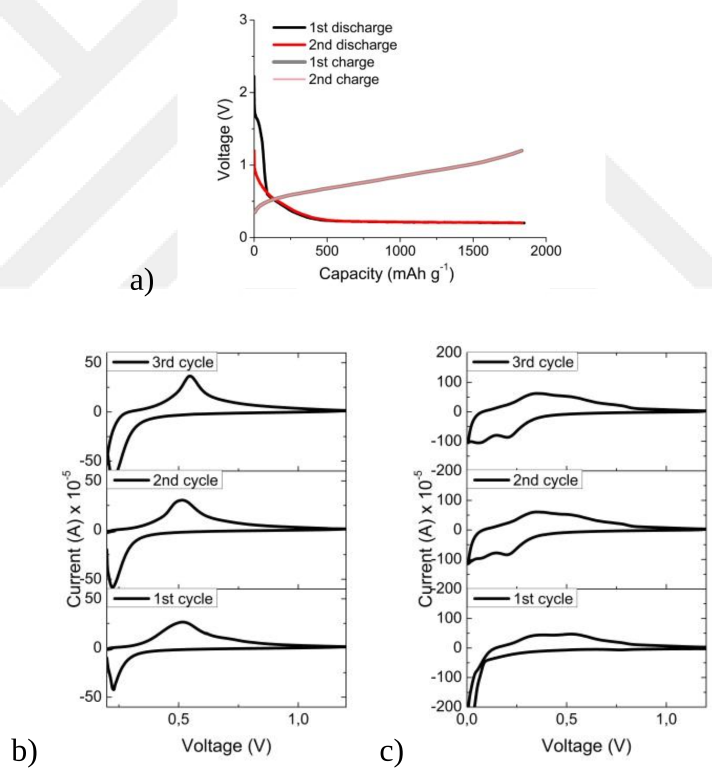


**Figure 4. 3 :** a) Capacity-voltage curvature of the SiAg film when cycled between 0.2-1.2 V; b) CV test result of SiAg film when cycled between 0.2-1.2 V, c) CV test result of SiAg film when cycled between 0.005-1.2 V.

To justify our hypothesis capacity-voltage curvature of the AgSi film for the 1st and 2nd cycles are given in Fig. 4.3.a, when cycled between 0.2–1.2 V. The curvature shows that during the discharge reactions, a stable SEI forms on the electrode surface, and no particular plateau is noted related to the lithiation of Ag particles.

Moreover, a CV test is applied in the first 3 cycles to observe the change in the electrochemical reaction of the SiAg electrode (Fig. 4.3.b). Considering the result of SiAg film when cycled between 0.005–1.2 V (see Fig. 4.3.c), the curvature shape seems to have some differences like the absence of anodic peak at 0.3 V, or cathodic peaks around 0.15 and 0.05 V proving that $Li_{15}Si_4$ and $Li_xAg_y$ phases have not been formed when the cut-off voltage is chosen as 0.2 V. Fig. 4.3.b shows that the anodic (around 0.50 V) and the cathodic (around 0.25 V) peak positions are the same compared to the peaks of pure Si anode. 0.25 V cathodic potential shows the lithiation of Si particles with partial reduction of the electrolyte forming SEI layer. The anodic peak around 0.50 V displays the recovery of the lithiated particles. Plus, the fact that both the anodic and the cathodic peak intensities increase and the cathodic peak shape broaden from the 1$^{st}$ to 3$^{rd}$ cycles could be from the morphological changes in the electrode. When Si particles pulverize following the high volumetric changes, the surface area of the active material (Si particles in that case) increases creating more available spaces in the electrode to react with Li.

For 0.2–1.2 V, the film performs 1825 mAh $g^{-1}$ (99% of the theoretical capacity) as the initial discharge capacity with 95% Coulombic efficiency. Contrary to the common understanding of Si anode, the coulombic efficiency is extremely high. This high reversible lithium ion storage in the first cycle is believed to be related to the existence of Ag particles reducing the irreversible capacity loss by restricting continuous solvent decomposition, hence forming stable SEI film on the electrode [159]. The irreversible capacity (5% of the first discharge reaction) in the first cycle might be due to the reaction of $SiO_2$ particles (chemically bonded or adsorbed oxides formed when the sample was taken out of the deposition chamber) with $Li^+$. During the initial discharge reaction inserted lithium reacts irreversibly first with these oxides forming $Li_2O$ then Li–Si phases. These $Li_2O$ particles (being ionically conductive) along with Ag (being electron conductive) act as conductive buffers to absorb the volume expansion in following cycles. Therefore, 5% decrease in the capacity, for the first cycle might be related to $Li^+$ entrapment in the electrode due to chemical and morphological changes of the film and the passive film formation on the electrode surface following the electrolyte reduction. After 60 cycles, the electrode delivers 1751 mAh $g^{-1}$ with 98% coulombic efficiency, which proves that the electrode retains 95% of its initial discharge capacity after 60 cycles. On the other hand, when the SiAg film is cycled between 0.005–1.2 V, the electrode delivers 2500 mAh $g^{-1}$ as initial discharge capacity with 40% coulombic efficiency. Herein, we particularly chosen 0.005 V as the cut-off voltage since the galvanostatic tests are done in half cells where Li foil is used the counter electrode. Therefore, in order to prevent dendrite growth and short circuit in the cell the lower cut off voltage is chosen as 0.005 instead of 0.0 V. Fig. 4.4.b shows that the electrode performs higher initial discharge capacity due to the increase in the amount of Li reacting with Si crystals to form $Li_{15}Si_4$ and the capacity coming from Ag particles reacting with Li below 0.2 V.

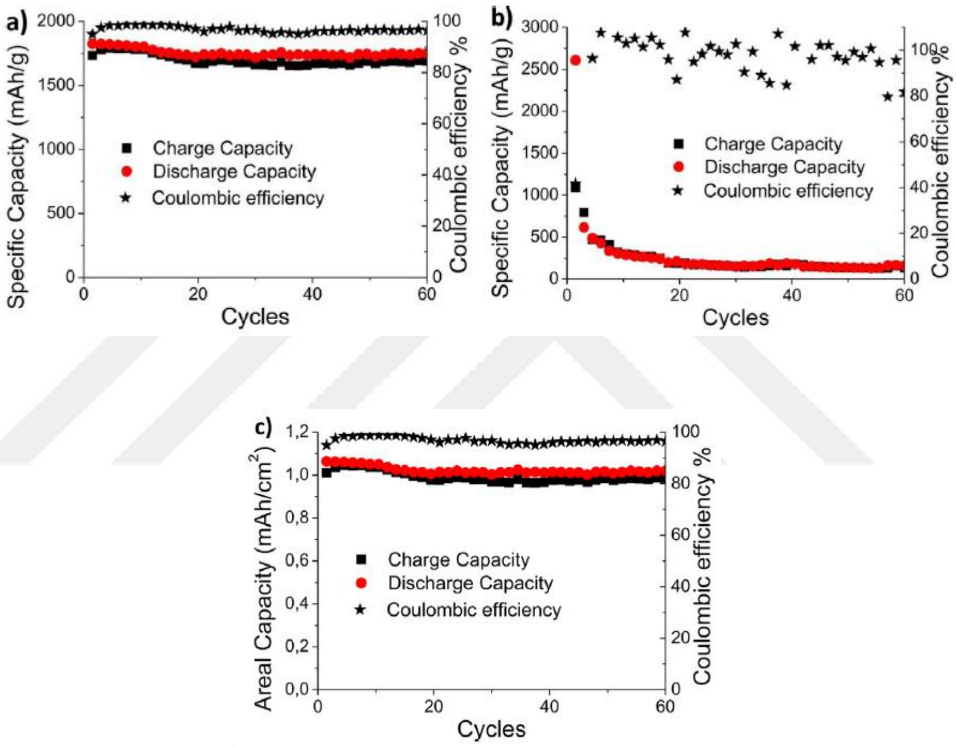


**Figure 4. 4 :** Capacity-cycle graph of the SiAg film a) between 0.2-1.2 V, b) between 0.005-1.2 V; c) Areal capacity-cycle graph of the SiAg film when cycled between 0.2-1.2 V.

The fact that the first efficiency during the 1st cycle and the capacity retention of the electrode (less than 1%) over 60 cycles are very poor in Fig. 4b might be related to several reasons. The formation of Ag–Li–Si ternary lithiated phases in the first cycle seems to be the important one. As Hatchard et al. [54,149] have shown, the amount of Ag is limited in the electrode. Not all Ag and Si incorporate into one single phase (to form Ag–Li–Si ternary phase). Upon the delithiation, Ag phase separates from the Ag–Li–Si phase to form large grains leaving areas of undisturbed a-Si that can form $Li_{15}Si_4$ in following cycles. This phase separation and formation of multiphase-structure are found to be the dominating mechanisms for the quick failure of the SiAg electrode. Moreover, $Li^+$ entrapment in highly stable $Li_xSi$ particles, the SEI formation on the electrode and possible cracking in the electrode following the high volumetric changes could be other reasons for the low electrochemical performances of the SiAg electrode when discharge upto 0.005 V. Since, the stress induced by the high volumetric change can lead a break-up (by cracking) of the surrounding $Li_xSi$ and $Li_2O$ matrix. This causes an electronic and ionic isolation of the particles, limits the removal of lithium from the active particles decreasing the reversibility of the reactions [160].

Indeed, Fig. 4.4.a–b shows that depositing SiAg (with 19.6%at.Ag) film by magnetron sputtering, a highly adherent composite film performing high reversible lithium ion storage (upto 95% over 60 cycles) is formed, when cycled between 1.2 and 0.2 V. Ag in this film behaves like “mechanical buffer”, “interconnectors” and “electron transferring channels” in the Si based electrode [160].

Additionaly, the areal capacity of the SiAg film when cycled between 0.2–1.2 V is also given as Fig. 4.4.c. The results are found to be reasonable (around 1 $mAh/cm^{-2}$) compared to other Si based electrodes' given in some articles [161-162].

The EIS data (Fig. 4.5.a–b) are explained based on the equivalent circuit given in Fig. 4.5c, where $R_s$ is used as uncompensated ohmic resistance, $R_{ct}$ and $R_{SEI}$ as the surface resistance of the electrode and SEI, $C_{dl}$ and $C_{SEI}$ as constant phase element of the coatings (electrical double layer) and the SEI film, and $W_o$ as the Warburg element which describes the solid state diffusion of Li ions. Herein, constant phase element (CPE) is used instead of capacitance because the film is not continuous and the sizes of particles vary around an average. Note that, CPE is not only the double layer capacitance at interface (or SEI), but also lithium intercalation capacitance in the active materials.

The solid lines (black and red) seen in Fig. 4.5.a are the results of experiments and model fitting data, respectively. This proves that the model fits well with EIS data. The fitting values of $R_s$, $R_{SEI}$, $R_{ct}$, $CPE_{SEI}$, $CPE_{dl}$ and $W_o$ are given in Table 4.1.

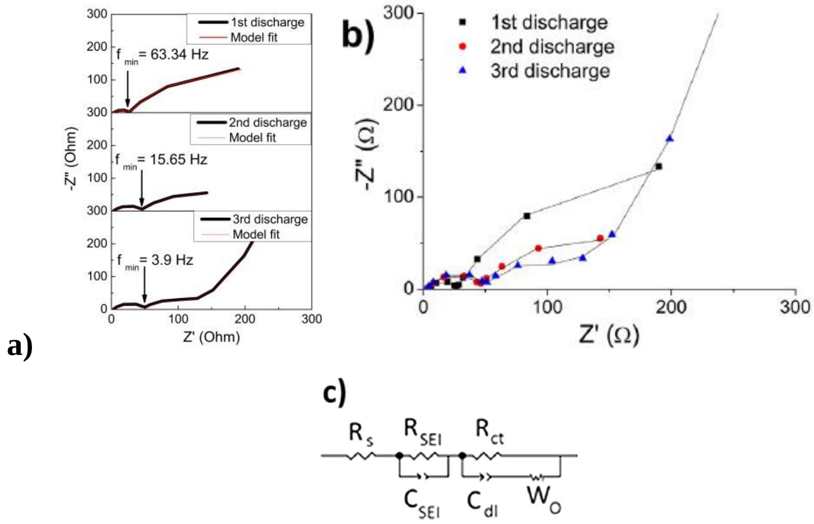


**Figure 4. 5 :** a) EIS test result of SiAg film at 0.2 V for the 1st, 2nd and 3rd cycles, b) EIS test result of SiAg film at 0.2 V for the 1st, 2nd and 3rd cycles, c) Modeling of EIS data.

**Table 4. 1 :** EIS test results of the SiAg film after the 1st, 2nd and 3rd discharge reactions at 0.2 V.

| | $R_s$ (Ω) | $R_{SEI}$ (Ω) | $CPE_{SEI}$ | $R_{CT}$ (Ω) | $CPE_{dl}$ | $W_o$ |
|---|---|---|---|---|---|---|
| 1st discharge | 3.48 | 383.9 | 0.77 | 24.93 | 0.56 | 0.68 |
| 2nd discharge | 2.94 | 178.5 | 0.69 | 44.3 | 0.71 | 0.74 |
| 3rd discharge | 2.97 | 154.1 | 0.50 | 48.49 | 0.78 | 0.86 |

When Nyquist plots of the 1st, 2nd and 3rd discharge reactions are analyzed, it is seen that at high frequencies (around 10 kHz), the spectra display a very low and stable uncompensated resistance values ($Rs < 5\Omega$) which prove that the cells are well assembled and the ionic conduction (through the electrolyte) is well established for the electrode during initial cycles. Knowing that 10 kHz is a low frequency value to get any inductive distortion in the spectra, the resistance seen in Fig. 4.5.a around 10 kHz is a pure resistive behavior ($Z_{im}$ close to 0). This shows that the presence of Ag atoms provides low resistance and stable ionic conductivity to the Si electrode. Knowing that the capacitance depends on the amount of active material reacting with Li, during the cycle test, a decrease in $CPE_{SEI}$ and an increase in $CPE_{dl}$ values are noted which might be explained by a stable passive film formation following the pulverization in initial cycles (Fig. 4.5.a).

In case of lower frequencies (10 kHz–10 Hz), the effect of the surface resistance in parallel with the capacitance is seen as depressed semi-circles in Fig. 4.5.a. In most case, each active component of the electrode (Si) contributes to the surface resistance due to the passive SEI film and the inherent electron transfer resistances, preventing direct electron transfer during cycling. However, the low $R_{ct}$ (<50 Ω) values of the electrode in initial 3 cycles demonstrate that the presence of Ag particles facilitates the electron transfer, hence resulting low polarization and charge transfer resistance of the electrode. Moreover, a decrease in $R_{SEI}$ values (from 383.9 to 154.1 Ω) shows the formation and the prevalence of the stable SEI film on the electrode in cycling, which explain the high reversible lithium ion storage capability of the electrode.

At lower frequencies (below 10 Hz), an upward slope so called Warburg impedance tail is observed for the first 3 cycles. The comparison of the slopes seen in Fig. 5a proves that morphological changes in the electrode cause differentiation in the slope.

The electrochemical analyses results show that when the electrode is cycled between 0.2–1.2 V, Ag presence induces the formation of thinner solid-state interface layer on the electrode which improves the transfer rate of $Li^{+.}$ Moreover, Ag additive also improves the surface electronic conductivity resulting easy transfer of $Li^+$ in the electrode. The low values of $R_{ct}$ and progressive decrease in $R_{SEI}$ values lead a reduction in cell polarization, hence low capacity losses. Therefore, the existence of Ag improves the transfer rate of Li-ion in Si electrode and the surface electronic conductivity [163-164].

To get more information about the reaction kinetic, $f_{min}$ values of each spectrum is examined in detail. This value ($f_{min}$) is found by intersecting the Warburg tail with the mid-frequency arc at the low frequency minima. Fig. 4.5.a display that $f_{min}$ decreases in cycling. This shows that a demarcation between the speed of interfacial and diffusion processes occurs following the SEI formation on both electrode surfaces.

As shown in EIS analyses, the presence of highly electronic-conductive Ag in the Si film is beneficial to reduce the total resistance, which further reduces the surface polarization of electrodes. As a result, the electrochemical properties including cycling stability and rate performance can be improved (Fig. 4.6). By choosing 0.2 V as the cut off potential, SiAg film can cycle in different rates up to 2C (C/6, C/2, C, 2C). The sample still cycles at 2C rate, which obviously support the advantage of co-depositing Ag with Si particles. Herein, it is not surprising to see that the capacity decreases with higher C rates. Low Li diffusion rate and high volumetric expansion are the major reasons for this decrease. Indeed in the galvanostatic tests, the analyzer stops when the voltage drops to a lower cutoff voltage (0.2 V in our case), an increase in the applied current augments IR drop, leading to a drop in the measured capacity. Fig. 4.7.a–b shows that the high Si content of the film and limited porosity in the electrode cause partial cracking and loss of electronic contact with the current collector. In future study, homogeneously distributed porosities could be induced in the SiAg (with 20% at. Ag content) electrode to improve the cycle rate capabilities of the electrode.

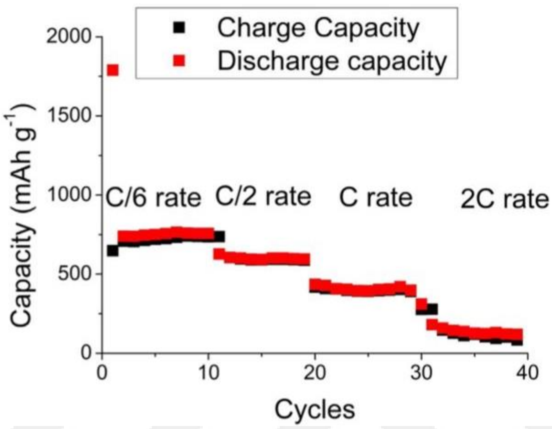


**Figure 4. 6 :** Rate test result of SiAg film.

The ex-situ surface analyses results are given in Fig. 4.8.a–f. During galvanostatic test (between 0.2–1.2 V), pulverization occurs in the electrode while stable SEI films remains on the surface. On the other hand when the sample is cycled between 0.005–1.2 V, cracks are formed during the first lithiation reaction following the high volumetric changes, then such cracks propagate and widen when cycling continues resulting quick failure in the electrode.

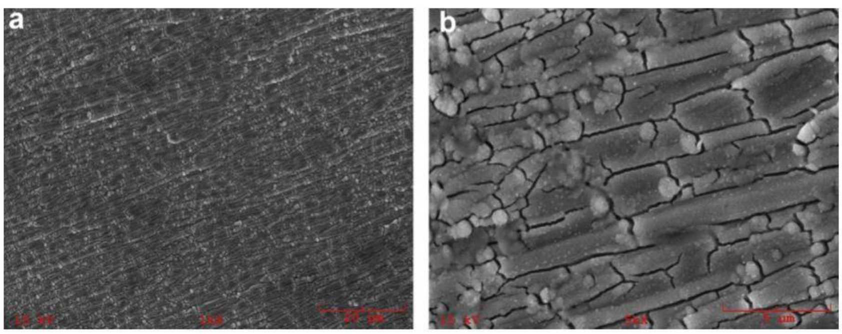


**Figure 4. 7 :** Ex-situ SEM surface view of the SiAg film after the rate test, when cycled between 0.2e1.2 V a) 1000x magnification, b) 5000x magnification.

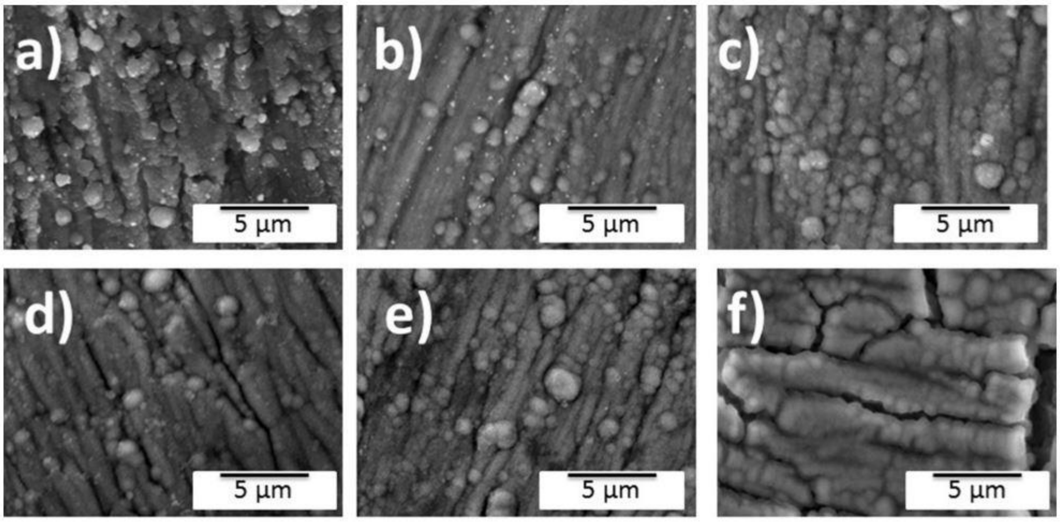


**Figure 4. 8 :** Ex-situ SEM surface view of the SiAg film when cycled 0.2-1.2 V a) after 1st discharge, b) 1st charged, c) 3rd cyles; Ex-situ SEM surface view of the SiAg film when cycled 0.005-1.2 V d) after 1st discharge, e) 1st charged, f) 3rd cyles.

### 4.1.4. Conclusions

In this study, to improve the capacity retention and 1st cycle coulombic efficiency of Si electrodes, 19.6% at. Ag containing Si based composite film is deposited by magnetron sputtering technique.

To understand the reaction mechanism and optimize the electrochemical performance of the electrode the sample is cycled between 0.005-1.2 and 0.2–1.2 V.

The galvanostatic test result shows that the SiAg film (3.2 microns thick) delivers 1825 mAh $g^{-1}$ (99% of its theoretical capacity) initially with 95% Coulombic efficiency and retains 96% of its initial discharge capacity after 60 cycles when cycled between 0.2–1.2 V. The same SiAg electrode performs 2500 mAh $g^{-1}$ as the first discharge capacity with 40% coulombic efficiency and quickly fails in 20 cycles when cycled between 0.005–1.2 V.

By optimizing the electrode composition and adjusting the working potential in the galvanostatic test, it is possible to benefit the advantages of Ag particles in the Si film to get high reversible lithium storage capability, which would have high potential to be used in new generation Li- ion batteries.

## 4.2. Functionally Graded Si Based Thin Films as Negative Electrodes for Next Generation Lithium Ion Batteries [2]

### 4.2.1. Introduction

Lithium ion battery (LIB) technology becomes a common subject of both industry and academia due to increasing demands in electrical vehicles and plug-in applications beside portable devices [165,166]. As the current commercial LIB do not have enough energy density to satisfy customers' requirements finding a safe and a high performance electrode is the main focus of researches.

In this sense, Silicon (Si) becomes remarkable: (1) Si has the highest gravimetric (4200 mAhg$^{-1}$ (9800 mAh ml$^{-1}$) and volumetric capacity) when it is fully lithiated ($Li_{22}Si_5$), (2) lithium rich Si compounds have high melting points, (3) the working potentials vs. lithium (Li) is high enough to eliminate the possibility of metallic-lithium deposition, (4) it is the second most abundant element in the earth's crust and (5) environmentally benign [167-168]. Although Si has many advantages, it does not represent the ultimate solution for anode material since Si electrodes quickly fail in cycling following extreme volume changes. This leads to a breakup of the electrode and electrical isolation of the active material, eventually. Moreover, the low electrical conductivity of Si and a solid electrolyte interface (SEI) formation following the electrolyte reduction on the Si electrode surface impede its effective use as the negative electrode [69,72,86].

To enhance the cycle performance, morphological and compositional improvements have been proposed previously. Researches on morphological improvement emphasize the importance of nanotechnology. The production of nano-scale materials decreases the large stresses formed as a result of volume changes promoting better cyclic stability of the nano-structured electrode compared to the bulk Si. This superior mechanical resistance to fracture can be explained by small sized cracks which do not reach their critical sizes for propagation as they do in bulk materials [166]. In 2012, Yang et al. [169] have shown that the nanoscale fracture and deformation mechanisms could be different from those macroscopic ones and

---

[2] This chapter is based on the paper : Polat, B.D., Keles, O. (2016). Functionally Graded Si Based Thin Films as Negative Electrodes for Next Generation Lithium Ion Batteries. *Electrochimica Acta,* **187**, 293–299

they have proved that many materials at nanoscale are more ductile than they are at the normal sizes since the critical sizes for crack propagation have been found to be larger than the dimensions of nanomaterials, in most cases. Moreover, the morphologies of nanoscale Si can shorten the length of the diffusion pathway and improve Li reaction rate with large surface area of Si. Plus, nanosizing makes the material more reactive and reduces energy barriers for alloy formation [68].

So far, different research groups have used Si thin films as electrodes due to the remarkable advantages like being directly connected to the metallic substrate that leads to minimum capacity loss, having 1D structure to allow efficient electron charge transport, and easy binderless approach of electrode formation to improve its compatibility for mass production [70, 170].

Even though the initial capacity is increased by means of Si film, the first cycles coulombic efficiencies are always low, which prevents its widely used in commercial applications. In this sense, scientists have investigated the lithiation mechanism of Si films and found that the stress induced in the electrode by lithiation reaction is the main reason for their moderate electrochemical performance. Besides that, Pal et al. [171] have stated that the small amount of segregants and impurities may have a major effect on the adhesion and this could embrittle the interface (electrode/current collector) resulting failure.

Previously, it has been shown that the high volumetric changes in the Si thin film electrode cause a vertical cracking which leads small islands formation after the first cycle [56, 87, 172]. These islands help the electrode to release the stress while maintaining electronic contact with the current collector. Therefore, the electrode keeps cycling even though the capacity decreases gradually. However, as the Si film thickness increases, after few cycles, the capacity drops precipitously due to high impedance and huge mechanical stress induced in the film, therefore the islands delaminate severely from the current collector resulting in a complete failure.

Some researchers have suggested to improve the mechanical stability of Si thin film anodes by either forming alloy (Fe, Co, Ni, Sn) with other materials to act as a buffer or by using nano-sized materials dispersed uniformly in a buffer matrix [173, 174]. Herein, copper (Cu) is used as an inactive but beneficial additive material in various forms other than substrate or current collector. Indeed, in previous studies, Sethuraman et al. [154] have found that Cu appears to act as a glue that binds the electrode together and prevents the electronic isolation of Si particles, consequently decreasing the capacity loss. Furthermore, Murugesan et al. [175] have demonstrated that Cu coating on Si reduces charge transfer resistance, improves the reversibility of the lithiation reaction and promotes the mechanical tolerance to volume expansion. In addition Kim et al. [97] have deposited Cu film by electroless deposition on the composite Si anode. The resulting film performs a remarkable improvement in the cycleability, as expected.

In this work, to control the stress propagation in the film and to promote the integrity of the electrode in cycling we propose to use functionally-graded SiCu film as a negative electrode. The film is designed to have pure Cu, then Cu rich layer close to the electrode/current collector interface and 10%at. Cu-90%at.Si content toward the top of the film (electrode/electrolyte interface). Cu is particularly chosen to be used with Si because it exhibits considerable plastic flow during electrochemical cycling, which is expected to impede the crack propagation. Moreover, its highly electron conductive behavior creates new electron pathway in the film to increases the cycling and rate efficiencies. Plus, its electrochemically inactive behavior vs Li would optimize the volumetric changes in the electrode. And, the existence of Cu atoms at the bottom is believed to increase the adhesion of the film to the Cu current collector [176-178]. The advantages of structured Si thin film electrodes prepared by means of various deposition methods including chemical vapor deposition, sputtering and evaporation have been reported by many bulk and micro-battery research groups [72, 179-181]. Among alternatives, magnetron sputtering is preferred because highly energetic sputtered particles (Cu and Si in our case) are expected to form intermetallics in the coating as well as increase the adhesion of the film. The originality of this work lies on engineering a functionally graded coating to relieve the stresses within the electrode and improve the adhesion of the film to the substrate without sacrifying the capacity delivered by the cell.

### 4.2.2. Experiments

A functionally-graded SiCu film is produced by using an advanced energy switching power supplies for DC sputtering process to prevent arcing in Si cathode (a CemeCon CC800/9 magnetron-sputtering system). The schematic representation of the experimental setup is given in Fig. 4.9.a. Both Si and Cu targets have high purities (99.9 at.%). The substrates are cleaned with acetone and isopropyl alcohol before being placed in the coating chamber.

The chamber is pumped down to a base pressure of less than $10^{-5}$ Pa. First, Ar etching is applied to the substrates at 550 V. Then, the bipolar pulsed with 250 kHz frequency and 1600 ns reverse time (duty cycle is 60%) is applied. The deposition takes 240 minutes and -100 V bias is applied on the substrate (Fig. 4.9.a).

Once pure Cu is sputtered for 5 min., the sputtering rate of Si is gradually increasing (15 W $min^{-1}$) for the following 170 min. up to a level where 10%at. Cu- 90%at. Si containing thin film is deposited. Then the sputtering ratio stabilizes and 10%at. Cu and 90%at. Si containing film is sputtered for the last 65 min. with the power applied to the Si (2500 W) and Cu (350 W).

The films are deposited on four different substrates: Glass discs (Thermascal) for X-ray diffraction (XRD) analysis, Si wafers for cross sectional view, stainless steel discs (304 type, 15.5-mm diameter and 1.5-mm thickness) for compositional analysis and mechanically polished (1200 nm, 800 nm, 600 nm, 320 nm, 3 mm, 1 mm, 0.5 mm) Cu discs (15.5-mm diameter and 1.5-mm thickness) for electrochemical experiments.

The amount of Si and Cu atoms along the film thickness is monitored by glow discharge optical emission spectroscopy (GDOES) analysis (JobinYconHoriba), where the RF excitation mode is used with 50 W power and 900 Pa pressure using the films coated on SS substrates.

The surface morphology of the films before and after the cycle tests as well as the film thicknesses are investigated by field-emission scanning electron microscopy (FEGSEM, JEOL JSM 7000F). To demonstrate the changes in film morphologies in cycling, the cell is discharged, and cycled for 1st, 5th and 20th cycles, then disassembled in the glove box. The discharged and cycled electrodes are washed with DMC (dimethyl carbonate) and naturally dried in the glove box prior to surface analysis by FEG-SEM.

The phases present in the coatings are determined using the Philips PW3710 XRD System with a 2θ range of $10–100^0$ in steps of 0.05 (with CuKa at 40 kV and 30 mA). Electrochemical performances of the functionally-graded SiCu thin film electrodes are measured using a 2032 button coin cells, which are prepared in an Ar filled glove box (MBRAUN, Labmaster). The cell assembling is done in the following sequence: the working electrode is placed on the lower cap of the cell, then drops of electrolyte (1 M $LiPF_6$ in the ethylene carbonate-dimethyl carbonate, (EC:DMC 1:1) (Merck Battery Grade)), separator (Celgrad 2400), lithium metal foil as the counter electrode, the spring and the upper cap of the cell are put on top of each other. Once the cell is assembled in the right order, it is sealed by a pressure crimper inside a glove box. The galvanostatic tests are made at room temperature in between 0.2-1.2 V (vs Li/Li) with a rate of 100 mA $g^{-1}$.

The weights of the thin films were measured by using (My weight i101) microbalance before and after the deposition process.

The mass of the coating is multiplied by the weight percentage of the active material that is revealed by EDS (Oxford) analysis. The specific capacity of the sample is calculated based on the active material weight in the coating.

Cyclic voltammetry (CV) was performed for the 1st and 20th cycles in the potential range of 0.2 V-1.2 V (vs $Li/Li^+$) at a scan rate 0.03 $mVs^{-1}$. EIS analyses are done on the 1st, 2nd and 3rd cycled samples in the frequency range of 10 mHz-65 kHz with 10 mV rms at 0.2 V (Gamry PCI4/750) discharge potential.

Finally, to evaluate the rate-capability of the functionally graded SiCu film, series of galvanostatic tests with different rates are performed. The rate capability of the electrode is measured when the sample is charging with 100 mA $g^{-1}$ rate and discharging at different rates from 200 to 500 mA $g^{-1}$ (200, 300, 400 and 500 mA $g^{-1}$). Both charging and discharging are conducted between 1.2 and 0.2 V vs $Li/Li^+$. Since the discharge capacities at higher rates are lower than the charge capacity, 60 minutes open circuit-potential relaxation is performed before the subsequent discharge reaction, as suggested by Sethuraman et al. [154]. This enables that the electrode retains its low state-of-charge before the beginning of each rate experiment.

### 4.2.3. Results and discussions

The surface and the cross sectional SEM images of the functionally graded SiCu films are shown in Fig. 4.9.b-c. From the top view, the morphology shows a typical sputtered film where the seams between the columnar structures are remarkably noticed in Fig. 4.9.b. The cross sectional image shows that the film has a thickness around 2.4 μm which is fairly thick for thin film anodes (Fig. 4.9.c). EDS analysis reveals the presence of 39.6 %at. Cu in the film. The oxygen and argon content of the films are also noted less than 5%at.

GDOES depth profile results exhibit the changes in the amount of Si and Cu atoms along the film thickness. Si/Cu atomic ratio is increased for 1700 nm (approximately) after the first 50 nm of pure Cu, then becomes stable for the last 600 nm (approximately), as expected (Fig. 4.10.a).

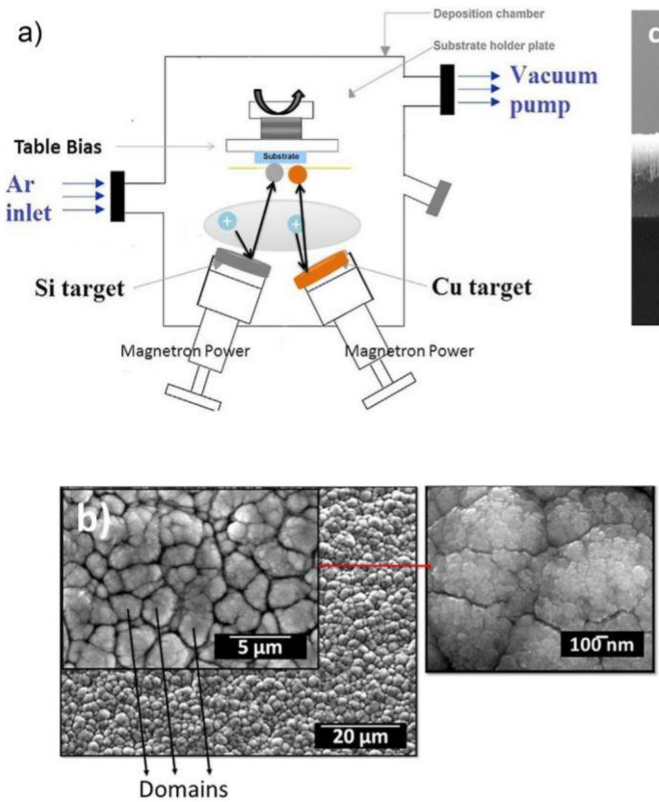


**Figure 4. 9 :** a) Experimental Setup for magnetron sputtering, b) SEM surface and c) SEM cross sectional views of the functionally graded film.

The structural properties of the films are further investigated by means of XRD (Fig. 4.10.b), which is taken from the film coated on the glass discs. The XRD diffractogram for the glass substrate show amorphous structure, as expected (Fig. 4.10.c). Fig. 4.10.b shows that the film contains crystalline states of $Cu_3Si$ intermetallic (JCPDS: 00051-0916) in addition to nanosized crystalline particles of which presence is shown as a slope in low diffraction angles ($2\theta < 20^0$). The reaction of $Cu_3Si$ with Li and its high electronic conductivity are expected to increase the electrochemical performance of the electrode.

Because, $Cu_3Si$ particles improve the electrical conduction pathways in the composite and increase the adhesion of the SiCu film to the Cu current collector. Plus, $Cu_3Si$ particles act as buffer to accommodate the volume-expansion and they minimize electrochemical agglomeration of Si in cycling [175]. The reaction mechanism of $Cu_3Si$ with Li has been described previously [ 175, 182-183].

During lithiation, the elemental Cu is ejected from the $Cu_3Si$ crystal and would act as a buffering matrix to minimize the destroying effect of the volume changes due to $Li_xSi$ formation (Eq. 4.1). This lithiated Si product surrounded by the conductive Cu matrix enhances the reversibility of the charge/discharge reactions, which intensifies the cycle stability of the electrode, eventually (see Eq. 4.1–4.2).

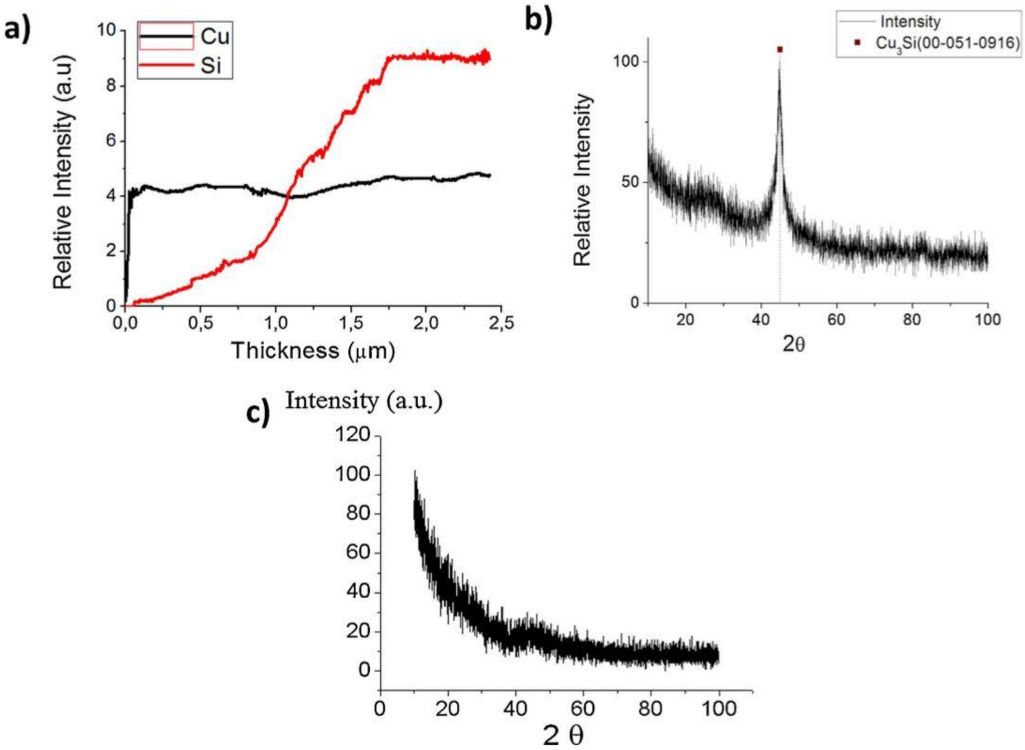


**Figure 4. 10 :** a) GDOES analyses of the functionally graded SiCu film, b) XRD results the functionally graded film, c) XRD results of the glass substrate.

$$xLi^+ + xe^- + Cu_3Si \rightarrow Li_xSi + 3Cu \quad (4.1)$$

$$Li_xSi + 3Cu \leftrightarrow 3Cu + Si + xLi^+ + xe^- \quad (4.2)$$

The absence of Cu and Si crystal peaks justifies the presence of Cu and Si particles as amorphous/nanocrystalline states in the film.

In previous studies, $Li^+$ insertion/extraction mechanisms in Si are analyzed by using in-situ XRD, SEM and high resolution transmission electron microscopy methods (HR-TEM) [50,53,155-184].

In these papers, the scientists have reported that in compliance with the "solid-state amorphization theory", during Li insertion, the crystal structure of the nano-sized Si particle is destroyed and converted into an amorphous metastable structure (Li-Si) without formation of intermediate phases. This amorphous lithiated Si phase prevails up to 0.05 V, followed by the formation of a new crystalline ($Li_{15}Si_4$) compound when the cell potential goes down to lower values (V < 0.05 V). Furthermore, studies point out that during $Li^+$ extraction (on the anodic side), crystalline Li is converted into two different phases (amorphous and crystalline), where $Li^+$ ions are trapped resulting in a decrease in the specific capacity delivered by the electrodes. On the other hand, the amorphous Si particles form amorphous lithiated particles in discharging. The formation of a new crystalline ($Li_{15}Si_4$) compound is found to be dependent on both the voltage of the cell and the thickness of the film. Therefore, more stable cycle performance would be achieved by using a-Si as anode material when cycled with a lower cut-off voltage > 0.2 V. Therefore, to eliminate irreversible lithiation reactions and to optimize the volume expansion in the anode the lower cut off potential of the galvanostatic test is fixed to 0.2 V.

The $Li^+$ insertion/removal mechanism of the graded films is investigated by CV test, for the 1$^{st}$, 2$^{nd}$, 3$^{rd}$ and 20$^{th}$ cycles (Fig. 4.11).

Fig. 4.11 shows that the electrode has one remarkable cathodic (around 0.2 V) and anodic (around 0.6 V) peaks of which intensities decrease after the 1st cycle justifying possible solid electrolyte interface (SEI) formation. Moreover, the peak broadenings seen after 20$^{th}$ cycle indicates the occurrence of morphological changes.

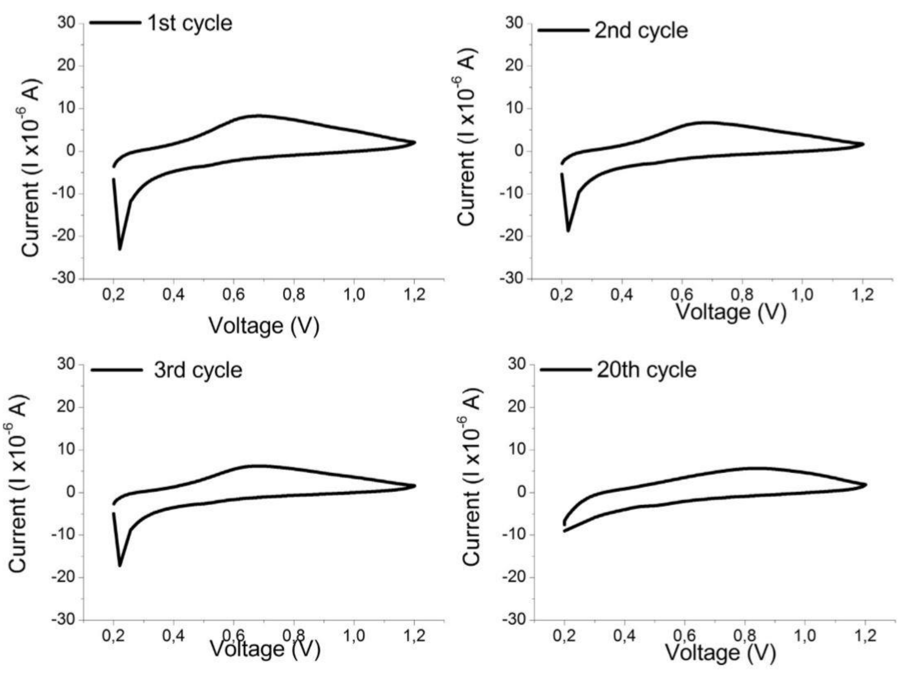


**Figure 4. 11 :** CV test results of the functionally graded film for the 1st, 2nd, 3rd and 20th cycles.

Fig. 4.12 shows the charge/discharge cycling data for the functionally graded electrode. The result is different than that of the composite SiCu electrode [185]. The capacity-cycle diagram of the composite electrode shows that the amount of capacity delivered by the anode in 100 cycles decreases gradually and attains to a value lower than that of carbon electrode [185]. Such a dramatic failure may occur due to a significant loss of electronic contact between the coating and the current collector. It is believed that beside the continuous SEI formation, some delamination is formed during the first cycle, then the delamination becomes prominent when cycling continues resulting in a continuous decay of capacity.

On the other hand, the capacity-cycle diagram of the functionally graded SiCu film shows 2073 mAh $g^{-1}$ as the first discharge capacity with 80% coulombic efficiency. The capacity delivered by the electrode decreases in the first 3 cycles, then increases very smoothly at the $5^{th}$ cycles and decreases again up to 10 cycle. This fluctuation in the first 10 cycles stabilizes around 1500 mAh $g^{-1}$ with 99% coulombic efficiency. So far in literature, for such a thick film electrode, this abrupt stabilization in the capacity has not been noted.

Particularity in the composition and the structure of the coating would explain this peculiar behavior. Indeed, this fluctuation noted in the first 10 cycles could be explained regarding the compressive and tensile stresses that the electrode undergoes during cycling. The existence of the graded film diverts the propagation of the stresses along the film and increases the adhesion of the coating to the current collector resulting in a high cycle performance. It is believed that particularly the existence of Cu atoms (inactive versus $Li^+$) at the electrode/current collector interface help the coating to maintain its integrity even though some cracks are formed.

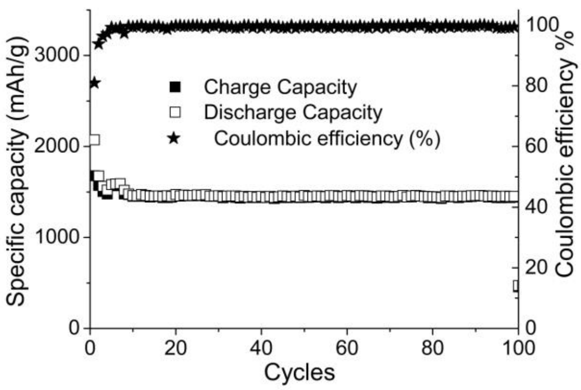


**Figure 4. 12 :** Capacity-cycle plots of the functionally-graded SiCu thin films.

To get more detailed explanation about the electrochemical performance of the functionallygraded electrode, EIS tests have been applied to the sample after the 1st and $30^{th}$ cycles at 0.2 V (Fig. 4.13.a). The EIS data are explained based on the equivalent circuit given in Fig. 5b, where $R_1$, $R_2$ and $R_3$ are used as uncompensated ohmic, solid electrolyte interface and charge-transfer resistances of the electrode,$CPE_1$ and $CPE_2$ are named for constant phase element of the SEI and of the coating with the electrolyte interface. Finally $W_0$is used as the Warburg element which describes the solid state diffusion inside the coating.

Herein, constant phase element (CPE) is used instead of capacitance because the films are not continuous and the sizes of particles are distributed around an average. Note that $CPE_2$ is not only the double layer capacitance at interface, but also includes lithium intercalation capacitance in the active materials.

The square dots and the solid line seen in Fig. 4.13.a are the results of experiments and model fitting data, respectively. This proves that the model fits well with EIS data. When the Nyquist plots of the $1^{st}$ and $30^{th}$ cycled samples are analyzed, it is seen that at high frequencies (around 10 kHz), the spectra of both samples display very low and stable uncompensated resistance values ($R_1$<5 V). Knowing that 10 kHz is a low frequency value to get any inductive distortion in the spectra, the resistance seen in Fig. 4.13.a around 10 kHz is a pure resistive behavior (Zim close to 0). Engineering a functionally graded electrode design promotes the connection between the substrate and the coating avoiding any delamination during cycling while taking advantage of the high amount of Si atoms on top.

In case of lower frequencies (10 kHz-10 Hz), beside the SEI formation ($R_2$ and $CPE_1$), the effect of the surface resistance ($R_2$ and $CPE_2$) in parallel with the capacitance is seen as a depressed semicircle in Fig. 4.13.a. Each active component of the electrode contributes to the surface resistance due to both the SEI passive film and the electron transfer resistances preventing direct electron transfer during cycling. A remarkable increase in $R_2$ values (from 2.67 to 42.34 V) could be attributed to the growth in SEI film thickness. When the changes in $R_3$ values are observed, an increase from 13.91 V to 38.53 V is noted. Knowing that the electrical conductivity and the morphology of the active material affect the charge transfer resistance value, this increase in R values shows that the electrode undergoes morphological changes (cracking) during cycling. It is believed that as this graded film is well adhered to the Cu substrate the changes in stress along the electrode causes cracking of the film (without delamination from the current collector) exposing fresh active materials (Cu particles in that case) to $Li^+$ which would be also passivated following the electrolyte reduction. At lower frequencies (below 10 Hz), the Warburg tail accounts for diffusion limitations in the electrode, which includes diffusion through the electrolyte, the electrode surface layers, and the active particles.

Fig. 4.13.a shows that $Li^+$ can diffuse in the electrode during the galvanostatic test. As cycling proceeds morphological changes and SEI formation become more prominent causing changes in Li diffusion kinetic as seen by the deviation of the slope.

a)

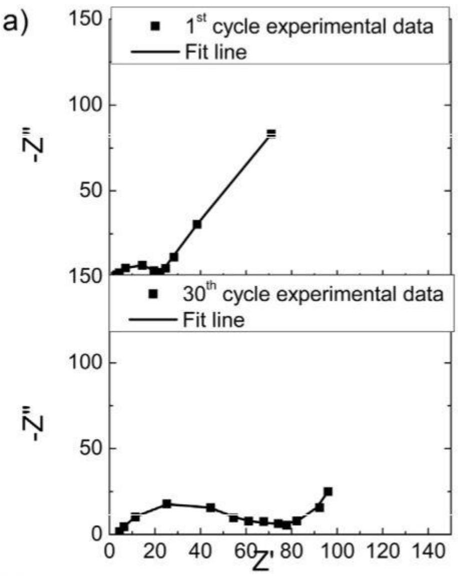


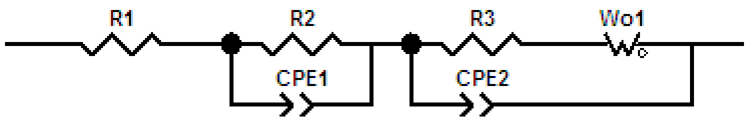


b)

**Figure 4. 13 :** EIS test results of a) the functionally graded composition films at 0.2V for the 1st and 30th cycled samples (dots for the experimental data, line for the model fitting), b) Schematic representation of the model to explain EIS data.

To evaluate the possible use of this functionally graded SiCu electrode in high energy density applications, the rate test is applied on the electrode (Fig. 4.14). The result of the rate-capability test is in well agreement with the above mentioned lithiation mechanism.

Fig. 4.14. shows that once the cycle rate is increased from 100 to 500 mA $g^{-1}$, the amount of capacity delivered by the anode decreases upto 700 mAh $g^{-1}$. Herein, the fact that the sample delivers roughly 700 mAh $g^{-1}$ discharge capacity at different cycle rates (200, 300, 400, 500 mA $g^{-1}$ rates) proves the enhanced capability, which is related to the improved stress relief behavior in the graded film.

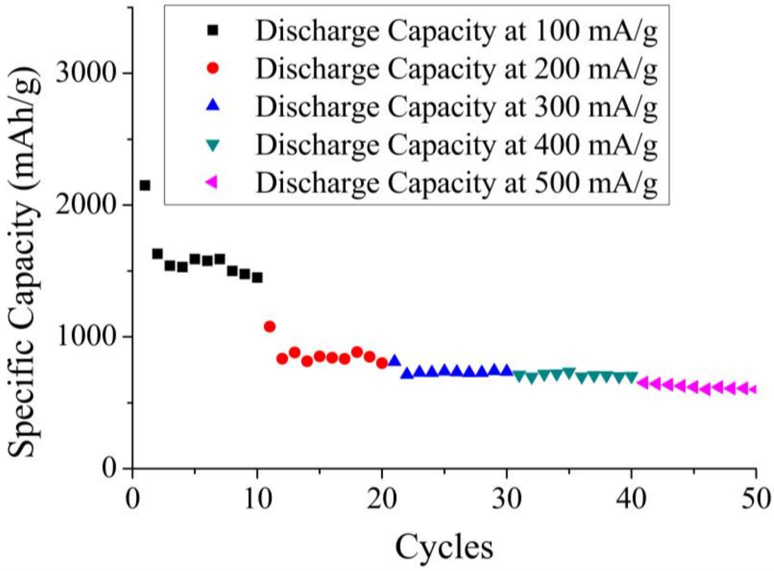


**Figure 4. 14 :** Rate test results of the functionally graded SiCu thin films.

The SEM views of the samples after the 1st discharge, 1$^{st}$ charge, 5$^{th}$ and 20$^{th}$ cycles (Fig. 4.15.a–d) support the above-mentioned lithiation mechanism. After the first discharge reaction, the particles are swollen and covered by the SEI layer, plus no additional electrochemical reaction induced cracks are detected along and inside the domains on the SEM views of the sample (Fig. 4.15.a). This fact is in agreement with the EIS data (Fig. 4.13.a). Then after the 1$^{st}$ charge reaction (delithiation) a noticeable shrinkage in the domain size is seen (Fig. 4.15.b). This delithiated film shows nanosized pores on the domains (Fig. 4.15.b closer view, upper left side).

These pores are assumed to be formed following the displacement of Li from the structure. After the 5$^{th}$ cycle, pronounced enlargements are noticed in the seams (spaces between the columnar structures of the film) forming micron-sized islands. We believe that engineering such a gradually changing composition in the film by magnetron sputtering changes the stress propagation in the electrode and holds the structure together due to the high adherence of the film. The enlargements at the seams expose fresh active particles to react with Li causing a fluctuation in the capacity since once SEI covers these particles, the capacity delivered by the electrode decreases smoothly and stabilizes around 1500 mAh $g^{-1.}$

Herein it is important to note that the interspaces remain the same proving that the electrode is able to withstand the volumetric changes (Fig. 4.15.c-d).

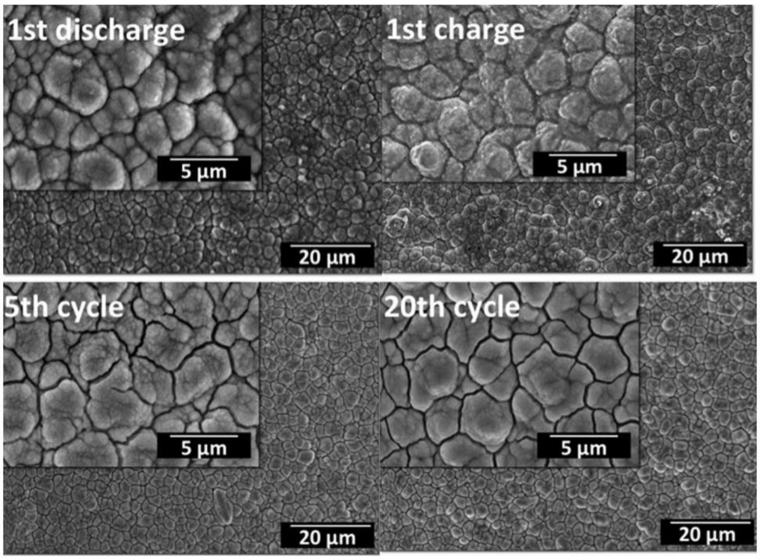


**Figure 4. 15 :** SEM surface views of the functionally graded film after a) 1st discharge, b) $1^{st}$ cycle, c) $5^{th}$ and d) $20^{th}$ cycles.

### 4.2.4. Conclusions

In this work, we engineered a functionally-graded SiCu films by magnetron sputtering technique. The outcomes of this study are summarized below:

- Common understanding suggests that an increase in film thickness causes quick failure of electrodes. However, this study shows that by an accurate materials selection (Cu and Si) and structural design (Cu rich at bottom and Si rich on top) an electrode having 2.4 µm thickness retains 70% of its initial capacity after $100^{th}$ cycle.
- This work displays the advantages of using functionally-graded film as anode in LIB. The gradient film has a composition profile that changes continuously from pure Cu layer to 10%at. Cu containing Si film. The existence of Cu atoms in the coating is believed to hinder quick failure of the Si electrode in initial cycles due to improved ductility, enhanced adhesion and defocusing ability of the film aganist the stress formed in cyling.
- The co-existence of Cu and Si highly energetic particles promotes the intermetallic formation ($Cu_3Si$) in the electrode which would increase the reversibility during lithiation.

- Seams present in the sputtered film help to accomodate electrochemically induced stress in cycling. In initial cycles, fresh particle exposures through cracks compete with SEI growth.
- Once the interlayer between the electrode and the electrolyte is settled then the electrochemical performance becomes stable around 1500 mAh $g^{-1}$.
- A clear understanding on the relationship between morphological, structural design and electrochemical performance of the thin films has been made. This would increase the likelihood of making high capacity Si based anodes for the next generation LIB.

## 4.3. Compositionally-Graded Silicon-Copper Helical Arrays as Anodes for Lithium-Ion Batteries [3]

### 4.3.1. Introduction

In response to the needs of modern society and emerging ecological concerns, it is now essential to use low-cost and environmentally friendly energy storage systems. Innovations in energy storage devices result from better material selection and process design.

Among alternative energy storage devices, lithium-ion batteries (LIB) are important in today's world since they are providing electrical power for a wide variety of applications, such as power tools, electrical vehicles, aerospace vehicles, power grids, and small portable electronic devices. So far, various materials (C, Sn, Ge, Al, Sb, and Bi) have been evaluated as anodes in LIB [186-189]. Among them, silicon (Si) is especially attractive due to its high theoretical storage capacity (3579 mAh $g^{-1}$ at room temperature) and high abundance in the Earth's crust. Nonetheless, Si has not yet replaced graphite in commercial applications because >300% volume expansion occurs when the lithium ions ($Li^+$) react with Si during cycling, generating an immense stress (as high as 1 GPa) in the anode. This immense stress causes a break-up of the electrode and the electrical isolation of Si [190]. Moreover, as the electrochemical alloying potential of Si is above the electrolyte solvent reduction

[3] This chapter is based on the paper : Polat, B.D., Keles, O., Amine, K. (2016) Compositionally-Graded Silicon-Copper Helical Arrays as Anodes for Lithium-Ion Batteries. *Journal of Power Sources*, **304** 273-281.

level, a passive film forms at the electrode/electrolyte interface. Finally, the high electrical resistivity and the low diffusion coefficient of Li in Si hinder fast electron transfers, resulting in high resistance along the electrode and, hence, failure in the early stages of cycling [190, 191].

Despite these challenges, the extraordinarily high energy capacity of Si has motivated researchers to develop techniques to reduce the limitations of Si as a practical anode material. For example, nanoscale morphologies, including thin films, nanowires, and nanotubes, have been designed [189-196]. The free spaces among these nanostructures form large pathways to facilitate electrolyte penetration, increase the accessible surface area of the anode reacting with $Li^+$, and decrease the polarization. Thus, the cycling performance of the electrode improves. In addition to the above, template-directed plating, direct chemical reaction, and nano- lithography have all been used by various researchers to produce composite nanostructured Si based thin film electrodes [197-199]. However, long processing time, the restricted aspect ratio of the nanostructures, safety concerns, difficulties in controlling the morphology, low adhesion of the film to the current collector, and limited choices of materials to form composite nanostructures have led investigators to look for alternative production methods.

In this sense, glancing angle deposition (GLAD) becomes remarkable since it has shown promise for generating thin-film anodes. The advantages of the GLAD method and its film formation mechanism have been explained in detail [127, 197-201]. In this method, process parameters (especially angle of incidence, evaporation rate, and substrate rotation speed) change the morphology of the microstructures from zigzag to helices.

Therefore, in this work we particularly form helices by GLAD method to improve mechanical integrity of the electrode. Therefore, a three-dimensional (3D) helix-containing film is expected to act as “micro-springs” [201] due to its particular morphology, as revealed by Seto et al. [202]. Plus, the separated helical structures enable freedom of ion movement over short distances, which would also improve mechanical tolerance of the electrode to the stress induced by volumetric changes in cycling.

Even though the cycle life of the anode is improved as a result of the helical morphology (improved electrode design), the service life of nanostructured thin films is still limited owing to the low electrical conductivity of Si and the high ohmic contact resistance between the thin film and its substrate [178]. Thus, to promote electron transfer along the nanostructures, to improve the adhesion of the film to the substrate, to alleviate the influence of expansion and to divert the stress formed along the helice additional Cu was incorporated into the structured film (improved material selection) [97, 176, 203] Previous studies had suggested that depositing Cu atoms on/with Si particles would significantly improve the electrical contact, the coulombic efficiency, and the cycle life of the electrode [176, 203]. However, deciding the optimum amount of Cu to add into the Si thin film is a challenging task. Although Cu increases the cycleability of the Si thin film, the theoretical capacity of the film decreases because Cu is electrochemically inactive versus Li. Therefore, optimization of Cu/Si ratios along the nanostructured thin film is highly desired.

One approach to handling this problem is to engineer a CuSi nanostructure with high surface area, where the Cu/Si ratio gradually changes from the substrate to the top of the nanostructure.

In this work, first in literature we have adopted ion assisted deposition technique to glancing angle deposition method and have used compositionally graded structuring to produce a thin film having compositionally-graded SiCu helices. During the film growth, the ratio between Cu and Si was precisely controlled and dynamically tuned. For comparison, a pure Si helices containing thin film is also produced in the same experimental conditions. A lithiation mechanism for anodes with the compositionally graded helices is proposed on the basis of electrochemical impedance spectroscopy at different states of charge and cyclic voltammetry for different cycles.

#### 4.3.2. Experiments

The experimental setup used in this study is given in Fig. 4.16.a. During the GLAD evaporation stage, two quartz-crystal microbal- ances (QCMs) were used independently to monitor the deposition rates and thicknesses of Cu and Si, separately.

Four kinds of substrates were used: a Si wafer for cross-sectional scanning electron microscopy (SEM), a stainless steel disc (15.5- mm diameter and 1.5-mm thickness) for compositional analysis, a glass disc (Tedpella) for structural analysis, and a mirror-like surface-finished copper disc (15.5-mm diameter and 1.5-mm thick- ness) for electrochemical experiments.

The pure Si and Cu pellet source materials were placed in separate graphite crucibles, and the chamber was pumped to a base pressure of about 3 $10^{-6}$ Pa. Prior to deposition, the samples were initially sputtered for 8 min using 900 eV$Ar^+$ ions from a Kaufman ion source at a gas feeding rate of 8 sccm. The incident angle of $Ar^+$ ions to the substrate's normal orientation was about $35^0$, and the pressure in the chamber was 0.01 Pa. Then, the shutters inserted for each source were opened, and the deposition was started. The deposition time was 15 min.

To form helices, the substrate was rotated by a stepper motor with an azimuthal rotational speed of 0.2 rpm, when the crucible surface has $85^0$ with substrate surface normal. To obtain gradual compositional variation along the helices, the evaporation rates of the Si and Cu sources were separately controlled. The evaporation rate of Si was 1 nm $s^{-1}$ during the entire process, but that of Cu changed from 0.3 nm $s^{-1}$ in the first 2 min, then to 0.18 nm $s^{-1}$ in the following 5 min, and finally to 0.09 nm $s^{-1}$ for the last 8 min, as read by the QCM (Fig. 4.16.a)

After cleaning (sputtering), immediately at the start of deposition, the ion energy was reduced to 250 eV, and $Ar^+$ ion-assisted deposition was conducted at 250 V and 23 mA for 5 min to establish a dense, adherent thin film. After that, the Ar flow and ion gun were turned off, but evaporation still continued. The ion source parameters used in the experiments were as follows: 30 mA beam, 40 V discharge, 100 V accelerator. For comparison, in the same experimental conditions a pure Si film with helices is deposited on the substrates.

The surface morphology and the thickness of the “pristine” (i.e., no charging or discharging) Si and SiCu thin films were determined with field-emission SEM (JEOL JSM 7000F and JEOL 5410). The phases present in the pristine SiCu thin film were determined by x- ray diffraction (XRD) analysis (Philips PW3710 System) with a 2θ range of 10-$90^0$ in steps of $0.05^0$ (with CuKa at 40 kV and 30 mA). The amount of Cu/Si atoms along the thin film thickness was monitored by glow discharge optical emission spectroscopy (GDOES) analysis (JobinYcon Horiba), where the RF excitation mode is used with 50 W power and 900 Pa pressure.

The composition of the film was determined by energy dispersive x-ray (EDS) analysis (Oxford). The weights of the films were measured by a microbalance (My Weigh Balance 101) before and after the coating process.

For electrochemical testing, half-cells were assembled as 2032 coin cells in an Ar-filled glove box (Mbraun, Labmaster). These cells included the test electrode (with the compositionally graded helices and Si helices), a counter electrode of pure Li foil, and a sepa- rator of porous polypropylene film (Celgrad 2400). The non-aqueous electrolyte was 1 M $LiPF_6$ dissolved in ethylene carbon- ate (EC) and dimethyl carbonate (DMC) in a 1:1 weight ratio. To improve the stability of the solideelectrolyte interface (SEI) on the electrode, 10% vol. fluoroethylene carbonate (FEC) was added into the electrolyte [204]. The cells were tested at room temperature and operated at a voltage range of 0.2 V-1.2 V versus $Li/Li^+$ with a rate of 100 mA $g^{-1}$. To compare the surface views after the 3$^{rd}$ cycle, 30$^{th}$ cycle, and 100$^{th}$ cycle, the cycled electrodes were washed with DMC and naturally dried in the glove box prior to examination of their surfaces by field emission SEM.

Furthermore, an HS-3E test cell (Hohsen Corp., Japan) was used to accomplish cyclic voltammetry (CV) and electrochemical impedance spectroscopy (EIS) in a three-electrode configuration. Details were given in a previous study [184].

Cyclic voltammetry was performed for the 1$^{st}$, 2$^{nd}$, 3$^{rd}$, and 30$^{th}$ cycles in the potential range of 0.2-1.2 V (vs $Li/Li^+$) at a scan rate 0.03 mV $s^{-1}$, and EIS analyses were done on the pristine and the 30$^{th}$ cycle samples in the frequency range of 10 mHz-10 kHz with 10 mV (rms) at discharge potentials of 1.2, 0.6, and 0.2 V (Gamry PCI4/750). To derive the impedance of the samples at 1.2 V, the cell was discharged, then a certain amount of time was allowed for potential relaxation at the open circuit voltage (OCV) condition (until the OCV potential drift was less than 0.5 mV $h^{-1}$). Once that condition was established, the impedance of the sample was measured at that discharged potential. This procedure was repeated for EIS measurements at 1.2, 0.6 and 0.2 V.

To evaluate the rate capability of the half cells, charging at 100 mA $g^{-1}$ and discharging at 100-400 mA $g^{-1}$ (100, 200, 300, and 400 mA $g^{-1}$) were done over a voltage range between 1.2 and 0.2 V vs. $Li/Li^+$. Since the discharge capacities at higher rates were lower than the charge capacities at 100 mA $g^{-1}$, OCV relaxation for 60 min was performed before the start of the subsequent test at higher discharge rate, as suggested by Sethuraman et al. [154] This step enables the electrode to retain its low state of charge before the beginning of each rate test.

### 4.3.3. Results and discussions

Fig. 4.16.b show the Si and Si-Cu coatings' surfaces and cross sectional views. Both films a have thickness around 600 ± 40 nm. Although both films have made of

helices, a closer view reveals the Si film has irregular helical morphology along the film thickness, but the Si-Cu film contains a homogenously distributed array of well-aligned helices. The density of the helices is around 6.6 helices mm$^{-2}$ (Fig. 4.16.b).

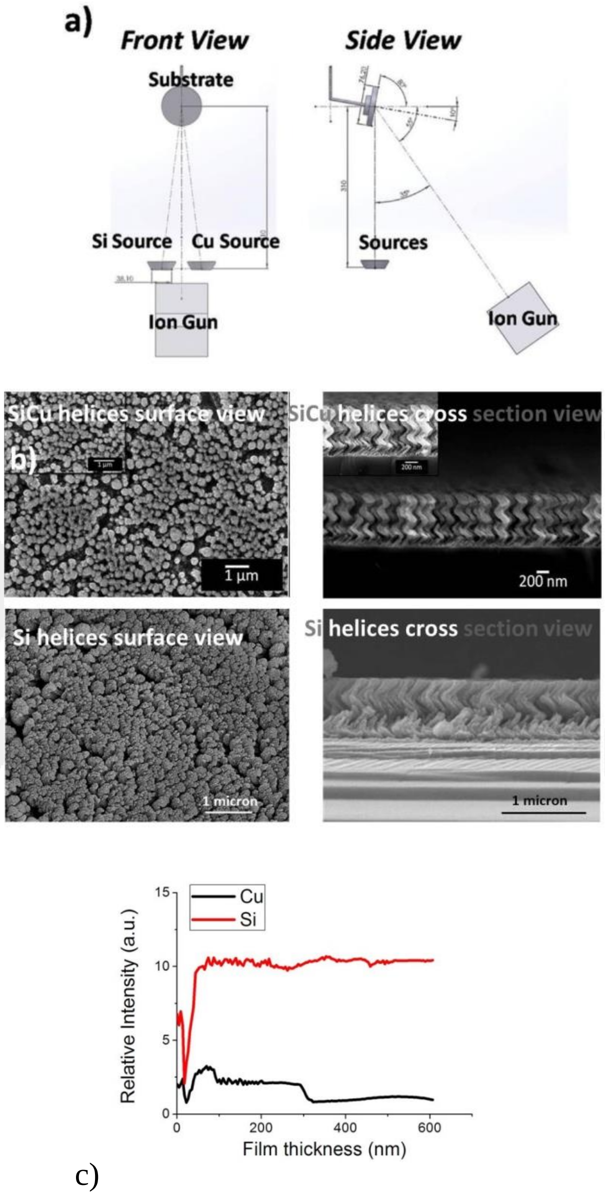


**Figure 4. 16 :** a) Experimental setup used in this study, b) SEM micrographs (of the surface and the cross section views) of the compositionally graded Si-Cu and pure Si helices containing films, c)GDOES result of the SiCu helices containing film.

The interspaces among the helices vary in size from 200 to 600 nm and the width of the helices along the height changes from 160 to 520 nm (Fig. 1b). This change from the bottom to the top of the film can be explained by the “broadening effect” and the different atomic mobilities of Cu and Si atoms [178].

The XRD results (Fig. 4.17.) show that the coating deposited on the glass substrate contains amorphous and/or nanosized particles, as seen by the sharp slope in the low diffraction angle ($2\theta < 20^0$). In earlier work, the $Li^+$ insertion/extraction mechanisms have been analyzed by in-situ XRD, SEM, and high resolution transmission electron microscopy (HR-TEM) [49,50,54,155]. The analysis results show that the lithiation mechanism of the crystalline and amorphous Si particles is different, depending on the cell potential. Upon $Li^+$ insertion, the crystal structure of the Si particles is destroyed and converted into an amorphous metastable LieSi structure according to the "solid state amorphisation theory", without formation of any intermediate phase [50,54]. This amorphous lithiated Si phase prevails up to 0.03 V, and a new crystalline compound ($Li_{15}Si_4$) forms when the cell potential decreases to values < 0.03 V. Furthermore, during $Li^+$ extraction, crystalline $Li_{15}Si_4$ is converted into both amorphous and crystalline particles, where an internal trapping of $Li^+$ ion occurs, resulting in a decreased specific capacity. On the other hand, $Li^+$ insertion into an amorphous Si anode forms an amorphous lithiated Si product, which is converted into $Li_{15}Si_4$ at a voltage lower than 0.03 V. Given that any lattice expansion could be adequately prevented by eliminating the formation of the two phases, using amorphous Si particles is more advantageous. The $Li^+$ diffusion paths developed in the amorphous thin film lead to higher electrochemical performance. To restrict recrystallization of LieSi particles and prevent over-expansion of the electrode, the lower cut-off voltage in this work was chosen to be 0.2 V.

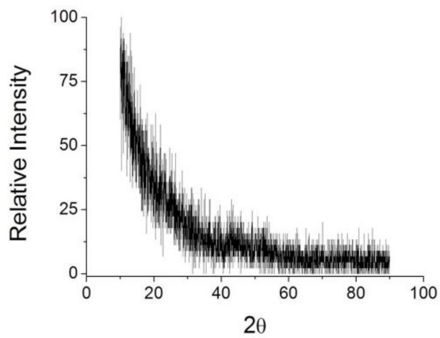


**Figure 4. 17 :** XRD analysis results of the compositionally graded Si-Cu helical coating.

The galvanostatic test shows that pure Si film with helices fails after 30$^{th}$ cycles but the graded-helix anode achieves 100th cycles with success (Fig. 4.18.a). The fact that samples do not fail in the first cycle (as in case of the bulk Si) proves the advantages of the helices morphology and ion assisted deposition. However, the morphological improvement is not enough. Therefore, we need to design compositionally graded electrode to produce an anode material with good cycleability. Different than the pure Si film, the graded electrode delivers 3331 mAh $g^{-1}$ as the first-cycle discharge ca- pacity with 54% coulombic efficiency In the next cycle, the capacity decreased to 1268 mAh $g^{-1}$, and 97% of this capacity was retained after the $100^{th}$ cycle (Fig. 4.18.c). The areal capacity of the same electrode is also given in Fig. 4.18.b. The result is found to be reasonable compared to Yue et al.'s work where they have fabricated germanium nano-island coated 3D hexagonal bottle-like Si nanorod arrays [163] and have got 0.12-0.13 mAh $cm^{-2}$ which is not stable in 100 cycles. In our case we have found a value close to 0.1 mAh $cm^{-2}$ as areal capacity which is stable around 100 cycles. To get more detailed information about the lithiation mechanism of the electrode the capacity-voltage curvatures of the sample for $1^{st}$, $2^{nd}$, $5^{th}$, $60^{th}$ and $100^{th}$ cycles are analyzed. Fig. 4.18.c reveals that the lithiation reaction of the compositionally graded helices-containing thin film is different in the first cycle (due to SEI formation starting around 1.5 V) then becomes constant. Moreover, some similarities in curvature shape are noticed with that of the Si thin film (which was also reported in the literature) [30]. This suggests that during $Li^+$ insertion, Si particles act as active centers and react with $Li^+$ to form $Li_xSi$ alloys. As no particular plateau exists for the lithiation of Cu atoms, Cu atoms are believed to form an inert, ductile, conductive matrix preventing electrochemical agglomeration and electronic isolation of $Li_xSi$ particles in cycling. This fact is expected to make an additional improvement in the reversible cycling behavior of this anode. Indeed, it is believed that SEI formation is not the only reason for the low coulombic efficiency of the electrode in the first cycle, possible morphological changes in the electrode and Li+ trapping in the film might also explain the change in the initial cycles (seen in Fig. 5.18). The high coulombic efficiency after the $1^{st}$ cycle indicates the formation of a stable interface between the electrode and the electrolyte (a stable SEI layer) after the $1^{st}$ cycle. The existence of the FEC additive in the electrolyte is believed to induce the stable SEI formation which holds the structure together by a glue effect [204].

The high and stable capacity and coulombic efficiency achieved after the $1^{st}$ cycle prove that no further delamination or peeling off of the film occurs in cycling. In the compositionally graded helix- containing film, Cu being more ductile and electrical conductive than Si increases the adhesion of the film to the Cu current collector, and decreases the ohmic resistance of the electrode. By tuning the Cu/Si atomic distribution along the helices, we benefit from the advantages of the Cu atoms without loss in the capacity delivered by the electrode.

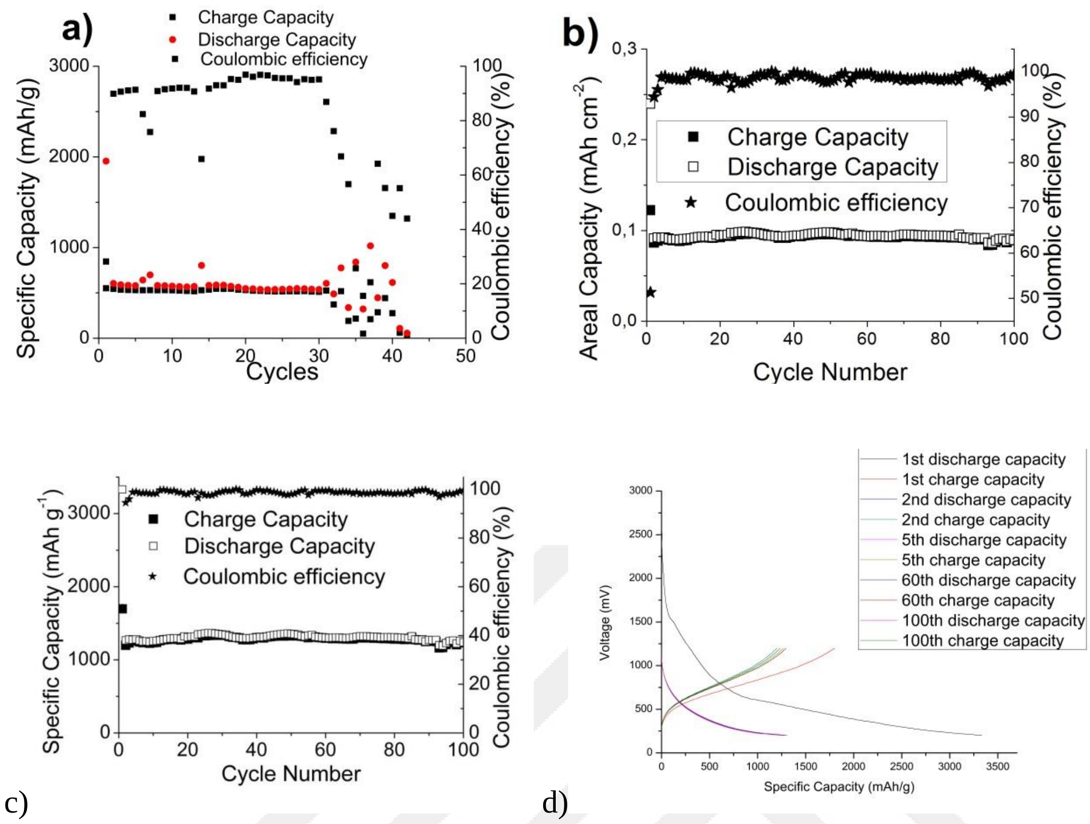


**Figure 4. 18 :** a) Specific capacity vs.cycle number of the Si film, b) Areal capacity versus cycle number of the graded film, c) Specific capacity vs. cycle number of the graded film d) Specific capacity vs. voltage curvature of the graded film as anode in half cell.

The CV curves in Fig. 4.19. demonstrate that the graded-helix-film anode has a sharp peak (0.2 V) and a very smooth bump (0.4 V) in the cathodic region. Plus, it has broad (0.35 and 0.5 V) and a smooth (>0.9 V) anodic peaks. The cathodic peaks are attributed to the lithiation of amorphous and crystalline Si particles. The anodic peaks are related to the recovery of Si from the lithiated Si particles. The decrease in the broad peak (>0.9 V) with cycling could be attributed to the oxidation of electrolyte on the electrode, which becomes less pronounced after the first cycle. On closer scrutiny of the CV curves, the peak positions were noted as being the same as that of a pure Si anode. This finding justifies the conclusion that Cu atoms in the coating represent electron conduction pathways and are inactive versus $Li^+$. The decrease in CV peak intensities upon cycling might be related to the SEI formation or morphological changes in the electrode.

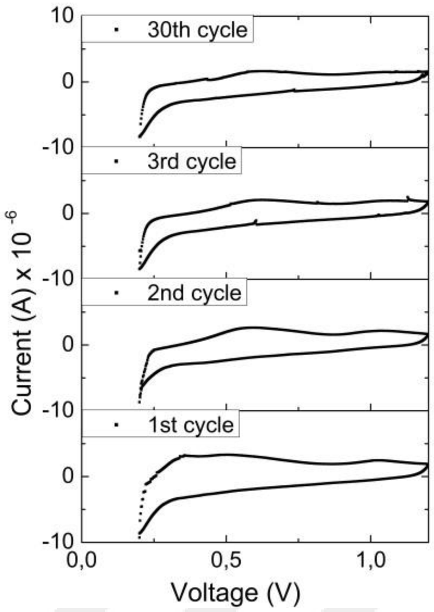


**Figure 4. 19 :** 1st, 2nd, 3rd and 30th cycles CV curves of the graded-helix-film.

The EIS data of this work is modeled by using the equivalent circuit proposed by Cui et al. [33]. Because Fig. 4.17.b reveals that the compositionally graded SiCu structured films have the similar morphological characteristics of a thin film which has mixed ionic/ electronic conductor with a large surface area and pores that can be partially filled by the liquid electrolyte. Cui et al. have explained that for such a structured thin film, nanostructures (helices in our case) that have a direct contact with the current collector, would be covered by SEI either they have direct contact with the electrolyte or with other nano structures (helices) [197]. Thus, charge transfer resistance or solid state diffusion is usually limiting the kinetics of charge/discharge reactions. Therefore, we believe that the model that is given in Fig. 4.20.c is the simplest and reasonable model that appropriately fits our experimental data. The fact that Fig. 4.20.a and b reveal the experimental and the modelling data are well-matched justify the availability of our model. The EIS data are explained based on the equivalent circuit model given in Fig. 4.20.c, where $R_s$ is the uncompensated ohmic resistance, $R_f$ is the surface resistance of the electrode, CPE is the constant phase element of the coatings with the electrolyte interface, and W is the Warburg element, which describes the solid-state diffusion inside the coatings. The constant phase element (CPE) is used instead of capacitance because the film is not continuous and the sizes of the particles vary. Note that the CPE is not only the double layer capacitance at the interface but also the lithium intercalation capacitance in the active material of the particle. The fitting values of $R_s$, $R_f$, CPE, and W are given in Table 4.2.

At high frequencies (around 10 kHz) the Nyquist plots (spectra) for the pristine anodes display low uncompensated resistance values. As we discharge the electrode, more stress is induced in the film (more Si reacts with Li). Therefore, the electrode expands. This expansion might cause some contact loss between the particle and the current collector, which explains the reason of the increase in $R_s$ values when the state of charges changes from 1.2 to 0.2 V. Given that 10 kHz is a low frequency to produce any inductive distortion in the spectra, the resistance seen in Fig. 5a around 10 kHz reflects pure resistive behavior ($Z_{im}$ close to 0). After 30 cycles, the electrode still has a very low $R_s$ value. This finding demonstrates that the array of compositionally graded Si-Cu helices prevents crack formation or delamination, enabling low resistance and stable ionic conductivity in the electrode.

At lower frequencies (10 kHz-10 Hz), the effect of the surface resistance in parallel with the capacitance is manifested as depressed semi-circles in all cases (see Fig. 4.20.a-b). The SEI formation and the inherent electron transfer resistance of Si contribute to the surface resistance. The $R_f$ can be analyzed by considering its variations at three states of charge (SOCs) in the same cycle (1.2, 0.6, and 0.2 V) or at fixed states of charge for different cycles. The results in Fig. 4.20.a suggest that SEI forms on the electrode surface during the first discharge reaction at 1.2 V, as seen by the high $R_f$ at that potential. Then, by decreasing the potential (increasing SOC) the $R_f$ value is decreased, suggesting that more $Li^+$ ions introduced into the electrode causes morphological changes. The changes are believed to increase the surface area, and thus, the amount of current passing through the active material. In turn, the charge transfer resistance is decreased. At the same SOC for different cycles, a very small increase in charge transfer resistance is noted after the 1$^{st}$ cycle. This proves that the electrode has a stable charge transfer resistance after the SEI forms. Note that the pristine and 30-cycle samples show a capacitance effect since the CPE-P values are always higher than 0.5 (Table 4.2).

At lower frequencies (below 10 Hz), an upward slope, the so-called Warburg impedance tail, is observed. The Warburg tail accounts for diffusion limitations in the electrode, which include diffusion through the electrolyte, the electrode surface layers, and the active particles. The slope seen in Fig. 4.20.a proves that the pristine sample at 1.2 V has difficult $Li^+$ diffusion due to SEI formation; following the morphological changes, the $Li^+$ diffusion becomes easier since the slope is closer to $45^0$.

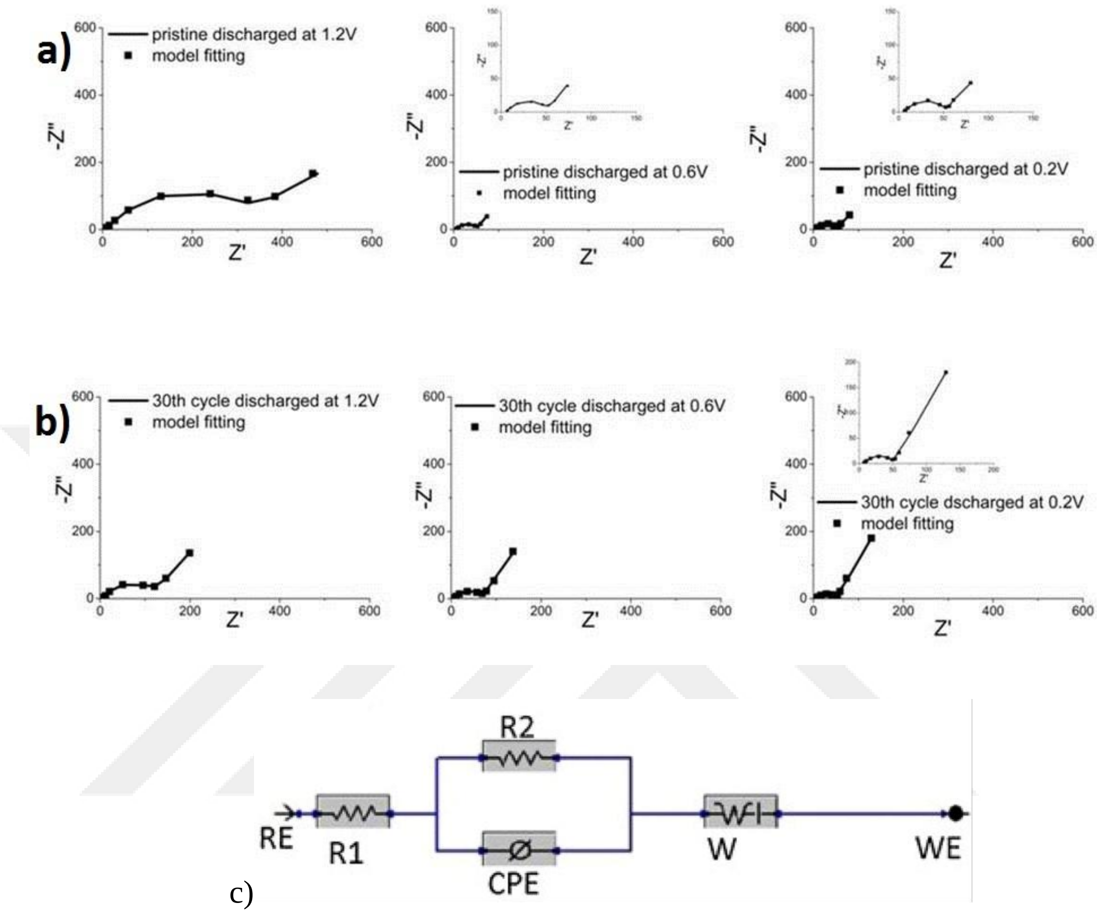


**Figure 4. 20 :** EIS test results for the a) pristine, and b) 30-cycle anode samples at 1.2, 0.6, and 0.2 V. c) Equivalent circuit model used for the EIS data.

**Table 4. 2 :** EIS test result of the graded-helix-film anode.

| | | $R_s(\Omega)$ | $R_F(\Omega)$ | CPE | W-p(S*s$^{1/2}$) |
|---|---|---|---|---|---|
| Pristine | 1.2 V | 1.084 | 298.9 | 0.71195 | 0.26211 |
| | 0.6 V | 5.403 | 39.65 | 0.74185 | 0.33206 |
| | 0.2 V | 5.909 | 34.59 | 0.72513 | 0.33381 |
| 30$^{th}$ cycle | 1.2 V | 4.505 | 73.51 | 0.89624 | 0.35818 |
| | 0.6 V | 6.189 | 54.58 | 0.75301 | 0.35778 |
| | 0.2 V | 6.664 | 43.86 | 0.68023 | 0.39081 |

The rate test results show (Fig. 4.21.) that increasing the cycle rate decreases the amount of capacity delivered by the anode, as expected. The electrode delivers 815 mAh $g^{-1}$ when cycled at 400 mA $g^{-1}$, then it retains the same capacity that it delivers after the 10th cycle when the initial rate (100 mA $g^{-1}$) is applied to the anode (after being tested at 200, 300, and 400 mA $g^{-1}$ rates). The irreversible capacity in the initial cycle could be explained by the formation of an SEI layer on the electrode, and the high capacity retention of the electrode after being cycled at different rates could be related to improved electrical and mechanical properties. The presence of more Cu atoms near the substrate compared with the film surface could be the main reason for this remarkable performance (Fig. 4.21.).

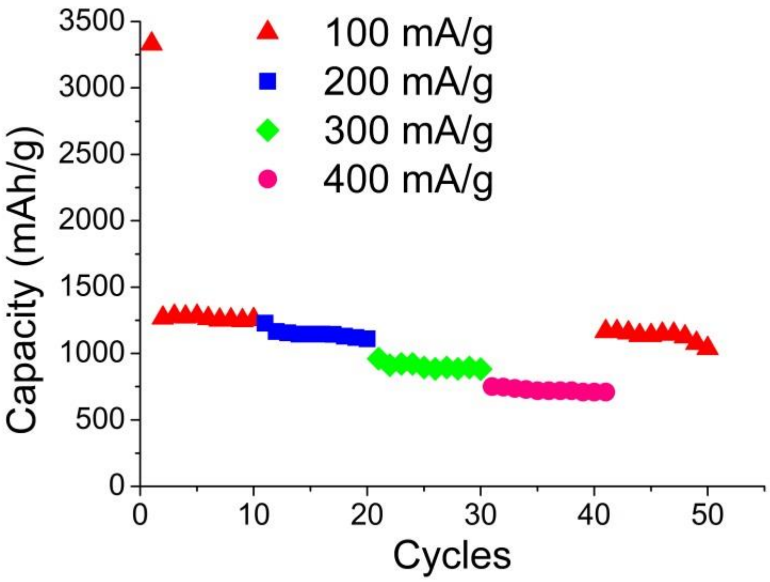


**Figure 4. 21 :** Rate test results of the graded helices containing thin film anode when cycled at 100, 200, 300, and 400 mA $g^{-1}$.

The ex-situ SEM micrographs after 3rd, 30th and 100th cycles indicate that no delamination/peel-off of the film occurs in the sample (Fig. 4.22.a-c). The particle sizes change with cycling following the stress induced by lithiation of Si particles.

The advantages of ion assisted deposition and functionally graded materials are acknowledged in literature. The originality of this work lies on the adaptation of ion assisted deposition technique to glancing angle deposition method and using compositionally-graded helices as anode material for lithium ion batteries.

The ion assisted deposition technique leads formation of dense, highly adherent film. The glancing angle deposition results in free spaces among well-aligned, ordered helices that have high surface area. By changing the composition along the helices, the functionally graded sculptured electrode has been produced. Herein, the mechanical integrity of the film is improved thank to the structured morphology of the electrode and the compositionally graded structure which (the change in Cu content along the helices) diverts the propagation of the stress while improving the adhesion of the film. Plus, the homogeneously distributed porosity in the film increases the tolerance of the electrode against volumetric changes. In addition, the amorphous and nano-sized particles improve the reversibility of the lithiation reaction. Moreover, the formation of the stable SEI layer on the electrode after the first discharge reaction stabilizes the electrode surface reactions with the electrolyte and holds the electrode particles together like a “glue,” resulting a high efficiency in cycling.

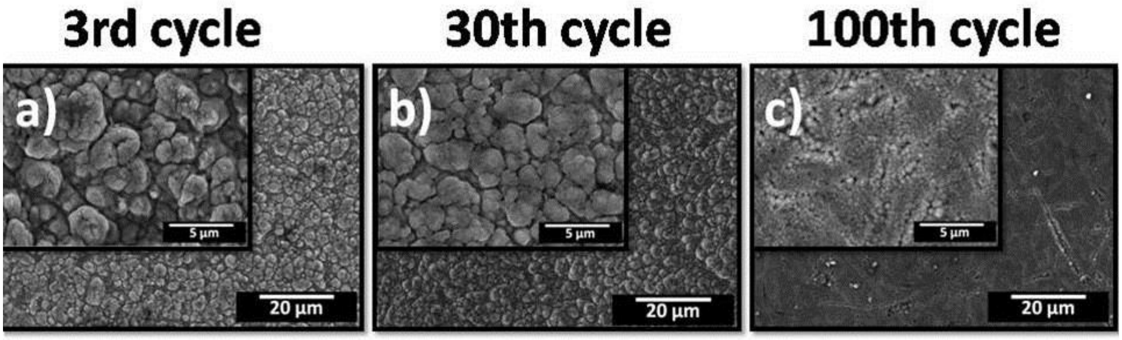


**Figure 4. 22 :** Ex-situ SEM images of the graded helices containing thin film anode after a) 3rd, b) 30th, and c) 100th cycle.

**4.3.4. Conclusions**

We have fabricated Si-Cu compositionally-graded helical arrays by an ion-assisted glancing angle electron beam evaporation method. Effective stress relaxation is achieved due to the helical morphologies and functionally graded structure of the electrode. The outcomes of our study are summarized below:

- A stable capacity 1250 mAh $g^{-1}$ with 97% retention has been achieved in between $2^{nd}$ and $100^{th}$ cycle.

- The helical shaped compositionally-graded film is the result of the synergy from the improved process design and the material selection: The presence of amorphous and/or nano-sized particles, homogeneously distributed interspaces in the structured film, new electron conductive pathway (due to Cu atoms), the improved adhesion of the film due to the compositionally graded structure (rich in the electrode/substrate interface, poor in the electrode/electrolyte interface) and the ion-assisted deposition process.

- No delamination or peel-off of the film from the substrate was noted after 100 cycles. This behavior could be due to the ion assistance during the first 5 min of evaporation, the high Cu presence at the bottom of the electrode, and interspaces among the helices representing free spaces to accommodate volumetric changes.

- Copper being more ductile and electrically conductive than Si plays a crucial role in holding the electrode together and minimizing overall capacity loss in cycling. Tuning the Cu/Si atomic distribution along the helices achieves the benefit from the Cu atoms without loss of capacity.

- The proposed EIS model fits well with the experimental data. The stable and low uncompensated resistance values are consistent with the above-mentioned advantages of the Cu atoms on the electrode performance. Plus, changes in the solid-state diffusion rate of $Li^+$ ions account for the morphological changes in the electrode during cycling.

# 5. CONCLUSIONS AND RECOMMENDATIONS

## 5.1. Conclusions

Nowadays, making lithium-ion batteries with long cycle life and efficiency becomes a hot topic. Each week 50 to 200 new papers are publishing on the topic of lithium-ion batteries. Although highly intensive researches propose new solutions to improve the performance of the lithium ion battery, no perfect method has yet to be found to overcome issues related to stress induced in the electrode and its mechanical degradation.

In this study, design criteria for high electrochemical performance anode material have been highlighted. The material selection and process design should be carefully done to improve the capacity and the cycle life of the negative electrode. In this concept, Ag and Cu are added to Si to promote the electrical conductivity of the film. Then magnetron sputtering and glancing angle electron beam evaporation are used to engineer well adherent Si based films. In this dissertation first in literature ion assistance was adopted to glancing angle electron beam evaporation process to fabricate compositionally graded well aligned helix containing film. Plus, HPPMS was used to sputter Si without arcing when producing functionally graded SiCu film by magnetron sputtering process.

Knowing that advantages and applications of lithium ion batteries have been vastly acknowledged in literature, the originality of this disertation lies on the seleection of the material and process design to engineer Si based negative electrodes for LIBs.

In Chapter 4.1. 20%at. Ag containing Si composite film was deposited by magnetron sputtering method. As Ag atoms are also electrochemically active versus Li, the lithiation reactions of SiAg film has been optimized by using different cut-off voltages in galvanostatic test. The galvanostatic test performance of the electrode when cycled between 0.2 – 1.2 V has been found to be outstanding: the electrode delivers 1825 mAh $g^{-1}$ at the first discharge reaction and retains 96% of this value after $60^{th}$ cycles when cycled with C/12 rate. Besides, the electrode still continue in cycling even at 2C rate [205]. However, the fact that Ag is a heavy and expensive metal, an alternative electrochemically inactive element Cu is used in the second and third chapter.

In Chapter 4.2, we have proposed to engineer functionally graded SiCu film with 2.4 μm thickness by magnetron sputtering method. Herein Cu has been chosen due its high conductivity, ductility and high solubility in Si. To be able to deposit defect-free Si film, HPPMS process has been used during experiments [206].The results show that the electrode delivers 2073 mAh $g^{-1}$ in the first cycle, then after some fluctutiation it stabilizes around 1500 mAh $g^{-1}$ during 90 cycles when cycled at 100 mA $g^{-1}$ rate vs $Li/Li^+$. The rate capability of this electrode is also outstanding since it delivers roughly 700 mAh $g^{-1}$ even at 500 mA $g^{-1}$ rate.

In Chapter 4.3, morphological, structural and electrochemical properties of the compositionally-graded electrode have been given [207]. The results show that the electrode delivers 3331 mAh $g^{-1}$ in the first cycle. The galvanostatic test exhibits that the capacity of the electrode decreases after the 1$^{st}$ cycle to 1268 mAh $g^{-1}$ and 97% of this capacity is retained from 2$^{nd}$ to 100$^{th}$ cycle when cycled at 100 mA $g^{-1}$ rate vs $Li/Li^+$. The rate test also exhibits that the rate capability of this graded electrode is also remarkable since it delivers 815 mAh $g^{-1}$ at 400 mA $g^{-1}$ rate.

### 5.2. Recommendations

This dissertation justifies that physical vapor deposition method could be used in the production of anode materials for next generation lithium ion batteries. Beside the production process, the composition, the structure and the morphology of the film as well as the galvanostatic test conditions are found to affect the electrochemical performances of the electrode.

We believe that by designing functionally graded electrodes could open a new gateway for future studies. Herein, results of films produced by magnetron sputtering are found to be more prominent since it enables one to fabricate thicker Si based films with higher electrochemical performance.

Therefore, future researchers are encouraged (1) to study more advanced techniques such as X-ray Absorption Spectroscopy (XAS) or TEM to get information about the homogeneity of the microstructure and the morphology of the electrode. (2) to examine the morphological changes in the electrode by in-situ techniques, which will give the opportunity to understand the mechanically weak points of the graded electrodes. (3) to model the stress dissipation in electrode, so as to quantify the advantages of using compositionally graded SiCu electrode in lithium ion battery, and (4) to improve the stress dissipation behavior and the mechanical tolerance of the electrode, different materials (like Al, C, etc) could be used to make varieties of functionally graded electrodes.

## REFERENCES


[1] **Energy in the 21st century.** Date retrieved 27.11.2016, <*http://pubs.acs.org/subscribe/archive/ci/31/i01/html/01chen.html*>.

[2] **Ford's science-based $CO_2$ Targets.** Date retrieved 7.1.2015, <*http://corporate.ford.com/microsites/sustainability-report-2011-12/environment-climate-strategy-targets.html*>.

[3] **Vergis, S.**, **Turrentine, T. S.** (2014). Plug-In Electric Vehicles:A Case Study of Seven Markets (Report No: UCD-ITS-RR-14-17). California, USA: Institue of Transportation Studies Research Report.

[4] **Tan, Q., Wang, M.** (2014). The Cultivation of Electric Vehicles Market in China: Dilemma and Solution. *Sustainability*, ***6***, 5493-5511.

[5] **Shanan, Z.** (2014). 15 Electrical cars hitting the market in 2015. *evobsession.com*. Retrieved October 3rd 2015, from <http://evobsession.com/new-electric-cars-market-2015-list/>

[6] **Url-1** <*http://www.eia.gov/*>, date retrieved 3.11.2015.

[7] **Li, H., Wang, Z.** (2009). Research On Advanced Materials For Li-Ion Batteries. *Adv. Mater.*, *21*, 4593-4607.

[8] **Manthiram, A.** (2001). Materials Challenges and Opportunities of Lithium Ion Batteries. *J. Phys. Chem. Lett*., *2*, 176-184.

[9] **Url-2** <*http://batteryuniversity.com/learn/article/global_battery_markets*>, date retrieved 5.1.2015.

[10] **Whittingham, M.S.** (2008). Materials Challenges Facing Electrical Energy Storage. *MRS Bullet.*, *33*, 411-419.

[11] **Besenhard, J.O., Schöllhorn, R.** (1977). Chromium Oxides as Cathodes for Secondary High Energy Density Lithium Batteries. *J.Electrochem. Soc.*, *124*, 968-971.

[12] **Basu, S.** (1982). *U.S. Patent No. 4423125A.* NewJersey, NY: U.S. Patent and Trademark Office.

[13] **Yazami, R., Touzain, P.** (1983). A Reversible Graphite-Lithium Negative Electrode for Electrochemical Generators. *J. Power Sources*, *9*, 365-371.

[14] **Mizushima, K., Jones, P.C.** (1981). $Li_xCoO_2$ ($0<x\leqslant1$): A new cathode material for batteries of high energy density. *Solid State Ionics*, *3-4*, 171-174.

[15] **Yoshino, A.**, (2012). The birth of Lithium-Ion Battery. *Angew. Chem. Int. Ed.*, *51*, 2-5.

[16] **Pahdi, A.K., Nanjundaswamy, K.S., Goodenough, J.B.** (1997*).* Phospho-olivines as positive- electrode materials for rechargeable lithium batteries*. J. Electrochem. Soc., 144,* 1188-1194.

[17] **Thackeray, M.** (2002). Lithium-Ion Batteries: An Unexpected Conductor. *Nature Mater., 1***,** 81-82.

[18] **Spotnitz, R.** (2003). Simulation Of Capacity Fade In Lithium-Ion Batteries. *J. Power Sources, 113*, 72-80.

[19] **Cui, Y., Han, S.** (2009).*U.S. Patent*, No: *US8450012 B2*. California. U.S. Patent and Trademark Office.

[20] **Dimov, N., Xia, Y., Yoshio, M.** (2007). Practical silicon-based composite anodes for lithium-ion batteries: Fundamental and technological features. *J. Power Sources, 171*, 886-893.

[21] **Choi, N.S., Chen, Z., Freunberger, S.A., Ki, X., Sun, Y.-K., Amine, K., Yushin, G., Nazar, L.F., Cho, J., Bruce, P.G.** (2012). Challenges facing lithium batteries and electrical double-layer capacitors. *Angew. Chem. Int. Ed., 51*, 9994–10024.

[22] **Arora, P., Zhang, Z.** (2015). Battery separators. *Chem. Rev., 104*, 4419–4462.

[23] **Xiao,W., Zhao, L., Gong, Y., Liu, J., Yan, C.** (2015). Preparation and performance of poly (vinyl alcohol) porous separator for lithium-ion batteries. *J. Membrane Sci., 487*, 221–228

[24] **Wakihara, M.** (2001). Recent developments in lithium ion batteries. *Mater. Sci. Eng., R., 33*, 109-134.

[25] **Chen, L., Wang, K., Xie, X., Xie, J.** (2007). Effect of vinylene carbonate (VC) as electrolyte additive on electrochemical performance of Si film anode for lithium ion batteries. *J. Power Sources, 174*, 538-543.

[26] **Choi, N.S., Yew, K.H.** (2006). Effect of fluoroethylene carbonate additive on interfacial properties of silicon thin film electrode. *J. Power Sources, 161*, 1254-1259.

[27] **Arakawa, M., Yamaki, J.-I.** (1987). The cathodic decomposition of propylene carbonate in lithium batteries. *J. Electroanal. Chem.,* ***219,*** 273-280.

[28] **Liu, H., Song, C., Zhang, L., Zhang, J. Wang, H., Wilkinson, D.P.** (2006). A review of anode catalysis in the direct methanol fuel cell**.** *J. Power Sources, 162*, 1379-1394.

[29] **Arico, A.S., Bruce, P., Scrosati, B., Tarascon, J.-M., Schalkwijk, W.v.** (2005). Nanostructured materials for advanced energy conversion and storage devices. *Nature Mater., 4*, 366-377.

[30] **Zhou, L., Zhao, D., Lou, X.** (2012). $LiNi_{0.5}Mn_{1.5}O_4$ Hollow Structures as High-Performance Cathodes for Lithium-Ion Batteries. *Angewandte Chem., 124*, 243-254.

[31] **Arrebola, J., Caballero, A., Hernan, L., Morales, J., Castellon, E.R., Barrado, J.R.R.** (2007). Effects of Coating with Gold on the Performance of Nanosized $LiNi_{0.5}Mn_{1.5}O_4$ for Lithium Batteries. *J. Electrochem. Soc., 154*, A178-184.

[32] **Melot, B. C., Tarascon, J. M.** (2013). Design and Preparation of Materials for Advanced Electrochemical Storage. *Accounts of Chemical Research, 46*, 1226-1238.

[33] **Fergus, J. W.** (2010). Recent developments in cathode materials for lithium ion batteries. *J. Power Sources*, *195,* 939-954.

[34] **Fischer, C.A.J., Islam, M.S.** (2014). Lithium and sodium battery cathode materials: computational insights into voltage, diffusion and nanostructural properties. *Chem. Soc. Rev., **43**,* 185-204.

[35] **Ji, G., Ma, Y., Lee J.Y.** (2011). Mitigating the initial capacity loss (ICL) problem in high capacity lithium ion battery anode materials. *J. Mater. Chem., 21,* 9819-9824.

[36] **Zhang, D., Harran, B.S., Durairajan, White, R.E., Podrazhansky, Y., Popov, B.N.** (2000). Studies on capacity fade of lithium ion batteries, *J. Power Sources, 91*, 122-129.

[37] **Tukamoto, H., West, A.R.** (1997). Electronic conductivity of $LiCoO_2$ and its enhancement by magnesium doping. *J. Electrochem. Soc., **144**,* 3164-3168.

[38] **Eom, K.S., Jung, J., Lee, J.T., Lair,V., Joshi, T., Lee, S.W., Lin, Z., Fuller, T.F.** (2015). Improved stability of nano-Sn electrode with high-quality nano-SEI formation for lithium ion battery. *Nano Energy*, ***12**,* 314-321.

[39] **Candelaria, S.L., Shao, Y. Zhou, W., Li, X., Xia,J., Zhang, J.-G., Wang, Y., Liu, J., Li, J., Cao, G.** (2012). Nanostructured carbon for energy storage and conversion. *Nano Energy, 2,* 195-220.

[40] **Wachtler, M., Winter, M.** (2002). Anodic materials for rechargeable Li-batteries. *J. Power Sources*, **105**, 151-160.

[41] **Wen, C. J., Huggins, R. A.** (1981). Chemical diffusion in intermediate phases in the lithium-silicon system. *J. Solid State Chem., 37,* 271-278.

[42] **Van Der Marcel, C., Vinke, G. J. B.** (1985). The phase diagram of the system lithium-silicon. *Solid State Commun., 54,* 917-919.

[43] **Su, X., Wu, Q., Li, J., Xiao, X., Lott, A., Lu, W., Sheldon, B.W., Wu, J.** (2014). Silicon based nanomaterials for lithium-ion batteries: a review. *Adv. Energy Mater., 4,* 1-23.

[44] **Yoshio, M., Kugino, S., Dimov, N.** (2006). Electrochemical behaviors of silicon based anode material. *J.Power Sources, 153***,** 375-379.

[45] **Hovington, P., Dontigny M., Guerfi, A., Trottier, J., Lagace, M., Mauger, A., Julien, C.M., Zaghib, K.** (2014). In situ Scanning electron microscope study and microstructural evolution of nano silicon anode for high energy Li-ion batteries. *J. Power Sources, 248,* 457-464.

[46] **Boukamp, B.A., Lesh, G.C., Huggins, R.A.** (1981). All-solid lithium electrodes with mixed-conductor matrix. *J. Electrochem. Soc***.,** *128,* 725-729.

[47] **Tirado, J.L.** (2003). Inorganic, materials for the negative electrode of lithium-ion batteries: state-of-the-art and future prospects. *Mater. Sci. Eng. R Rep., 40,* 103-136;

[48] **Van der Marcel, C. , Vinke, G.J.B., Van der Lugt, W.** (1985). The phase diagram of the system lithium-silicon. *Solid State Commun. 54,* 917-919.

[49] **Li, H., Huang, X., Chen, L., Zhou, G., Zhang, Z., Yu, D., Mo, Y.J., Pei, N.** (2000). The crystal structural evolution of nano-Si anode caused by lithium insertion and extraction at room temperature. *Solid State Ionics, 135,* 181-191.

[50] **Limthongkul, P., Yang, Y.I.** (2003). Electrochemically-driven solid-state amorphization in lithium-metal anodes. *J.Power Sources, 119-121,* 604-609

[51] **Li, J., Dahn, J.R.** (2007). An situ X-ray diffraction study of the reaction of Li with crystalline Si. *J. Electrochem. Soc., 154,* A156-A161.

[52] **Obravac, M.N., Christensen, L.** (2004). Structural changes in silicon anodes during lithium insertion/extraction. *Electrochem. Solid State Lett., 7,* A93-A96.

[53] **Limthongkul, P., Yang, Y. I.** (2003). Electrochemically-driven solid-state amorphization in lithium-silicon alloys and implications for lithium storage .*Acta Mater., 51,* 1103-1113.

[54] **Hatchard, T.D., Dahn, J.R.** (2004). In situ XRD and electrochemical study of the reaction of lithium with amorphous silicon. *J. Electrochem. Soc., 151,* A838-A842

[55] **Abel, P.R., Chockla, A.M., Lin, Y.-M., Holmberg, V.C., Harris, J.T., Korgel, B.A., Heller, A., Mullins, C.B.** (2013). Nanostructured $Si_{(1-x)}Ge_x$ for tunable thin film lithium-ion battery anodes. *ACS Nano.,* ***7,*** 2249-2257.

[56] **Maranchi, J.P., Hepp, A.F., Kumta, P.N.** (2003). High capacity, reversible silicon thin-film anodes for lithium-ion batteries. *Electrochem. Solid State Lett., 6 (9),* A198-201.

[57] **Datta, M.K., Kumta, P.N.** (2009). In situ electrochemical synthesis of lithiated silicon–carbon based composites anode materials for lithium ion batteries. *J. Power Sources., 194 (2),* 1043-1052

[58] **Peled, E., Golodnitsky, D., Ardel, G., Eshkenazy V.** (1995). The SEI model-application to lithium-polymer electrolyte batteries. *Electrochem. Acta,* ***40***, 2197-2204.

[59] **Yao, Y., Liu, N., McDowell, M.T., Pasta M., Cui, Y.** (2012). Improving the cycling stability of silicon nanowire anodes with conducting polymer coatings. *Energy Environ. Sci.,5*, 7927-7930.

[60] **Gao, J. Zhang, H.P., Fu, L.J., Zhang, T., Wu, Y.P., Takamura, T., Wu, H.Q., Holze, R.** (2007). Suppressing propylene carbonate decomposition by coating graphiteelectrode foil with silver. *Electrochimica Acta., 52* (17), 5417-5421.

[61] **Shafiei, M., Alpas, A.T.** (2011). Electrochemical performance of a tin-coated carbon fibre electrode for rechargeable lithium-ion batteries. *J. Power Sources, 196* (18), 7771-7778.

[62] **Xiao, X., Lu, P., Ahn, D.** (2011). Ultrathin multifunctional oxide coatings for lithium ion batteries. *Adv. Mater., 23* (34), 3911-3915.

[63] **Abraham, D. P., Furczon, M. M., Kang, S.-H., Dees, D.W., Jansen, A.N.** (2008). Effect of electrolyte composition on initial cycling and impedance characteristics of lithium-ion cells. *J. Power Sources, 180* (1), 612–620.

[64] **Ryu, Y.G., Lee, S., Mah S., Lee, D.J., Kwon, K., Hwang, S., Doo, S.** (2008). Electrochemical behaviors of silicon electrode in lithium salt solution containing alkoxy silane additives. *J. Electrochem. Soc., 155,* A583–A589.

[65] **Song, S.W., Baek, S.W.** (2009). Silane-derived SEI stabilization on thin-film electrodes of nanocrystalline Si for lithium batteries. *Electrochem. Solid-State Lett., 12* (2), A23–A27.

[66] **Yen, Y.C., Chao, S.C., Wu, H.-C., Wu, N.-L.** (2009). Study on solid–electrolyte-interphase of Si and C-coated Si electrodes in lithium cells**.** *J. Electrochem. Soc., 156,* A95–A102.

[67] **Yang, J., Winter M., Besenhard, J.O.** (1996). Small partical size multiphase Li-alloy anodes for lithium-ion batteries. *Solid State Ionics*, ***90,*** 281–287.

[68] **Gao, B., Sinha, S., Fleming, L., Zhou, O.** (2001). Alloy formation in nanostructured silicon. *Adv. Mater., 13,* 816-819.

[69] **Chan, C. K., Peng, H., Liu, G., McIwrath K., Zhang, X.F., Huggins, R.A., Cui, Y.** (2008). High-performance lithium battery anodes using silicon nanowires. *Nat. Nanotechnol., 3,* 31-35.

[70] **Chan, C. K., Ruffo, R., Hong, S.S., Cui, Y.** (2009). Surface chemistry and morphology of the solid electrolyte interphase on silicon nanowire lithium-ion batteriy anodes. *J. Power Sources., 189,* 1132-1140.

[71] **Yang, J. I. Y.-P. H. C. A. L. Y.-P. Z. B.** (2012). A chemo-elastoplastic analysis of anisotropic swelling in an $SnO_2$ nanowire under lithiation *Engi. Mater. Tech., 134,* 031013-1-031013-5.

[72] **Graetz, J., Ahn C. C., Yazami R., Fultz, B.** (2003). Highly reversible lithium storage in nanostructured silicon. *Electrochem. Solid State Lett. 6,* A194-A197.

[73] **Yu, D.P., Xing, Y.J., Hang, Q.L., Yan, H.F., Xu, J., Xi, Z.H., Feng, S.Q.** (2001). Controlled growth of oriented amorphous silicon nanowires via a solid- liquid-solid (SLS) mechanism. *Physica E, 9,*305-309.

[74] **Kolb, F.M., Hofmeister, H., Scholz, R., Zacharias, M., Gösele, U., Ma, D.D., Lee, S-T.** (2004). Analysis of silicon nanowires grown by combining SiO evaporation with the VLS mechanisim. *J. Electrochem. Soc., 151,* G472-G475.

[75] **Chang, J.B., liu, J.Z., Yan, P.X., Bai, L.F., Yan, Z.J., Yuan, X.M., Yang, Q.** (2006). Ultrafast growth of single-crystalline Si nanowires. *Mater. Lett.*, *60,* 2125-2128.

[76] **Yazami, R.** (2014). *Nanomaterials for Lithium-Ion Batteries: Fundamentals and Applications.* Boca Raton, FL.: CRC Press.

[77] **Li, J., Dozier A.K., Li Y., Yang F., Cheng Y.T**. (2011). Crack pattern formation in thin film lithium-ion battery electrodes. *J. Electrochem. Soc., 158,* A689-A694

[78] **Wen, Z., Tian F**. (2013). Cu-doped Silicon film as anode for lithium ion batteries prepared by ion-beam sputtering. *Int. J. Electrochem. Sci*., *8*, 10129-10137.

[79] **Li, H., Huang, X., Chen, L., Zhou, G., Zhang, Z., Yu, D., Mo, J.Y., Pei, N.** (2000). The crystal structural evolution of nano-Si anode caused by lithium insertion and extraction at room temperature. *Solid State Ionics*, *135*, 181-191.

[80] **Ohara, S., Suzuki, J., Sekine, K., Takamura, T.** (2004). A thin film silicon anode for Li-ion batteries having a very large specific capacity and long cycle life. *J. Power Sources*., *136*, 303-306

[81] **Cui, L. F., Ruffo, R., Chan, K.C., Peng, H., Cui, Y.** (2009). Crystalline-amorphous core-shell silicon nanowires for high capacity and high current battery electrodes. *Nano Lett.*, *9*, 491-495.

[82] **Nanda, J., Datta, M.K., Remillard, J.T., O'neill, A., Kumta, P.N.** (2009). In situ Raman microscopy during discharge of a high capacity silicon-carbon composite Li-ion battery negative electrode**.** *Electrochem. Commun*., *11*, 235-237.

[83] **Li, J.** (2012). *Understanding Degradation And Lithium Diffusion In Lithium Ion Battery Electrodes* (Doctoral Dissertation). Retrieved from http://uknowledge.uky.edu/cme_etds/12/

[84] **Gross, D., Seelig, T.** (2006). *Fracture Mechanics*. New York: Springer.

[85] **Chen, L.B., Xie, J. Y., Yu, H.C., Wang, T.H.** (2009). An amorphous Si thin film anode with high capacity and long cycling life for lithium ion batteries. *J. App. Electrochem., 39*, 1157-1162.

[86] **Song, T. Xia, J., Lee, J.-H., Lee, D.H., Kwon, M.-S., Choi, J.-M., Wu, J., Doo, S.K., Chang, H., Park, W., Zang, D.S., Kim, H., Huang, Y., Hwang, K.-C., Rogers, J.A., Paik, U.** (2010). Arrays of sealed silicon nanotubes as anodes for lithium ion batteries. *Nano Lett., 10*, 1710-1716.

[87] **Lee, K. L., Jung, J. Y., Lee, S.-W., Moon, H.-S., Park, J.-W.** (2004). Electrochemical characteristics of a-Si thin film anode for Li- ion rechargeable batteries. *J. Power Sources., 129*, 270-274.

[88] **Chen, X. L., Gerasopoulos, K. J., Guo, J., Brown, A., Wang, C., Ghodssi, R., Culver, J.N.** (2010). Virus-enabled silicon anode for lithium-ion batteries. *ACS Nano., 4*, 5366-5372.

[89] **Kim, H., Han, B.  Choo, J., Cho, J.** (2008). Three-dimensional porous silicon particles for use in high performance lithium secondary batteries. *Angew. Chem. Int. Ed., 47,* 10151-10154.

[90] **Xiao, J., Xu, W., Wang, D., Choi, D., Wang, W., Li, X., Graff, G.L. ve Liu, J., Zhang, J.-G.** (2010). Stabilization of silicon anode for Li-ion batteries. *J. Electrochem. Soc*., *157,* A1047-A1051.

[91] **Fleischauer, M.D., Topple, J.M., Dahn, J.R.** (2005). Combinatorial investigations of Si-M (M=Cr plus Ni, Fe, Mn) thin film negative electrode materials. *Electrochem. Solid State Lett., 8*, A137-A140.

[92] **Mao, O., Dahn, J.R.** (1999). Mechanically alloyed Sn-Fe(-C) powders as anode materials for Li-ion batteries. I. The $Sn_2$Fe-C system. *J. Electrochem. Soc., 146*, 405-413.

[93] **Fleischauer, M.D., Obrovac, M.N.,. McGraw, J. D, Dunlap, R. A., Topple, J. M., Dahn, J. R.** (2006). Al-M (M=Cr, Fe, Mn, Ni) Thin-film negative electrode materials. *J. Electrochem. Soc., 153,* A484-A491.

[94] **MSI Eureka Viewer** [Computer Software] Stuttgart, Germany.

[95] **Ohring, M.** (1992). *The materials science of thin films***.** London: Academic Press.

[96] **Sarkar, J. (2014).** *Sputtering Materials for VLSI and Thin Film Devices*. Tokyo: Elsevier.

[97] **Wasa, K**. (2012). *Handbook of Sputtering Deposition Technology*. Tokyo: Elsevier.

[98] **Mattox, D.M**. (2014). *Handbook of Physical Vapor Deposition Processing*. Tokyo: Elsevier.

[99] **Mahan, J.** (2000). *Physical Vapor Deposition of Thin Films.* New York, NY: Wiley.

[100] **Lee, S.-J., Lee, J.-K., Chung, S.-H., Lee, H.Y., Lee, S.-M., Baik, H.K.** (2001). Stress effect on cycle properties of the silicon thin-film anode. *J.Power Sources, 97-98,* 191-193.

[101] **He, Y., Zhao, Y.** (2011). Advanced multi-component nanostructures designed by dynamic shadowing growth. *Nanoscale 3,* 2361-2375.

[102] **Ye, D.X., Karabacak, T., Picu, R.C., Wamg, G.-C., Lu, T.-M.** (2005). Uniform Si nanostructures grown by oblique angle deposition with substrate swing rotation. *Nanotechn., 16*, 1717-1723.

[103] **Karabacak, T., Picu, C.R., Senkevich, J.J., Wang, G.-C., Lu, T.-M.** (2004). Stress reduction in tungsten films using nanostructured compliant layers.  *J. Appl. Physic., **96***, 5740-5746.

[104] **Lisfi, A.**, **Lodder, J.C.** (2001). Magnetic domains in Co thin films obliquely sputtered on a polymer substrate. *Phys. Rev. B*, ***63***, 174441-1.

[105] **Neiuwenhuizen, J.M., Haanstra, H.B.** (1966). Microfractography of thin films. *Philips Tech. Rev., **27**,* 87-91.

[106] **Tait, R. N., Smy, T., Brett, M.J.** (1993). Modeling and characterization of columnar growth in evaporated-films. *Thin Solid Films., 226* (2), 196–201.

[107] **Hawkeye, M. M, Brett, M. J.** (2007). Glancing angle deposition: Fabrication, proper- ties, and applications of micro- and nanostructured thin films. *J. Vacuum Sci. & Techn.*, A, *25* (5), 1317–1335.

[108] **Zhao, Y. P., Ye, D. X., Wang, G.C., Lu, T.M.** (2003). Designing nanostructures by glancing angle deposition. *Nanotubes And Nanowires., 5219*, 59–73.

[109] **Lichter, S., Chen. J.** (1986). Model for columnar microstructure of thin solid films. *Physical Rev. Lett., 56* (13):1396–1399.

[110] **Robbie, K., Sit, J.C., Brett, M.J.** (1998). Advanced techniques for glancing angle deposition. *J. Vac. Sci. Technol. B, 16*, 1115-1122.

[111] **Vick, D., Friedrich, L.J., Dew, S.K., Brett, M.J., Robbie, K., Seto, M., Smy, T.** (1999). Self-shadowing and surface diffusion effects in obliquely-deposited thin films. *Thin Solid Films, 339*, 88-94.

[112] **He, Y., Zhang, Z.** (2008). Embedding Ag nanoparticles into $MgF_2$ nanorod arrays. *Adv. Func. Mater., 18*, 1676-1684.

[113] **He, Y., Zhao, Y.** (2010). Mg nanostructures tailored by glancing angle deposition. *Crys. Growth&Design, 10*, 441-448.

[114] **He, Y., Fu, J., Zhang, Y., Zhao, Y., Xia, A., Cia, J.** (2007). Multilayered Si/Ni nanosprings and their magnetic properties. *Small., 3*, 153-160.

[115] **Huang, Z., Bai, F.** (2014). Wafer-scale, three-dimensional helical porous thin films deposited at a glancing angle. *Nanoscale, 6*, 9401-9409.

[116] **González-Garcia, L., González, I.-V., Monica, L.-C., Barranco, A., Gonzalez-Elipe, A.R.** (2011). Aligned $TiO_2$ nanocolumnar layers prepared by PVD-GLAD for transparent dye sensitized solar cells. *Energy Environ. Sci., 4*, 3426-3435.

[117] **Wakefield, N. G., Sorge, J. B.** (2011). Control of the principal refractive indices in biaxial metal oxide films. *J. Optical Society of America, 28*, 1830-1840.

[118] **Kwan, J. K, Sit, J. C. (2010).** The use of ion-milling to control clustering of nanostructured, columnar thin films. *Nanotechnology*, ***21***, 295301-1-6.

[119] **Macias-Montero, M., Borras, A., Saghi, Z., Espinos, J.P., Barranco, A., Cotrino, J., Gonzalez-Elipe, A.R. (2012).** Vertical and tilted Ag-NPs@ZnO nanorods by plasma-enhanced chemical vapour deposition. *Nanotechnology, 23*, 255303-1-12.

[120] **He, Y., Zhao Y. (2011).** Advanced multi-component nanostructures designed by dynamic shadowing growth. *Nanoscale*, ***3***, 2361-2375.

[121] **Url-3** *<https://web.viu.ca/dickb/Research/GLAD.html>* date retreieved 3.11.2015.

[122] **Yang, M., Kotov N. A. (2011).** Nanoscale helices from inorganic materials. J. Mater. Chem., *21*, 6775-6792.

[123] **Shi, X., Choi, I. Y. (2014).** Efficient photoelectrochemical hydrogen production from bismuth vanadate-decorated tungsten trioxide helix nanostructures. *Nature Communications, 5,* Article Number:4775.

[124] **Url-4** <*http://www.scorec.rpi.edu/nanomechanics/testing_material_behavior_at_the_nanoscale.htm*> date retrieved 3.11.2015

[125] **Kaminska, K., Brown, T.** (2003). Vacuum evaporated porous silicon photonic interference filters. *Applied Optics*, *42* (20), 4212–4219.

[126] **Steele, J. J.,Van Popta, A. C.** (2006). Nanos- tructured gradient index optical filter for high-speed humidity sensing. *Sensors and Actuators B-Chemical*, *120* (1), 213–219.

[127] **Robbie, K., Brett M.J.** (1997). Sculptured thin films and glancing angle deposition: Growth mechanics and applications. *J. Vac. Sci. Technol.* A, *15* , 1460-1465.

[128] **Wasa, K., Kitabatake M., Adachi, H.** (2014). Handbok of Thin film devices, USA: Elsevier.

[129] **Zoerb, K.A. (2007).** *Diferential sputtering yields of refractory metals by ion bombardment at normal and oblique incidences.* (Doctoral dissertation). Retrieved from http://projects-web.engr.colostate.edu/

ionstand/publications/papers/Zoerb%20Thesis.pdf.

[130] **Berg, S., Nyberg, T.** (2005). Fundamental understanding and modeling of reactive sputtering processes. *Thin Solid Films, 476*, 215-230.

[131] **Kelly, P.J., Arnell, R.D.** (2000). Magnetron sputtering:a review of recent developments and applications. *Vacuum., 56*, 159-172.

[132] **Kouznetsov, V., Macak, K., Schneider, J.M., Helmersson, U., Petrov, U.** (1999). *Surf. and Coat. Tech., 122*, 290-293.

[133] **Sarakinos, K., Alami, J., Konstantinidis, S.** (2010). High power pulsed mangetron sputtering: A review on scientific and engineering state of the art. *Surf. Coat. Techn., 204*, 1661-1684.

[134] **Bobzin, K., Bagcivan, N., Immıch, P., Bolz, S., Alami, J., Cremer R**. (2009). Advantages od nanocomposite coatings deposited by high power pulse magentron sputtering technology, *J. Mater. Process. Techn., 209*, 165-170.

[135] **Afyon, S., Krumeich, F., Mensing, C., Borgschulte, A., Nesper, R.** (2014). New high capacity cathode materials for rechargeable Li-ion batteries:vanadates-borate glasses. *Nat. Chem*., *19*, 1079-1083.

[136] **Sharma, S.K., Kim, M.-S., Kim, D.Y., Yu, S.-J**. (2013). Al nanorod thin films as anodes electrode for Li ion rechargeable batteries. *Electrochim. Acta*, *87*, 872-879.

[137] **Nithyadharseni, P., Reddy, M.V., Nalini, B., Kalpana, M., Chowdari, B.W.R.** (2015). Sn based intermetallics alloy materials for the applications for lithium ion batteries. *Electrochim. Acta., 161*, 261-268.

[138] **Lv, J., Qui, S., Lu, H., Fu, Y., Li, X., Hu, C., Liu, J.** (2015). Nanostructured Antimony/Carbon composite fibers as anode material for lithium-ion battery, *Electrochim. Acta, 151*, 214-221.

[139] **Kennedy, T., Mullane, E., Geaney, H., Osiak, M., O'Dwyer, C., Ryan, K.M.** (2014). High performance germanium nanowire-based lithium-ion battery anodes extending over 1000 cycles through in-situ formation of a continuous porous network. *Nano Lett., 14,* 716-723.

[140] **Yuan, W., Wu, M., Zhao, H., Song, X., Liu, G.** (2015). Baseline Si electrode fabrication and performance for advanced transportation technologies program. *J. Power Sources, 282,* 223-227.

[141] **Verbrugge, M., Baker, D.R., Xiao, X., Zhang, Q., Cheng, Y.T**. (2015). Experimental and therorical characterization of electrode materals that undergo large volume changes and application to the lithium-silicon system, *J. Phys. Chem. C., 119*, 5341-5349.

[142] **Pollak, E., Salitra, G., Baranchugov, V., Aurbach, D.** (2007). In-situ conductivitiy, impedance spectroscopy, and ex-situ raman of amorphous silicon during the insertion/extraction of lithium, *J. Phys. Chem. C., 111,* 11437-11444.

[143] **Xie, J., Imanishi, N., Zhang, T., Hirano, A., Takeda, Y., Yamamoto, O.** (2010). Li-ion diffu- sion in amorphous Si films prepared by RF magnetron sputtering: a com- parison of using liquid and polymer electrolyte, *Mater. Chem. Phys., 120,* 421-425]

[144] **Li, J., Xiao, X.C., Yang, F.Q., Verbrugge, M.W., Cheng, Y.T.** (2012). Potentiostatic inter- mittent titration technique for electrodes governed by diffusion and interfacial reaction, *J. Phys. Chem. C., 116*, 1472-1478.

[145] **Hwang, C.-M., Park J.-W.** (2010). Investigation of Si-M (Mo, Ti, V) negative electrodes fabricated using RF/DC magnetron sputtering for lithium ion batteries, *Surf. Coat. Tech., 205,* S439-S446.

[146] **Polat, B.D., Eryilmaz, O.L., Keles, O.** (2014). Si based anodes via magnetron sputtering for LIB. *ECS Electrochem Lett., 3,* A45-A49.

[147] **Wang, G.X., Sun, L., Bradhurst, D.H., Zhong, S., Dou, S.X., Liu, H.K.** (2000). Nanocrystalline NiSi alloy as an anode material for lithium ion batteries, *J. Alloys Compds, 306,* 249-252.

[148] **Courtel, F.M., Duguay, D., Abu-Lebdeh, Y., Davidson, I.J.** (2012). Investigation for $CrSi_2$ and $MoSi_2$ as anode material for lithium ion batteries. *J. Power Sources, 202*, 269-275.

[149] **Hatchard, T.D., Obrovac, M.N., Dahn, J.R.** (2006). A Comparison of the reactions of the SiSn, SiAg, and SiZn binary systems with Li, *J.Electrochem. Soc., 153,* A282-A287.

[150] **Lee, K.S., Kim, Y.L., Lee, S.M.** (2005). Silver alloying effect on the electrochmical behavior of Si-Zr thin film anodes, *J. Power Sources, 146*, 464-468.

[151] **Taillades, G., Sarradin, J.** (2004). Silver:high performance anode for thin film lithium ion batteries, *J. Power Sources, 125,* 199-205.

[152] **Erdas, A., Ozcan S., Nalcı, D., Güler M.O., Akbulut H.,** (2015). Novel $Ag/Li_4Ti_5O_{12}$ binary composite anode electrodes for high capacity Li-ion Batteries, *Surf. Coat. Tech., 271,* 136-140.

[153] **Vaughey, J.T., Fransson, K., Swinger, H.A., Edstrom K., Thackeray, M.M.** (2003). Alternative anode materials for lithium ion batteries:A study of $Ag_3Sb$, *J. Power Sources, 119-121,* 64-68.

[154] **Sethuraman, V.A., Kowolik, K., Srinivasan, V**. (2011). Increased cycling efficiency and rate capability of copper-coated silicon anodes in lithium-ion batteries. *J. Power Sources, 196,* 393-398

[155] **Kasavajjula, U., Wang, C., Appleby, A.J.** (2007) Nano- and bulk-silicon-based insertion anodes for lithium-ion secondary cells. *J. Power Sources, 163,* 1003-1039.

[156] **Li, H., Huang, X., Chen, L., Zhou, H., Zhang, Z., Yu, D.,. Mo, Y.J., Pei, N.** (2000). The crystal structural evolution of nano-Si anode caused by lithium insertion and extraction at room temperature. *Solid State Ionics, 135,* 181-191.

[157] **Limothongkul, P., Jang, Y.-I., Dudney, N.J., Chiang, Y.-M.** (2003). Electrochemically-driven solid-state amorphization in lithium-metal anodes. *J. Power Sources, 119-121,* 604-609.

[158] **Limthongkul, P., Jang, Y., Dudney, N.J., Chiang, Y.-M.** (2003) Electrochemically-driven solid-state amorphization of lithium-silicon alloys and implications for lithium storage, *Acta Mater., 51,* 1103-1113

[159] **Shu, Z.X., McMillan, R.S., Murray, J.J.**(1993). Electrochemical intercalation of lithium into graphite. *J. Electrochem. Soc., 140,* 922-927.

[160] **Wang, X., Wen, Z., Lin, B., Lin, K., Wu, Z, Xu, X.** (2008). Preparation and electrochemical chatacterzation of tin/graphite/silver composite as anode materials for lithium ion batteries. *J.Power Sources, 184,* 508-512

[161] **Yin, J., Wada, M., Yamamoto, K., Kitano, Y., Tanase, S., Sakai T.** (2006). Micrometer-scale amorphous Si thin-film electrodes fabricated by electron-beam deposition for Li-ion batteries. *J. Electrochem. Soc., 153,* A472-A477.

[162] **Yue, C., Yu, Y., Wu, Z., He, X., Wang, J., Li, J., Li, C., Wu, S., Li, J., Kang, J.** (2014). Enhanced reversible lithium storage in germanium nano-island coated 3D hexagonal bottle-like Si nanorod arrays. *Nanoscale, 6,* 1817-1822.

[163] **Chen, X., Huang, Y., Huang, H., Wang, M., Wang, K**. (2015). Silver-modified hollow $ZnSO_3$ boxes as high capacity anode materials for li-ion batteries. *Mater. Lett., 149,* 33-36.

[164] **He, B.-L., Dong, B., Li, H.-L.** (2007). Preparation and electrochemical properties of Ag modified-$TiO_2$ nanotube Anode for lithium ion battery. *Electrochem. Commun., 9,* 425-430.

[165] **Tarascon, J.M., Armand, M.** (2001). Issues and challenges facing rechargeable lithium batteries. *Nature, 414*, 359-367.

[166] **Armand, M., Tarascon, J.M.** (2008). Building better batteries. *Nature, 451*, 652-657.

[167] **Wu, H., Cui, Y.** (2012). Designing nanostructured Si anodes for high energy lithium ion batteries. *Nanotoday*, ***7***, 414-429.

[168] **Yoshio, M., Tsumura, T., Dimov, N**. (2005). Electrochemical behaviors of silicon based anode material. *J. Power Sources, 146*, 10-14.

[169] **Yang, B., Irsa, J., He, Y.P., Lundgren, C.A., Zhao, Y.P.** (2012). Chemoelastoplastic analysis of a copper-graded silicon nanorod for lithium-ion battery anode application. *J. Eng. Mater. Tech.,* ***134***, 031013-1

[170] **Chen, X.L., Gerasopoulos, K., Guo, J.C., Brown, A., Wang, C.S., Ghodssi, R., Culver, J.N.** (2010). Virus-enabled silicon anode for lithium-ion batteries. *ACS Nano, 4*, 5366-5372.

[171] **Pal, S., Damle, S.S., Kumta, P.N., Maiti, S.** (2013) Modeling of lithium segregation induced delamination of a-Si thin film anode in Li-ion batteries. *Comput. Mater. Sci., 79*, 877-887.

[172] **Maranchi, J., Hepp, A., Evans, A., Nuhfer, N., Kumta, P.** (2006). Interfacial properties of the a-Si ; Cu: active–inactive thin-film anode system for lithium-ion batteries. *J. Electrochem. Soc., 153*, A1246-A1253.

[173] **Zhang, W.-J.** (2011). A review of the electrochemical performance of alloy anodes for lithium-ion batteries. *J. Power Sources, 196*, 13-24.

[174] **Liu, W.-R., Wu, N.L., Shieh, D.-T., Wu, H.-C., Yang, M.-H., Korepp, C., Besenhard, J.O., Winter, M.** (2007). Synthesis and characterization of nanoporous NiSi-Si composite Anode for lithium-ion batteries. *J. Electrochem. Soc. 154*, A97-A102.

[175] **Murugesan, S., Harris, J.T., Korgel, B.A., Stevenson, K.J.** (2012). Copper-coated amorphous Silicon particles as an anode material for lithium-ion batteries. *Chem. Mater., 24*, 1306-1315.

[176] **Pu, W., He, X., Ren, J., Wan, C., Jiang, C.** (2005). Electrodeposition of Sn–Cu alloy anodes for lithium batteries. *Electrochim. Acta, 50*, 4140-4145.

[177] G**ao, J., Zhang, H.P., Zhang, T., Wu, Y.P., Holze, R.** (2007). Preparation of Cu coating on graphite electrode foil and its suppressive effect on PC decomposition. *Solid State Ionics, 178*, 1225-1229

[178] **He, Y., Fan, J., Zhao, Y.** (2010). Engineering a well-aligned composition-graded CuSi nanorod array by an oblique angle codeposition technique. *Cryst. Growth Des., 10*, 4954-4958.

[179] **Wilson, A.M., Dahn, J.R.** (1995). Lithium insertion in carbons containing nanodispersed silicon. *J. Electrochem. Soc., 142*, 326-332.

[180] **Bourderau, S., Brousse, T., Schleich, D.M.** (1999). Amorphous silicon as a possible anode material for Li-ion batteries. J. Power Sources, *(81–82)* 232-238

[181] **Ohara, S., Suzuki, J., Sekine, K., Takamura, T.** (2003). Li insertion/extraction reaction at a Si film evaporated on a Ni foil. J. Power Sources, *119–121*, 591-596.

[182] **He, Y., Brown, C., Lundgren, C.A., Zhao, Y**. (2012). The growth of CuSi composite nanorod arrays by oblique angle co-deposition, and their structural, electrical and optical properties. *Nanotechnology*, *23*, 1–10.

[183] **Semaltianos, N.G.** (2001). Thermally evaporated aluminium thin films. *Appl. Surf. Sci.*, *183*, 223-229.

[184] **Young, S., Shieh, D.-T., Wu, H.-C., Yang, M.-H., Wu, N.-L.** (2005). Effect of electrode structure on performance of Si anode in Li-ion batteries: Si particle size and conductive additive. *J. Power Sources, 140,* 139-144.

[185] **Polat, B.D., Keles, O.** (2015). Improving si anode performance by forming copper capped copper-silicon thin film anodes for rechargeable lithium ion batteries. *Electrochim. Acta, 170,* 63-71.

[186] **Zhuo, K., Jeong, M.-G., Chung, C.-H.** (2015). Highly porous dendritic Ni-Sn anodes for lithium-ion batteries. J. Power Sources, *244*, 601-605.

[187] **Piper, D.M., Evans, T., Leung, K., Watkins, T., Olson, J., Kim, S.C., Han, S.S., Bhat, V., Oh, K.H., Buttry, D.A., Lee, S.-H.** (2015). Stable silicon-ionic liquid interface for next- generation lithium-ion batteries. *Nature Commun.*, ***6***, 1-6.

[188] **Tan, L.P., Lu, Z., Tan, H.T., Zhu, J., Rui, X., Yan, Q., Hng, H.H.** (2015). Germanium nanowires-based carbon composite as anodes for lithium-ion batteries. *J. Power Sources*, *206*, 253-258.

[189] **Song, Z., Ma, T., Tang, R., Cheng, Q., Wang, X., Krishnaraju, D., Panat, R. Chan, C.K., Yu, H., Jiang, H.** (2014). Origami lithium-ion batteries. *Nature Commun.*, *5*, 1-7.

[190] **Usui, H., Meabara, K., Nakai, K., Sakaguchi, H**. (2011). Anode properties of composite thick-film electrodes consisted of Si and various metal silicides, *Int. J. Electrochem. Soc***., *6*,** 2246-2254

[191] **Suzuki, J., Yoshida, M., Nishijima, Y., Sekine, K., Takamura, T.** (2002). Effect of a vacuum-deposited metal film on the CV of the Li insertion/extraction reaction at a graphitized carbon fiber electrode, *Electrochim. Acta, 47,* 3881-3890.

[192] **Jung, H., Park, M., Han, S.H., Lim, H., Joo, S.-K.** (2003). Amorphous silicon thin-film negative electrode prepared by low pressure chemical vapor deposition for lithium-ion batteries. *Solid State Commun., 125,* 387-390.

[193] **Luo, L., Yang, H., Yan, P., Travis, J.J., Lee, Y., Liu, N., Piper, D.M., Lee, S.-H., Zhao, P., George, S.M., Zhang, J.-G., Cui, Y., Zhang, S., Ban, J., Wang, C.-M.** (2015). Surface-coating regulated lithiation kinetics and degradation in silicon nanowires for lithium ion battery. *ACS Nano, 9,* 5559-5566.

[194] **Gohier, A., Laik, B., Pereira-Ramos, J.-P., Cojocaru, C.S., Tran-Van, P.** (2015). Influence of the diameter distribution on the rate capability of silicon nanowires for lithium-ion batteries. *J. Power Sources, 203,* 135-139

[195] **Xu, W., Vegunta, S.S.S., Flake, J.C. (**2011). Surface-modified silicon nanowire anodes for lithium-ion batteries, *J. Power Sources, 196*, 8583-8589

[196] **Park, M.-H., Kim, M.G., Joo, J., Kim, K., Kim, J., Ahn, S., Cui, Y., Cho, J.** (2009). Silicon nanotube battery anodes, *Nano Lett., 9,* 3844-3847.

[197] **Feng, C., Zhang, L., Wang, Z., Song, X., Sun, K., Wu, F., Liu, G.** (2014). Synthesis of copper sulfide nanowire bundles in a mixed solvent as a cathode material for Lithium-Ion batteries, *J. Power Sources, 269,* 550-555.

[198] **Jing, S., Jiang, H., Hu, Y., Li, C**. (2014). Directly grown Si nanowire arrays on Cu Foam with a coral-like surface for lithium-ion batteries. *Nanoscale, 6***,** 1441-1445

[199] **Ng, H.T., Foo, M.L., Fang, A., Xu, G., Jaenicke, S., Chan, L., Li, S.F.Y.** (2002). Soft-lithography mediated chemical vapor deposition of architectured carbon nano-tube networks on elastomeric polymer. *Langmuir, 18***,** 1-5.

[200] **Dick, B., Brett, J.M.** (2003). Investigation of substrate rotation at glancing incidence on thin-film morphology. *J. Vac. Sci. Technol. B, 21,* 2569-2574.

[201] **Steele, J.J., Brett, M.J.** (2007). Nanostructure engineering in porous columnar thin films: recent advances. *J. Mater. Sci Mater. Electron., 18,* 367-379.

[202] **Seto, M.W., Robbie, K., Vick, D., Brett, M.J., Kuhn, L.** (1999). Mechanical response of thin films with helical microstrucures, *J. Vac. Sci. Tech., 17,* 2172-2177.

[203] **Guo, K., Pan, Q., Wang, L., Fang, S.** (2002). Nano-scale copper-coated graphite as anode material for lithium ion batteries. J. App. Electrochem., *32,* 679-685

[204] **Elazari, G. Salitra, G. Gershinsky, A. Garsuch, A., Panchenko, D. Aurbach**. (2012) Li Ion cells comprising lithiated columnar silicon film anodes, $TiS_2$ cathodes and fluoroethyene carbonate (FEC) as a critically important component. *J. Electrochem. Soc,. 159,* A1440-A1445.

[205] **Polat, B.D., Eryilmaz, O.L., Keles, O.** (2016). SiAg film by magnetron sputtering for *high reversible lithium ion storage anodes. Journal of Alloys and Compounds, 654,* 363-370.

[206] **Polat, B.D., Keles, O.** (2016). Functionally Graded Si Based Thin Films as Negative Electrodes for Next Generation Lithium Ion Batteries. *Electrochimica Acta, 187,* 293–299.

[207] **Polat, B.D., Keles, O., Amine, K. (**2016) Compositionally-Graded Silicon-Copper Helical Arrays as Anodes for Lithium-Ion Batteries. *Journal of Power Sources, 304,* 273-281.

**CURRICULUM VITAE**

Name Surname: Billur Deniz Karahan

Place and Date of Birth: Adapazari, 25.07.1985

E-Mail: bpolat@itu.edu.tr

B.Sc.: Istanbul Technical University

M.Sc.: Istanbul Technical University

**Professional Experience:**

September 2006-January 2009 Project Development Engineer<br>Galtek Galvano Ltd Şti., Turkey

January 2009- Current Research Assistant at ITU, Turkey.

October 2012- May 2013 Visitor Scholar at Argonne National Lab., USA

To improve the mechanical and the physical properties of Si based electrodes, structured Si based films have been produced by both magnetron sputtering and electron beam deposition methods.

**Rewards:**

| | |
|---|---|
| 2017 | ICMCTF Graduate Student Award |
| 2016 | Electrochemical Society Battrey Division Student Research Award |
| 2010-2014 | The Scientific and Technological Research Council of Turkey (TUBITAK) Merit Award |
| 2010 | ITU Material Science and Engineering Program, Valedictorian |
| 2008 | ITU Metallurgical and Material Science Engineering Dep., Valedictorian |
| 2008 | ITU Chemical-Metallurgy Faculty Valedictorian. |

| | |
|---|---|
| 2004 | Yıldız Technical University, Metallurgical and Material Science Engineering Department, Valedictorian |
| 2001 | Sainte Pulchérie French High School, Valedictorian |
| 2001 | IV. Activities Sportives et Culturelle Franco-Turque Contest, The Best Orator Award |
| 2001 | IV. Activities Sportives et Culturelle Franco-Turque Contest, The Best Speaker Group Award |

**List of Publications and Patents:**

**Books:**

**1.** Keleş, Ö., Amine, K., **Polat, B. D.** (2014). Nanocolumnar Porous Cu-Sn Thin Film as Anode Material for LIB. Saarbrücken, LAP.

**2. Polat, B. D.,** Eryilmaz, O. L., Keleş, Ö. (2015). Silicon Based Thin Film Anodes for Next Generation Lithium Ion Battery. Saarbrücken, LAP.

**Papers Published in Journals:**

**Polat, B.D.,** Keleş, Ö. (2017). Designing Self Standing Three Dimensional Composite SiCu Thin Films as Anodes for Lithium Ion Battery, *Journal of Nanoscience and Nanotechnology, 17,* (1), 606-615.

**Polat, B.D.,** Keleş, Ö. Amine, K. (2016). Compositionally-Graded Silicon-Copper Helical Arrays as Anodes for Lithium-Ion Batteries", *Journal of Power Sources, 304,* 273-281.

**Polat, B.D,.** Keleş, Ö. (2016). Functionally Graded Si Based Thin Films as Negative Electrodes for Next Generation Lithium Ion Batteries", *Electrochimica Acta, 187,* 293–299

**Polat, B.D.,** Keleş, **Ö. (2016).** Designing Self-Standing Silicon-Copper Composite Helices as Anodes for Lithium Ion Batteries, *Journal of Alloys and Compounds, 677,* 228 – 236.

**Polat, B.D.,** Keleş, Ö., Chen, Z.H., Amine, K. (2016). Si–Cu Alloy Nanowires Grown by Oblique Angle Deposition as a Stable Negative Electrode For Li-Ion Batteries, *Journal of Material Science, 51*, 6207-6219.

**Polat, B. D.,** Eryilmaz, O. L., Keleş, Ö. (2016). Fabrication of SiAg film by magnetron sputtering as high capacity lithium ion storage anodes for lithium ion batteries. *J. Alloys Compnd., 654*, 363-370.

**Polat, B. D.,** Eryilmaz, O.L., Keleş, Ö., Erdemir, A., Amine, K. (2015). Compositionally graded SiCu thin film anode by magnetron sputtering for lithium ion battery. *Thin Solid Films, 596, 190–197.*

**Polat, B. D.,** Keleş, Ö., Amine, K. (2015). Silicon-copper helical arrays for new generation lithium ion batteries. *Nano Letter, 15,* 6702-6708.

**Polat, B. D.,** Keleş, Ö. (2015). The effect of Cu coating on nanocolumnar Si anode. *Thin Solid Films, 589,* 543-550.

**Polat, B. D.,** Keleş, Ö. (2015). Improving Si anode performance by forming copper capped Copper-Silicon thin film anode for rechargeable lithium ion batteries. *Electrochimica Acta*, *170***,** 63-71.

**Polat, B. D.,** Eryılmaz, O. L., Chen, Z., Keleş, Ö. ve Amine, K. (2015). High capacity anode with well- aligned, ordered NiSi nano-columnar arrays. *Nano Energy, 13*, 781-789.

**Polat, B.D.,** Keleş, Ö. (2015). Multi-layered Cu/Si nanorods and its use for lithium ion batteries. *Journal of Alloys and Compounds, 622*, 418-425.

**Polat, B. D.,** Keleş, Ö. (2015). The effects of film thickness and evaporation rate on Si-Cu thin films for lithium ion batteries. J. *Nanoscience and Nano Technology, 15,* 1-9.
**Polat, B. D.,** Keleş, Ö., Ürgen, M. (2015). Optimization of the anodic layer morphology on aluminum in a mixed phosphoric/sulfuric acids bath using taguchi method. *Advanced Science, Engineering and Medicine, 7,* 1-6.
**Polat**, **B. D.,** Eryılmaz, O.L, Erck, R., Keleş, Ö., Erdemir, A., Amine, K. (2014). Structured SiCu thin films in LIB as anodes. *Thin Solid Films*, *572*, 134-141.
**Polat, B. D.,** Keleş, Ö., Amine, K. (2014). Well-aligned, ordered, nanocolumnar, Cu-Si thin film as anode material for lithium – ion batteries. *Journal of Power Sources*, *270*, 238- 247.
**Polat, B. D.,** Abouimrane, A., Sezgin, N., Keleş, Ö., Amine, K. (2014). Use of multilayered Ni-Sn and Ni-Sn-C thin film anodes for lithium-ion batteries. *Electrochimica Acta*, *135*, 585-593.
**Polat, B.D.,** Keleş, Ö. (2014). Improving the Electrochemical Performance of Tin Based Anodes Formed via Oblique Angle Deposition Method, *Bulletin of Material Science, 37* (7), 1701-1708.
**Polat, B. D.,** Keleş, Ö. (2014). The use of well-aligned composite nanorod arrays as anode material for lithium rechargeable batteries. *Journal of Power Sources*, *266***,** 353-364.
**Polat, B. D.,** Lu, J., Keleş, Ö., Amine, K. (2014). Nanocolumnar structured porous Cu-Sn thin film as anode material for lithium-ion batteries. *ACS Applied Materials and Interfaces, 6,* 10877-10885.
**Polat, B. D.,** Eryılmaz, O. L. ve Keleş, Ö. (2014). Si based anodes via magnetron sputtering for LIB. *ECS Electrochemistry Letters*, *3,* A45-A49.
**Polat, B. D.,** Sezgin, N., Keleş, Ö., Kazmanlı, K., Abouimrane, A. ve Amine, K. (2013). A nano- architectured porous electrode assembly of copper rich $Cu_6Sn_5$ thin film for rechargeable lithium batteries. *Journal of Alloys and Compounds*, *553***,** 204–207.
Zümrüt, Z., **Polat, B. D.,** Akın, İ., Keleş, Ö. ve Göller, G. (2013). Bioactivity characterization and a full factorial design on the adhesive strength of air plasma sprayed Ha-$TiO_2$ coated Ti. *Journal of The Australian Ceramic Society, 49,* 95 – 103.
Ürgen, M., Keleş, Ö., **Polat, B. D**., Bayata, F. (2012). Generation of a surface pattern having conical surface features by anodic polarization of aluminum. *Journal of Electrochemical Society, 159,* C411-C415.

Papers Published in National Journals:

**Polat, B.D.** Sıcak daldırma galvaniz prosesinde ZnNi alaşımlarının kullanımı. *Galder* (Kabul edildi).
**Polat, B. D. ve Keleş, Ö.** (2015). Fosil yakıtların en güçlü alternatifi: lityum iyon Piller-1. *Enerji Panorama*, *22*, 69-71.
**Polat, B. D. ve Keleş, Ö.** (2015). Fosil yakıtların en güçlü alternatifi: lityum iyon piller-2. *Enerji Panorama*, *23*, 62-65.
**Polat, B.D.** (2013). Zamak alaşımı nedir? Zamak'tan nasıl para kazanılır. *Metalurji Dergisi*, *159*, 34-45.
**Polat, B.D.** (2013). Zamak dökümde sıkça karşılaşılan hatalar. *Metalurji Dergisi,* ***159,*** 46-54.

**Polat, B. D.,** Timur, İ. S. ve Keleş, Ö. (2013). Çinko-Alüminyum alaşımından üretilmiş döküm parçalarının korozyon direncine bakır kaplama proseslerinin etkisi. *Gazi Universitesi Fen Bilimleri Dergisi : Tasarım ve Teknoloji, 3*, 103-113.
**Polat, B. D.,** Keleş, Ö. (2012). Dünya'da ve Türkiye'de lityum iyon pil teknolojisi. *Gas and Power Dergisi*, 6-7.
**Polat, B. D.,** Keleş, Ö. (2012). Lityum iyon pil teknolojosi. *Metalurji Dergisi, 162*, 42-48.
**Polat, B. D.,** Keleş, Ö., Timur, İ. S. (2012). Zamak Alaşımları İçin Farklı Bakır Kaplama Prosesleri. *Yüzey İşlemleri Dergisi* , 40-44.
**Polat, B. D.,** Keleş, Ö. (2012). Zamak alaşımları üzerine uygulanan kaplama öncesi yüzey hazırlama işlemlerin önemi. *Yüzey İşlemleri Dergisi*, 68-72.
İhvan, S., **Polat, B. D.,** Sezer, D., Keleş, Ö. (2012). Alüminyum köpük üretiminde alaşım elementlerinin etkisi. *İTÜ Dergisi*, **2**, 149-157.
**Polat, B. D.,** Keleş, Ö., Taptık, Y**.** (2010). Metalik köpükler, alüminyum metalik köpük ve üretim yöntemleri. *Metal Dünyası*, *205*, 2-7.

**PUBLICATIONS/PRESENTATIONS ON THE THESIS**

**Publications on the thesis**

**Polat, B. D.,** Keleş, Ö., Amine, K. (2016). Compositionally-graded silicon-copper helical arrays as anodes for lithium-ion batteries. *Journal of Power Sources, 306***,** 273-281
**Polat, B.D.,** Keles, O., Chen, Z.H., Amine, K. (2016). Si-Cu alloy nanowires grown by oblique angle deposition as a stable negative electrode for Li ion batteries. *Journal of Materials Science*, DOI: 10.1007/s10853-016-9918-3
**Polat, B.D.,** Eryilmaz, O.L., Keles, O. (2016). Fabrication of SiAg film by Magnetron Sputtering as High Capacity Lithium Ion Storage Anodes for Lithium Ion Batteries, *J. Alloys Compnd., 654*, 363-370.
**Polat, B.D.,** Keles, O. (2015). Functionally Graded Si Based Thin Films as Negative Electrodes for Next Generation Lithium Ion Batteries. *Electrochim. Acta, 187,* 293-299.
**Polat, B.D.,** Keles, O. (2015). Improving Si Anode Performance by Forming Copper Capped Cu-Si Thin Film Anode for LIB, *Electrochim. Acta, 170,* 63-71.
**Polat, B.D.,** Eryilmaz, O.L., Keles, O. (2014). Si Based Anodes via Magnetron Sputtering for LIB, *ECS Electrochemistry Lett., 3* (6) A45-A49.

<u>Presentations on the thesis</u>

**Polat, B.D.,** Bilici, B., Keles, O. (2016). "Si and SiCu Three Dimensional Sculptured Films as Negative Electrodes for Rechargeable Lithium Ion Batteries" (poster). 145. *The Minerals Materials Society,* Tenneessee-USA.
**Polat, B.D.,** Keles, O. (2016). "Optimizing Composition and Morphology of the Structured Si Based Films as Anodes in LIB" (poster). *Advancaed Automotive Battery Conference*, Huzhou- China.
**Polat, B.D.,** Keles, O. (2016). "Production and Characterization of Si based Thin Films as Negative Electrodes for Secondary Lithium Ion Batteries'' (oral presentation). *Prime Pasific Rim Meeting on Electrochemical and Solid State Science*, Honolulu- Hawaii.
**Polat, B.D.,** Keles, O. (2016). "Chevron like Structured SiCu Thin Film Anodes for Lithium Ion Batteries" (poster). *18. International Meeting on Lithium Ion Batteries,* Chicago-USA.

**Polat, B.D.,** Eryilmaz, O.L., Keles, O. (2015) “Generation of AgSi Film by Magnetron Sputtering for Use as Anodes in Lithium Ion Batteries” *(*poster*). 227 The Electrochemical Society Meeting*, Chicago- USA.

**Polat, B.D.,** Keles, O. (2015). “Evaluation of Si Based Composite Helices Used as Anodes for Rechargeable in LIB” (oral presentation). *227. The Electrochemical Society Meeting*, Chicago- USA.

**Polat, B.D.,** Keles, O. (2015). “Three Dimensional Structured Silicon-Copper Composite Films as High Performance Anodes for Next Generation LIBs” (poster). 8. *International Conference on Advanced Lithium Batteries for Automobile Applications*, Bilbao-Spain.

**Polat, B.D.,** Eryilmaz, O.K., Keles, O. Erdemir, A., Amine, K. (2015). “Compositionally Graded SiCu Thin Film Anode by Magnetron Sputtering for Lithium Ion Batteries” (oral presentation). *42. International Conference on Metallurgical Coatings and Thin Films*, San Diego- USA.

**Polat, B.D.,** Eryilmaz, O.L., Keles, O. (2014), “Improving Electrochemical Performance of CuSi Thin Film by Depositing Cu Thin Film via Magnetron Sputtering” (poster). *226 The Electrochemical Society Meeting*, Cancun-Mexico.

**Polat, B.D.,** Eryilmaz, O.L., Keles, O. (2014), “Optimization in the Electrochemical Performance of Cu/Si Thin Film Anode Produced via Magnetron Sputtering” (oral presentation). *224. The Electrochemical Society Meeting*, San Francisco-USA.